University of California
Santa Barbara

Fluid-driven Fractures in Heterogeneous Environments

A dissertation submitted in partial satisfaction
of the requirements for the degree

Doctor of Philosophy
in
Mechanical Engineering

by

Sri Savya Tanikella

Committee in charge:

Professor Emilie Dressaire, Chair
Professor Tresa Pollock
Professor Eckart Meiburg
Professor Todd Squires

March 2024

The Dissertation of Sri Savya Tanikella is approved.

Professor Tresa Pollock

Professor Eckart Meiburg

Professor Todd Squires

Professor Emilie Dressaire, Committee Chair

March 2024

Fluid-driven Fractures in Heterogeneous Environments

by

Sri Savya Tanikella

To my parents and sister...

Acknowledgements

First and foremost, I express my sincere gratitude to my advisor and mentor, Dr Emilie Dressaire. When I first came in, you told me that a PhD is more of a marathon than a sprint, and you were right. There were some parts where I sped through, and some parts where I couldn't get myself to walk. You were always there, helping me through it all. I cannot thank you enough for everything you have done and everything I learned from you, whether scientifically or personally.

A special thank you to my dissertation committee, Professors Tresa Pollock, Eckart Meiburg and Todd Squires for taking out the time to discuss and provide me with valuable comments on my research.

For his helpful insights, I would like to thank Emre Turkoz. Thank you for coming to my conference talks and discussing my research with me. Your input has been instrumental in guiding me towards fruitful directions for further exploration.

I would also like to express my gratitude to everyone I worked with in the BIFF lab. I couldn't have asked for better people to share my PhD journey with. Sara, you helped me get through some of the lowest points in my PhD, and in you, I have found a lifelong friend. I have some of my most cherished memories in Santa Barbara with you. Thank you for being my lab mate, my running partner, my fun-friend, and my closest confidante. JP, thank you for all the work you did with me and for always being your cheery self. I don't think I would have been able to make the 7 ft long channels without your patience. Sean and Trinh, thank you for all the spirited discussions we had in the office; it was always a welcome distraction from work. Brian and Amanda, thank you so much for helping me find my footing in Santa Barbara.

My internship at Intel was an amazing experience, providing me with the opportunity to apply and expand my knowledge beyond my PhD. Pramod, I am truly grateful for

everything you have done for me. Canh and Yuqin, thank you for being the best mentors one could ask for. Your patience and support made me feel valued and welcomed throughout my time there.

Mengye and Mariam, thank you for helping me through my first couple of years in my PhD. Solaire, thanks for showing me the ropes; I would have been culturally very lost without you.

Shivnag, Mohit, Anusha, and Pranjali, thank you for being there and listening to my rambles, even though I probably did not make coherent sense a lot of the time. Shivnag, I can maybe imagine my life without bananas, but not without you. Mohit, thank you for always taking the time to meet me whenever I am in India. I will visit your home soon. I promise. Anusha, you have helped me more than you realize. You have always pushed me to be better, and I will be forever grateful for that. Pranjali, thank you for all the tasty food. I have yet to meet someone who can make aloo better than you.

Chetan, I don't know where to begin. This is probably where I accept defeat and just thank you for being my emotional support mountain, and also for the invaluable scientific discussions that helped me in many tricky situations. Thank you for putting up with me and my fancies. You make me hopeful.

Finally, I would like to thank my parents, Lalitha and Radha Krishna, and my sister, Guddu. None of this would have been possible without them. Everything that is good about me, is an imitation of them.

Curriculum Vitæ

Sri Savya Tanikella

Education

2024	Ph.D. in Mechanical Engineering (Expected), University of California, Santa Barbara.
2019	B.Tech. in Chemical Engineering, Minor in Mechanical Eng., Indian Institute of Technology, Gandhinagar

Publications

S. S. Tanikella, S. Bohling, J.P. Raimondi, N.D. Jones, and E. Dressaire, Creeping flows through confined channels, *In preparation*, 2024.

S. S. Tanikella, M. C. Sigallon, and E. Dressaire, Dynamics of fluid-driven fractures in layered materials, *To be submitted*, 2024.

S. S. Tanikella, M. C. Sigallon, and E. Dressaire, Dynamics of fluid-driven fractures in the viscous-dominated regime, *Proc. R. Soc. A*, 2023.

S. S. Tanikella and E. Dressaire, Axisymmetric displacement flows in fluid-driven fractures, *J. Fluid Mech.*, 2022.

Conference Proceedings

S.S. Tanikella, N. D. Jones, and E. Dressaire, A Numerical Study of the Effect of Surface Coverage on the Filtration Performance of Hair Arrays, *Proceedings of the ASME 2021 International Mechanical Engineering Congress and Exposition*, 2021.

Conference Abstracts

S. S. Tanikella, E. Dressaire, and M. C. Sigallon, How multilayered rocks seal the fate of fluid-filled fractures, *76th Annual Meeting of the Division of Fluid Dynamics*, November 19–21, 2023; Washington, DC.

S. S. Tanikella, and E. Dressaire, Dynamics of fluid-driven fractures in the viscous-dominated regime, *75th Annual Meeting of the Division of Fluid Dynamics*, November 20–22, 2022; Indianapolis, Indiana.

S. S. Tanikella, and E. Dressaire, Growth of fluid-driven fractures in the viscous-dominated regime, *APS March Meeting 2022*, March 14–18, 2022; Chicago.

S. S. Tanikella, and E. Dressaire, Displacement flow in an Elastic Fracture, *APS March Meeting 2021*, March 15–19, 2021; Virtual.

Abstract

Fluid-driven Fractures in Heterogeneous Environments

by

Sri Savya Tanikella

Fluid-driven subsurface fractures interact with a variety of heterogeneous elements in the surrounding environment, including fluid-filled pores, material discontinuities, and other cracks and fissures. Their complex propagation is governed by fluid-solid interactions, characterized by nonlinear and coupled dynamics between the flow and the fracture. This thesis focuses on addressing a variety of such problems related to fluid-driven fractures or hydraulic fractures within increasingly realistic situations. Initially, we examine the post-shut-in behavior of a hydraulic fracture in the viscous regime, where viscous dissipation is the dominant form of energy dissipation. Subsequently, we investigate the propagation of a hydraulic fracture driven by displacement flows of two immiscible fluids and the propagation of a hydraulic fracture across a material discontinuity.

When pressurized fluid is injected in a homogeneous infinite solid medium, a simple penny-shaped fracture forms and grows in the direction of the minimum confining stress. This type of fracture offers a representative focus for experimental investigations in a laboratory environment, serving as a powerful tool to understand the various physical mechanisms governing the growth of the fracture. Throughout the thesis, we vary different material properties of the solid media and fracturing fluids, including the Young's modulus of the solids, the viscosity of the fluids and, the flow rate of the injection. Gelatin serves as the clear brittle elastic solid medium, that allows us to observe and record the fracture growth because of its transparent nature.

In the first study, we examine the post-shut-in behavior of a penny-shaped hydraulic

fracture in the viscous regime. We measure both the fracture aperture and radius, noting that the fracture radius continues to grow slowly over time even after injection stops, until it reaches a saturation point.

Next, we investigate the injection of an immiscible fluid at the center of a liquid-filled fracture. We study the displacement of the interface between the two fluids and its effect on fracture propagation. We conduct experiments and derive scales to predict the growth dynamics of the fracture.

Finally, we present an experimental investigation into the propagation of hydraulic fractures in layered brittle media in the toughness regime, where the creation of new fracture surfaces is the dominant means of energy dissipation. We report that the relative stiffness of the initiating layer significantly influences fracture propagation: A fracture that forms in a soft layer remains trapped, whereas a fracture that originates in a stiffer layer experiences a rapid fluid transfer into the neighboring softer layer upon reaching the interface. Additionally, we present a quantitative model that captures the competing effects of elastic deformation and fracture propagation and report good agreement with experiments.

Contents

Chapter 1

Introduction

Hydraulic fracturing results from the injection of a pressurized fluid in low-permeability solid media. Hydraulic fracturing was developed as a technique to extract oil and gas trapped in shale rocks (unconventional reservoirs), which otherwise have low permeability, making it difficult to extract using conventional methods. For oil and gas extraction, the process involves injecting a fluid comprised mostly of water, sand, and chemicals ($< 2\%$) into the shale rock [1] as shown in figure 1.1. The chemicals help suspend the sand in the water and also reduce the effective viscosity of the suspension, helping make the process more economically viable. The injected fluid creates tensile fractures in the rock, that are initiated and propagated due to the pressure in the fluid. The sand particles are used as "proppants", which ensure that the fractures stay propped open once the injection stops. These fractures help create a pathway for the trapped oil/gas to reach the well-bore.

Apart form oil and gas extraction, hydraulic fracturing is also used to improve permeability in geothermal energy reservoirs. Another recent application has been in carbon sequestration. Because of the considerable risks and expenses associated with CO_2 transportation, storage in a reservoir near the emission source is preferred [2, 3]. Yet, local reservoirs may not possess the most favorable characteristics for storing large fluid vol-

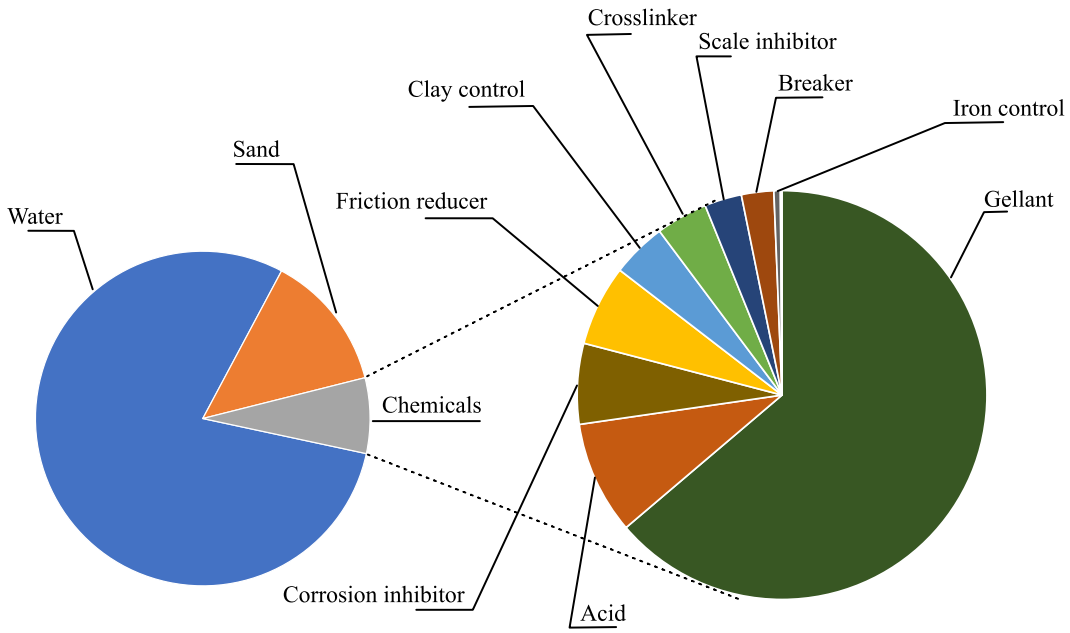

Figure 1.1: Composition of typical hydraulic fracturing fluid for oil and gas applications as reported by FracFocus [1].

umes, requiring hydraulic fracturing to improve permeability [4].

However, the injection of large amounts of fluid into geological formations poses environmental and public health risks associated with water footprint, seismic activity, and leakage of the fracture content [5, 6, 7]. Carbon sequestration commonly relies on cap rocks to prevent leaks [8]. Yet injection can induce fracture propagation within the reservoir and cap rock [9, 10, 11, 12], compromising long-term storage. Leakage can also contaminate groundwater reservoirs, directly impacting local ecosystems and populations [13]. Therefore, the mapping of underground mechanics and development of predictive models are essential for safe fluid injection and storage.

The complex mechanics of fluid-driven fractures are governed by the elastic deformation of the solid medium, fluid flow within the fracture, and the criteria for fracture propagation at the tip of the tensile fracture [14]. When pressurized fluid is injected from a point source into an infinite, homogeneous solid medium, a penny-shaped hydraulic frac-

ture forms and grows in the direction of the minimum confining stress. Seminal work on the stress distribution in a penny-shaped fracture [15] and the injection of viscous fluids to form fractures [16, 17] led to the development of self-similar solutions for fractures whose propagation is limited by the viscous dissipation in the fluid [18]. Further work on the crack front or tip region identified two asymptotic regimes for the tip geometry and fracture propagation [19, 20, 21, 22, 23]; In the viscous-dominated regime, the viscous dissipation in the flow opposes the elastic stress of the deformable boundary to control the fracture evolution. Whereas, in the toughness-dominated regime, the material toughness opposes the propagation of the fracture and determines the growth dynamics. Moreover, if the surrounding solid medium is porous, some of the injected fluid will escape from the fracture into the surroundings, thus modifying the growth dynamics of the hydraulic fracture. Therefore, the growth of a hydraulic fracture depends on the relative importance of two dissipative mechanisms and two storage mechanisms [24].

Numerous experimental studies have been conducted to validate tip asymptotes, study near-surface fractures, and understand the initiation and early-stage growth of fluid-driven fracture [25, 26, 27, 28, 29, 30, 31, 32]. Additionally, recent experimental studies have explored increasingly complex systems to gain better insights into the propagation dynamics of hydraulic fractures in rock formations [33, 34, 35, 36]. These studies contribute significantly to our understanding of the physical mechanisms associated with fracture coalescence, fracture propagation induced by the injection of heterogeneous fluids like foam, observations of fracture propagation in the presence of material stratification, and fracture surface roughness. They also offer insights into developing more realistic models for predicting fracture initiation and growth. However, a gap exists in understanding and modelling the propagation dynamics of the fracture in complex heterogeneous systems. Specifically, we aim to investigate scenarios where the injected fluid interacts not directly with the impermeable rock but with another fluid within the rock. Consid-

ering the well-known stratification of rocks inside the Earth, we explore questions about the impact when the injected fluid encounters an interface. Additionally, we delve into the effects when the flow is shut off, examining whether the fracture ceases propagation or continues.

1.1 Methodology overview

Throughout this thesis, we focus on developing theoretical frameworks for complex, heterogeneous systems. This enables direct comparison with existing theories designed for single fracture propagation. Using simple scaling analysis tools, we aim to construct comprehensive theories capturing intricate dynamics. To validate and refine these theories, we conduct experiments in clear hydrogels. This combined theoretical-experimental approach forms the core of our methodology, providing a robust foundation for understanding heterogeneous systems.

When a fluid is injected into a solid to induce fracture, numerous mechanisms come into play. We make assumptions regarding fluid flow and fracture propagation to simplify the system. Given the low injection rates, the fracture propagates at equilibrium, and the liquid and fracture fronts coincide at all times, with no fluid lag. Additionally, the surrounding solid medium is considered impermeable, eliminating fluid leak-off from the fracture.

The growth of the fluid-filled fracture is given by the coupled equations that describe (a) the viscous flow in the fluid phases (b) the elastic deformation of the solid material or fracture walls, (c) the stress intensity factor at the tip of the fracture, and (d) the volume conservation. These sets of equations are coupled by the net pressure in the fracture. As mentioned earlier, two different sets of scales can be derived depending on whether the primary mechanism of energy dissipation is viscous dissipation in the fluid (the viscous

regime) or the creation of new fracture surfaces (the toughness regime). The derived scales are then verified by conducting experiments in gelatin. Gelatin has been used to experimentally study many different fluid driven fracture systems including buoyancy driven magma transport [37, 38, 39] and hydraulic fractures [28, 29, 40, 34, 41, 42]. Gelatin is a clear gel whose properties can be easily tuned by varying the wt% of gelatin powder added to water [43]. Gelatin's transparency allows easy visualization of the fracture, facilitating different methods to record fracture geometry evolution, such as radius and thickness.

We compare the experimentally derived fracture data with the theoretical model by scaling relevant physical quantities, such as fracture radius, thickness, and pressure, using the appropriate scales.

1.2 Outline

This thesis is structured as follows: The core of the work revolves around understanding fluid-driven fractures in increasingly heterogeneous environments. In this thesis, we investigate three main problems, (i)fracture propagation in viscous regime after the injection stops,i.e., post "shut-in", (ii) fracture propagation driven by two immiscible fluids and, (iii) fracture propagation across a material interface. Each of the studies is written as a separate chapter. Below, a concise summary of each chapter, touching on the motivation and some of the key findings, is provided.

Chapter 2: Dynamics of fluid-driven fractures in viscous dominated regime During hydraulic fracturing, the injection of a pressurized fluid in a brittle elastic medium leads to the formation and growth of fluid-filled fractures. A disc-like or penny-shaped fracture grows radially from a point source during the injection of a viscous fluid at a constant flow rate. We report an experimental study on the dynamics of fractures propa-

gating in the viscous regime. We measure the fracture aperture and radius over time for varying mechanical properties of the medium and fluid and different injection parameters. Our experiments show that the fracture continues to expand in an impermeable brittle matrix, even after the injection stops. In the viscous regime, the fracture radius scales as $t^{4/9}$ during the injection. Post shut-in, the crack continues to propagate at a slower rate, which agrees well with the predictions of the scaling arguments, as the radius scales as $t^{1/9}$. The fracture finally reaches an equilibrium set by the toughness of the material. The results provide insights into the propagation of hydraulic fractures in rocks.

Chapter 3: Axisymmetric displacement flows in fluid-driven fractures

Displacement flows are common in hydraulic fracturing, as fracking fluids of different composition are injected sequentially in the fracture. The injection of an immiscible fluid at the center of a liquid-filled fracture results in the growth of the fracture and the outward displacement of the interface between the two liquids.

We study the dynamics of the fluid-driven fracture which is controlled by the competition between viscous, elastic, and toughness-related stresses. A model experiment is used to characterize the dynamics of the fracture for a range of mechanical properties of the fractured material and fracturing fluids. A liquid-filled pre-fracture is first formed in an elastic brittle matrix of gelatin. The displacing liquid is then injected. The radius and aperture of the fracture, and the position of the interface between the two liquids are recorded in the experiments.

In a typical experiment, the axisymmetric radial viscous flow is accommodated by the elastic deformation and fracturing of the matrix. We model the coupling between elastic deformation, viscous dissipation, and fracture propagation and recover the two fracturing regimes identified for single fluid injection. For the viscous-dominated and toughness-dominated regimes, scaling equations are derived that describe the crack growth due to a displacement flow and show the influence of the pre-existing fracture on the crack

dynamics through a finite initial volume and an average viscosity of the fluid in the fracture.

Chapter 4: Dynamics of fluid-driven fractures in layered materials

Fluid-filled fractures in underground formations allow large-scale energy and waste storage. Hydraulic fractures are, therefore, essential to various industrial processes ranging from oil and gas extraction to storage of carbon dioxide. The geological formations selected for storage commonly have a multilayered reservoir and caprock structure. Understanding fracture propagation in stratified formations is vital for performance and environmental impact assessment.

This chapter focuses on the analysis of fracture profiles ensuing from the injection of a low-viscosity fluid into a two-layer hydrogel block. The layers are characterized by different stiffness and are separated by an interface. Experimental findings highlight the influence of the initiating layer on fracture dynamics. Fractures that form in the softer layer are confined, with no penetration in the stiffer layer. Conversely, fractures initiated within the stiffer layer experience rapid fluid transfer into the softer layer when reaching the interface. We record the fracture geometry and pressure for different injection conditions to characterize the unexpected dynamics. We model the coupling between elastic deformation, material toughness, and volume conservation. After a short transient regime, scaling arguments capture the dependence of the fracture geometry on material properties, injection parameters, and time.

These results show that stiffness contrast can accelerate fracture propagation while extending its reach. These results have implications for climate mitigation strategies involving the storage of heat and carbon dioxide in stratified underground rock formations.

Finally, in chapter 5, we summarise the key points and results of the thesis and provide directions for future work.

1.3 Permissions and Attributions

1. The content of chapter 2 is in collaboration with Emilie Dressaire and Marie C. Sigallon, and has previously appeared in *Proceedings of the Royal Society A*. DOI: `http://doi.org/10.1098/rspa.2022.0460`.

2. The content of chapter 3 is in collaboration with Emilie Dressaire and has previously appeared in *Journal of Fluid Mechanics*. DOI: `https://doi.org/10.1017/jfm.2022.954`.

3. The content of chapter 4 is in collaboration with Emilie Dressaire and Marie C. Sigallon and is under preparation as a journal paper.

4. The content of Appendix A is the result of a collaboration with Nathan D. Jones and Emilie Dressaire and previously appeared in *ASME 2021 International Mechanical Engineering Congress and Exposition*. DOI: `https://doi.org/10.1115/IMECE2021-69668`.

Chapter 2

Dynamics of fluid-driven fractures in viscous dominated regime

2.1 Introduction

Hydraulic fracturing is a well-stimulation technique used to recover natural gas and oil from reservoirs with low permeability, such as shale formations. The US Environmental Protection Agency reports that the natural gas production from hydraulically fractured wells in the United States saw a 10-fold increase between 2000 and 2015 [44]. The formation of fractures in rocks has other applications, including carbon sequestration and geothermal energy extraction [45, 46]. It is estimated that almost 1 million wells have been hydraulically fractured since the 1940s. As hydraulic fracturing has become more prevalent, so has the need to characterize the associated risk to the local environment and populations. Over the past two decades, groundwater contamination and induced seismicity have been linked to hydraulic fracturing operations. Between 2000 and 2013, there was at least one hydraulically fractured well system within 1 mile of the water sources of 3900 public water systems in the continental United States [47]. The water

from these systems was distributed to more than 8.6 million people year-round in 2013. Another major concern is the induced earthquakes associated with hydraulic fracturing [48].

Earthquakes of magnitude 4.0 can be caused by the disposal of wastewater in fractured reservoirs [49, 50, 51, 5]. The associated risks increase as the distance between stimulated wells and groundwater wells or fault lines decreases. Therefore, understanding the dynamics of a fracture during and after the fluid injection is critical for risk assessment.

When a pressurized Newtonian fluid is injected from a point source into a uniform impermeable brittle matrix, a disk-like hydraulic fracture forms and propagates. This penny-shaped fracture results from the coupling of three mechanisms: (1) the elastic deformation of the fracture surfaces, (2) the propagation of the fracture at the rim of the fluid-filled region, and (3) the flow of the fluid in the fracture. Theoretical and numerical modeling of the penny-shaped crack has been developed since the seminal work of Sneddon & Mott [15]. Yet the fracture dynamics remain complicated to model owing to the multi-scale nature of the problem, [14, 52], with viscous dissipation associated with fluid transport through the volume and the stress concentration at the tip of the fracture. In limiting regimes, in which the viscous dissipation or the fracture opening controls the dynamics of the fracture, tip asymptotes can be defined [18, 53, 22, 20, 21, 54, 43].

In the viscous-dominated or zero-toughness regime, the elastic stresses drive the radial fracture propagation, which is limited by the viscous stresses. In the toughness-dominated regime, the stress concentration or stress intensity factor controls the fracture expansion, and the viscous stresses are negligible. To study the two-propagation regimes, laboratory-scale experiments use hydrogels, whose brittle elastic properties are analogous to those of rocks. For example, gelatin is a clear material that allows fracture visualization for a wide range of mechanical properties [28, 26]. Upon injection of an aqueous solution or oil

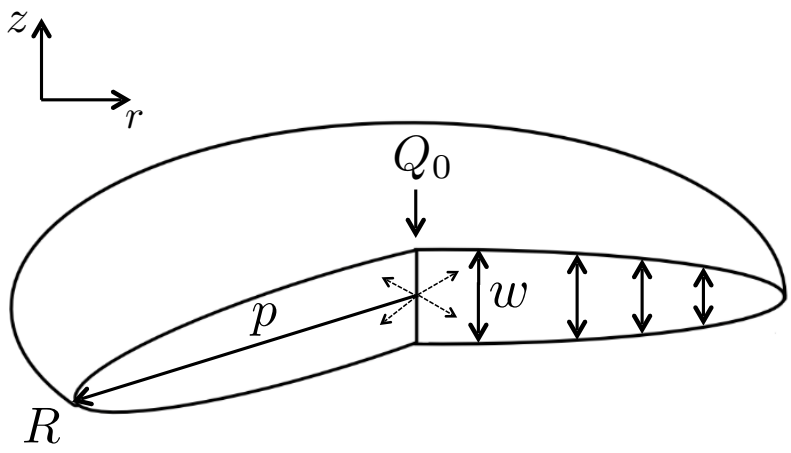

Figure 2.1: Diagram showing the radial fracture geometry.

from a needle, a penny-shaped fracture forms at the injection point and expands radially through the gelatin, perpendicularly to the needle. Radius and aperture measurements (see figure 2.1) in experimental model systems agree with the theoretical predictions during the fluid injection. [28, 26, 29, 32].

The dynamics of a fracture after the injection, i.e., post-shut-in, differs depending on the propagation regime [24]. Here we assume that the fracture propagates in a mobile equilibrium with no fluid lag. The influence of gravity on fracture propagation is negligible [55]. In the toughness-dominated regime, the fluid-filled fracture propagates when the stress intensity factor is equal to the toughness of the matrix. When the fluid injection stops, the elastic pressure is no longer sufficient to sustain the propagation of the fracture. In the toughness regime, the final geometry of the fracture is reached when the injection stops. In the viscous regime, however, the material's toughness does not limit the propagation of the fracture. The viscous dissipation in the fluid balances the elastic stresses during and after the injection. This chapter focuses on the dynamics of fractures that propagate in the viscous-dominated regime during and post-injection. Previous experimental studies have investigated the fracture dynamics during the in-

jection of a viscous fluid in a hydrogel matrix [28, 32] and the closure of the fracture post-injection in porous materials like cement and plaster with a typical Young's modulus of the order of 1 GPa [56]. Those studies characterized the decline in pressure inside the fracture post-shut-in, where the pressure decrease is due to various phenomena such as leak-off. Numerical studies predicted fracture growth and pressure reduction after shut-in in non-permeable matrices [57, 58]. Here, we conduct injection experiments in gelatin blocks to study the post shut-in dynamics of a fracture in the viscous regime. The fracture initially forms and propagates during the injection of a viscous Newtonian liquid. The injection is stopped, and we record the time dependence of the fracture radius and aperture until both properties become constant, indicating that the fracture has reached its equilibrium configuration. We observe that the fracture created in the viscous regime continues to propagate even after the injection stops. Consequently, we identify three different regimes of propagation in our experiments: (1) propagation during injection, (2) propagation post shut-in or at constant volume, and (3) saturation. To the best of our knowledge, the experiments presented here are the first observations for the three regimes in a hydrogel matrix, and the data agree well with the corresponding scaling laws [24, 56, 58].

This chapter is structured as follows. In §3, we discuss the experimental set-up and methods and our observations. In §4, we summarize the scaling arguments and derivation of the dimensionless parameters. The experimental results and theoretical predictions are compared in §5. Our conclusions are summarized in §6.

2.2 Experiments and observations

To study the fracture dynamics in the viscous-dominated regime, we inject a viscous liquid into a high Young's modulus and low toughness gelatin block. Using dyed silicone

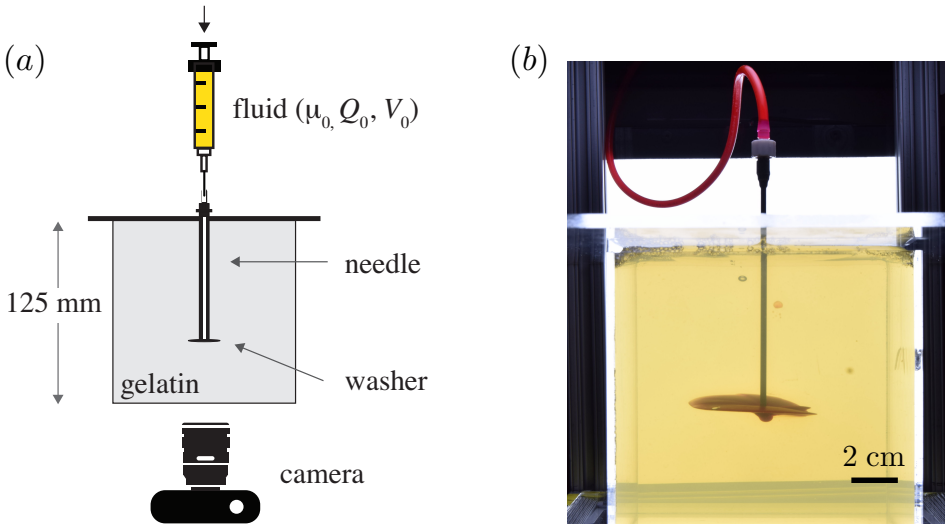

Figure 2.2: Experimental set-up: (a) schematic and (b) penny-shaped fracture formed by injecting silicone oil of viscosity $\mu = 10$ Pa.s at a flow rate $Q_0 = 10$ ml.min^{-1}) into a block of gelatin with a Young's modulus $E = 88$ kPa. The oil is dyed with a red oil-soluble food color.

oil, we can characterize the geometry of the fracture, i.e., its radius and aperture, as a function of the radial distance from the injection point during and after the injection.

2.2.1 Experimental methods

The gelatin is prepared by heating ultra-pure water to 60^{o}C and slowly adding gelatin powder (Gelatin type A; Sigma-Aldrich, USA) while mixing. The gelatin is then allowed to be set over 24 hours at room temperature in a cubic clear container (12.5 cm $\times$ 12.5 cm $\times$ 12.5 cm) around a blunt needle as represented in figure 2.2. The Young's modulus of the gelatin E is measured with cylindrical samples of height and diameter equal to 2.5 cm. The cylinders are tested under compression using a custom-built displacement-controlled load frame. The Young's moduli range between 88 to 144 KPa $\pm$10% for mass fractions of gelatin powder in water between 20 - 25%. The fracture energy and Poisson's ratio of the gelatin are assumed constant with $\gamma_S \approx 1$ J.m^{-2} and $\nu \approx 0.5$ respectively [38]. The inner diameter of the blunt needle is equal to 2.15 mm. A plastic washer of

diameter of about 6 mm is placed at the tip of the needle to ensure the propagation of the fracture in a plane perpendicular to the needle and parallel to the lens of the camera. We inject silicone oils of different viscosity μ to fracture the gelatin. Viscosity measurements are conducted using an MCR 92 Anton Parr rheometer with a parallel plate measuring system. The values obtained at 20^oC are listed in table 2.1 and have an error of $\pm 1\,\%$. We use a syringe pump (KDS Legato 200 series infusion syringe pump) to inject the fracturing fluid at a controlled flow rate Q_0 ranging from 5 to 28 ml.min^{-1}. The injection stops when a volume V_0 of fluid has been injected.

To ensure that the experiments are in the viscous regime, we estimate the ratio of the toughness-related pressure and the viscous pressure. This ratio is called the dimensionless toughness ($\mathcal{K}_s$), and its maximum value is reached at the time of shut-in [24]

$$\mathcal{K}_s = K' \frac{t_s^{1/9}}{E'^{13/18} \mu'^{5/18} Q_o^{1/6}}, \tag{2.1}$$

with the effective viscosity $\mu' = 12\mu$, the effective toughness $K' = 4\left(\frac{2}{\pi}\right)^{\frac{1}{2}} K_{IC}$, the toughness $K_{IC} = \sqrt{2\gamma_S E'}$ and the effective Young's modulus $E' = E/(1-\nu^2)$. The dimensionless toughness is of order 1 for all experiments as presented in table 1. We, therefore, expect the fracture propagation to be limited by the viscous dissipation associated with the fluid flow in the fracture.

The silicone oil is dyed using oil-based food color to help visualize the propagation of the fracture. The list of experiments and the corresponding parameters are summarized in table 2.1. The propagation of the fracture is recorded using a Nikon D5300 camera with a Phlox® LED panel ensuring uniform backlighting. The images are processed using a custom-made MATLAB code to determine the radius of the fracture R.

Exp.	Markers	E (kPa)	μ (Pa.s)	Q_0 (ml.min^{-1})	V_0 (ml)	$\mathcal{K}_s$
1	● / ○	88	10.3	15	6	1.6
2	◀ / ◁	88	10.3	5	6	2.17
3	▲ / △	88	10.3	10	6	1.79
4	▶ / ▷	88	10.3	25	4.3	1.34
5	▼ / ▽	88	10.3	28	4.3	1.30
6	◆ / ◇	88	10.3	15	8	1.65
7	⊠ / ✕	88	10.3	15	4	1.53
8	■ / □	88	20	25	3	1.06
9	⊞ / +	116	10.3	10	4	1.61
10	■ / □	144	10.3	20	3	1.23
11	■ / □	144	30	15	3.5	0.996

Table 2.1: List of Experiments. The markers on the left and right of the / symbol correspond to the data recorded during and after the injection respectively.

2.2.2 Thickness measurements

We use the light absorption technique pioneered by Bunger [59] to measure the fracture aperture using a soluble dye in the injected fluid. In our system, white light illuminates the sample and a filter is placed on the camera to measure the light intensity at a single wavelength. The filtered wavelength corresponds to the maximum absorbance of the dye. At this wavelength, the absorbance A_λ follows Beer's law:

$$A_\lambda = -\log_{10}\left(\frac{I_\lambda}{I_{\lambda,0}}\right) = \epsilon_\lambda c\, h \tag{2.2}$$

where $I_{\lambda,0}$ is the background intensity and I_λ is the intensity of light after it passes through a fluid layer of thickness h, with a dye concentration c. The fitting parameter ϵ_λ depends on the dye-fluid combination and the concentration and is obtained through calibration. Here, the fracturing fluid is dyed with Nile Red at a concentration of 0.2 g.L^{-1}, and the wavelength of the optical filter used was 632 nm. The value of the fitting parameter $\epsilon_\lambda c = 3.54 \times 10^{-3}$ mm^{-1} is obtained through the calibration process using liquid layers whose thickness ranges from 0.14 mm to 2 mm.

2.2.3 Observations

During the injection process, the fracture forms at the tip of the needle and propagates along the washer and beyond, expanding radially. Figure 2.3 presents a time series of the fracture propagation (see also electronic supplementary material, Movie S1). As the fracture grows radially, its thickness w increases as its color becomes darker. When the injection stops, the fracture expands radially at a slower pace. As the fracture grows, its color fades, indicating that the aperture decreases with time. Since the amount of fluid in the fracture needs to be conserved, as the radius increases, the width of the fracture decreases. Finally, the fracture stops growing. The radius R of the fracture vs time for the experiments listed in the table 2.1 is plotted in figure 2.4(a). To ensure that the finite volume of material and the bounding container walls are not affecting fracture growth, we experimented with a larger volume of gelatin (see Appendix 2.1 of the chapter for more details). The maximum fracture radius is independent of the size of the gelatin block, indicating that the viscous-dominated fracture stops expanding when it reaches equilibrium.

2.3 Scaling arguments

The fracture results from the injection of a high-viscosity Newtonian fluid in a brittle elastic matrix that is impermeable. We assume there is no lag between the fracture tip and the fluid front. The fracture is initially driven by an incompressible fluid of viscosity of μ pumped at a constant flow rate Q_0. The elastic medium is characterized by Young's modulus E, Poisson's ratio ν, and toughness K_{IC}. The injection through a point source leads to the formation and radial propagation of a penny-shaped fracture with no lag between the fluid and the fracture tip, as represented in figure 2.1. The experiments conducted in this study are in the viscous-dominated regime during the injection. The

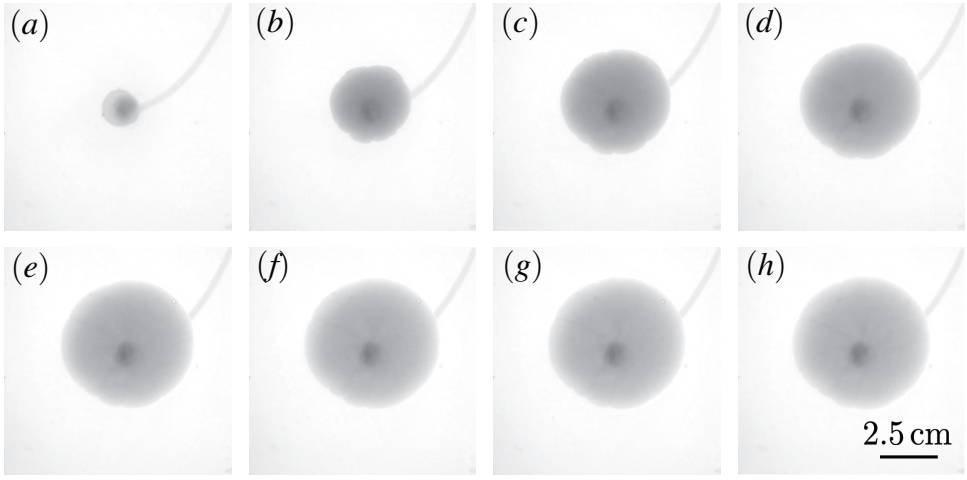

Figure 2.3: Fracture growth during and after the injection. The fluid is dyed with red food color to enhance the contrast. The grayscale images presented here are obtained by filtering the red channel from the color images. The first images are recorded during the injection: (a) $t = 0$ s, (b) $t = 18$ s, (c) $t = 36$ s. The fracture continues to grow after the injection stops (d) $t = 54$ s, (c) $t = 126$ s, (f) $t = 198$ s, (g) $t = 270$ s. The recording ends when the fracture has reached its equilibrium configuration (h) $t = 396$ s. The experimental parameters are: Young's modulus $E = 88$ KPa, flow rate $Q_0 = 10$ ml/min, volume injected $V_0 = 6$ ml and fluid viscosity $\mu = 10$ Pa.s.

viscous dissipation associated with fluid transport in the fracture limits growth. The material toughness is negligible and does not contribute to the fracture dynamics during the injection.

The evolution of the radius and width of the fracture in the viscous dominated regime can be modeled using scaling arguments, derived for both the injection and post "shut-in" stages of the propagation [22, 24] We make the following assumptions: (i) the stresses at the crack tip are well described by Linear Elastic Fracture Mechanics (LEFM), (ii) the lubrication theory can be used to model the flow; (iii) the fracture propagates continuously in a mobile equilibrium; and (iv) the matrix is impermeable (no leak-off). To describe the fracture aperture $w(r, t)$, radius $R(t)$, and pressure $p(r, t)$, we solve the coupled equations that describe (a) the viscous flow of the fracturing fluid in the time-dependent fracture, see equation (2.3), (b) the elastic deformation of the solid material, see equation (2.4), (c) the fracture propagation criteria based on LEFM, see equation (2.5), and the global

mass balance or fluid mass conservation, see equations (2.6) or (2.7). The net pressure couples these equations. The non-dimensional forms of the equations are summarised below, and a detailed derivation is provided in Appendix 2.2 of the chapter. The equations are non-dimensionalized with $R = R_o\hat{R}$, $w = w_o\hat{w}$, $p = p_o\hat{P}$, and $t = t_o\hat{t}$, where R_o, w_o, p_o and t_o represent the characteristic radius, aperture, pressure of the fracture and timescale of the propagation, respectively. As proposed by Savitski and Detournay [22], we define the effective viscosity $\mu' = 12\mu$, the effective toughness $K' = 4\left(\frac{2}{\pi}\right)^{\frac{1}{2}} K_{IC}$ and the effective Young's modulus $E' = E/(1-\nu^2)$. The dimensionless lubrication equation writes [32]:

$$\frac{\partial \hat{w}}{\partial \hat{t}} = \frac{t_0 w_0^2 p_0}{\mu' R_0^2} \frac{1}{\hat{r}} \frac{\partial}{\partial \hat{r}} \left(\hat{r} \hat{w}^3 \frac{\partial \hat{p}}{\partial \hat{r}} \right). \tag{2.3}$$

The elastic deformation leads to the following:

$$\hat{w} = \frac{8}{\pi} \frac{p_0 R_0 \hat{R}}{w_0 E'} \int_{\hat{r}/\hat{R}}^{1} \frac{\xi}{\sqrt{\xi^2 - (\hat{r}/\hat{R})^2}} \int_0^1 \frac{x\hat{p}}{\sqrt{1-x^2}} \mathrm{d}x\mathrm{d}\xi. \tag{2.4}$$

The fracture propagation requires:

$$\frac{K'}{p_0 R_0^{1/2}} = \frac{2^{7/2}}{\pi\sqrt{\hat{R}}} \int_0^{\hat{R}} \frac{\hat{p}}{\sqrt{\hat{R}^2 - \hat{r}^2}} \hat{r} \ \mathrm{d}\hat{r}. \tag{2.5}$$

Since the gelatin is considered impermeable, the volume of the fracture is equal to the volume of fluid injected. During the injection, the volume of the fracture is equal to

$$\hat{Q}\hat{t} = 2\pi \frac{R_0^2 w_0}{Q_0 t_0} \int_0^{\hat{R}} \hat{r}\hat{w} \ \mathrm{d}\hat{r}. \tag{2.6}$$

The injection stops when the fracture volume is equal to $V_0 = Q_0 t_0$. After the injection, the volume of the fracture is:

$$\hat{V} = 2\pi \frac{R_0^2 w_0}{V_0} \int_0^{\hat{R}} \hat{r}\hat{w} \, \mathrm{d}\hat{r}. \tag{2.7}$$

To determine the fracture dynamics during and after the injection, we now solve the sub-set of equations relevant to each stage of fracture propagation.

2.3.1 Viscous regime: constant flow rate propagation

To obtain the scaling relations that describe the fracture dynamics during the injection at a constant flow rate, we assume that the major form of dissipation of energy in the fracture is the viscous dissipation of the fluid flow. We set the dimensionless parameters in equations (2.3), (2.4) and (2.6) equal to 1. We recover the scaling relations for the radius R_o and aperture w_o of the fracture originally derived by Savitski and Detournay [22]:

$$R_0 \approx \left(\frac{Q_0^3 E' t_0^4}{\mu'} \right)^{1/9} \tag{2.8}$$

$$w_0 \approx \left(\frac{\mu'^2 Q_0^3 t_0}{E'^2} \right)^{1/9} \tag{2.9}$$

During the injection, both the radius and the aperture are increasing functions of time, which is consistent with our observations.

2.3.2 Viscous regime: propagation at constant volume

Once the injection is complete, the volume inside of the fracture is constant [24]. The viscous dissipation of the fluid is assumed to be the limiting factor in the propagation

of the fracture. Setting the dimensionless parameters of equations (2.3), (2.4) to 1 and (2.7) and solving for the characteristic radius R_0 and aperture w_0, we get:

$$R_0 \approx \left(\frac{V_0^3 E' t_0}{\mu'}\right)^{1/9} \tag{2.10}$$

$$w_0 \approx \left(\frac{\mu'^2 V_0^3}{E'^2 t_0^2}\right)^{1/9}. \tag{2.11}$$

The radius is still increasing with time, at a slower rate than during the injection. The aperture of the fracture is now a decreasing function of time. This is consistent with the fact that the total volume of fluid in the fracture ($\propto R_0^2 w_0$) needs to be conserved, independent of time.

2.3.3 Toughness regime: saturation

Based on the scaling relations derived for the viscous regime, the fracture radius is an increasing function of time at constant fracture volume. Yet, the elastic pressure in the fracture is a decreasing function of time, as the wall deformation decreases. Eventually, the material toughness is no longer negligible. Indeed, if the pressure in the fracture is too low, the material no longer fractures and the propagation of the fracture stops. We assume that saturation, unlike the previous two stages of propagation, is controlled by the fracture opening or material toughness. The fracture opening criterion as a function of the pressure and stress intensity factor is given by equation (2.5). This equation coupled with the elastic stress in the gelatin matrix, equation (2.4) and the volume conservation of the fracture, equation (2.7) leads to the following scaling [24]:

$$R_0 \approx \left(\frac{V_0 E'}{K'}\right)^{2/5} \tag{2.12}$$

$$w_0 \approx \left(\frac{K'^4 V_0}{E'^4}\right)^{1/5}. \tag{2.13}$$

Where, $K' = 4\left(\frac{2}{\pi}\right)^{1/2} K_{IC}$. The radius and the aperture of the fracture are now functions of the volume of fluid and mechanical properties of the matrix. They are independent of time.As the material toughness increases, the arrest radius decreases because it is more difficult to create a new fracture surface.

2.4 Results and observations

In the following section, we report quantitative experimental results, and their comparison with the scaling arguments derived above for both the radius and width of the fracture.

2.4.1 Radius measurements

We first measure the radius of the fracture as a function of time for the experimental parameters summarized in table 2.1. The raw experimental data are shown in figure 2.4(a). The solid symbols correspond to the values recorded during the injection. In contrast, the open markers indicate that the data were recorded after the injection. For some of the experiments, such as experiment 8, we see a 50 % increase in the radius of the fracture after the injection stops.

We successively rescale the data using the scaling laws derived above and obtain figures 2.4(b-d), where the fit line is shown in black. On the log-log plot, the slope of the line is set to the value of the power-law derived using scaling arguments. The y-intercept is obtained by minimizing the mean squared error and corresponds to the prefactor, which can be predicted theoretically [21]. The propagation dynamics exhibit three stages described by (i) the viscous-dominated propagation during the injection, (ii) the viscous-dominated propagation at constant volume after the injection stops, and (iii) a toughness-controlled saturation. For the fracture dynamics during the injection [regime

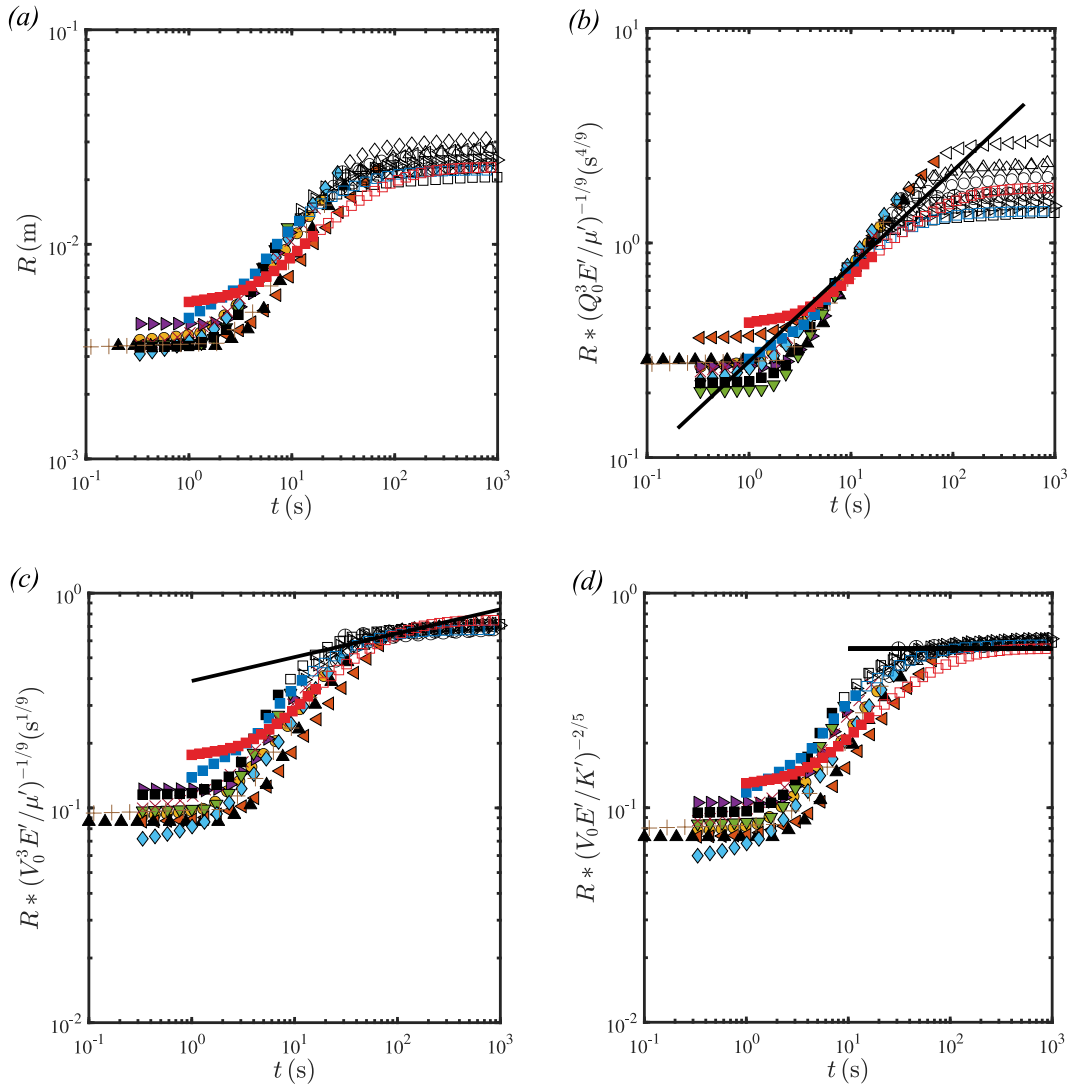

Figure 2.4: Radius of the fracture formed during experiments 1-9, see table 2.1 for corresponding parameters. Data collected during and after the injection are displayed with solid and open symbols, respectively. (a) The radius of the fracture over time. (b) Rescaled radius using equation (2.8) for the regime (i) as a function of time. (c) Rescaled radius using equation (2.10) for the regime (ii) as a function of time. (d) Rescaled radius using equation (2.12) for the regime (iii) as a function of time. For each regime, the best fit line is represented by a solid black line.

(i) and figure 2.4(b)], we rescale the data using the viscous scaling. After the early times that correspond to the fracture formation and its propagation over the washer, the data points collapse onto a best-fit line which has a prefactor, $k_1 = 0.28$ and an exponent,

$\alpha_1 = 4/9$ where

$$R(t) = k_1 \left(\frac{E' Q_0^3}{\mu'} \right)^{1/9} t^{\alpha_1}. \tag{2.14}$$

The theoretical prefactor derived by Savitski and Detournay [21] is equal to 0.7. The low value of the prefactor obtained in our experiments is consistent with measurements previously reported for the viscous-dominated regime [28, 32].

In the next regime [regime (ii) and figure 2.4(c)], the fracture fluid continues to propagate after the injection stops, and the open symbols collapse on the best fit line

$$R(t) = k_2 \left(\frac{E' V_0^3}{\mu'} \right)^{1/9} t^{\alpha_2}, \tag{2.15}$$

which has a prefactor $k_2 = 0.39$ and an exponent, $\alpha_2 = 1/9$. The results indicate that the propagation continues to be dominated by viscous dissipation. For time values above 100 s, the increase in radius no longer follows the best fit line: the radius reaches its maximum or equilibrium value.

In the saturation regime, regime (iii), and figure 2.4(d)], we rescale the data using the volume of the fracture and the mechanical properties of the gelatin matrix. All data collapse on an average value represented with a horizontal line whose y-intercept $k_3 \approx 0.58$ where,

$$R(t) = k_3 \left(\frac{E' V_0}{K'} \right)^{2/5}. \tag{2.16}$$

The experimental prefactor of 0.58 is comparable to the expected theoretical prefactor of 0.85 [24]. This result indicates that the propagation controlled by the viscous dissipation stops when the stress intensity factor at the tip of the fracture is too low to sustain the formation of the fracture.

The time dependence of the radius demonstrates the succession of three regimes of fracture propagation: growth at constant flow rate, growth at constant volume and

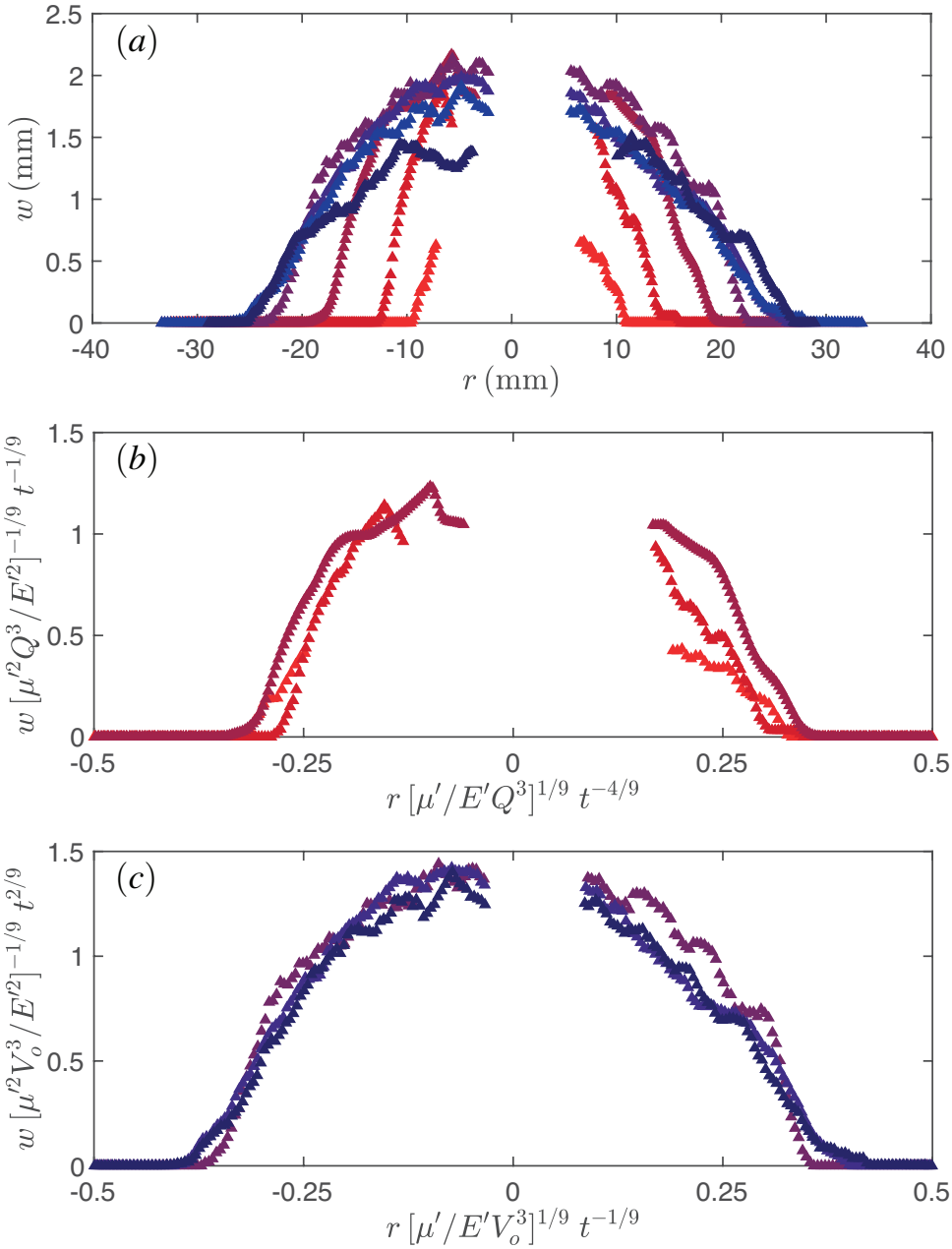

Figure 2.5: (a) Fracture profiles measured during and after the injection for $t = [9, 21, 33, 81, 105, 117, 762]$ s with time increasing from clear red to dark blue. (b) Rescaled fracture profiles using the scaling laws derived for the injection in §2.1. (c) Rescaled fracture profiles using the scaling laws derived for the constant volume propagation in §2.2. Experimental parameters: $E = 88$ KPa, $Q_0 = 10$ ml.min^{-1}, $V_0 = 6$ ml, and $\mu = 10$ Pa.s

saturation. The growth of the fracture at constant volume is characterized by its duration and the relative change in fracture radius. The duration and the relative change in radius decrease as the dimensionless toughness of the injection increases [24]. Indeed the larger the value of κ_s, the closer to the toughness regime the injection is. The fracture is arrested immediately after the injection stops for a cut-off value of $\mathcal{K}_s = 2.5$. For the experiments conducted in this study, the $\mathcal{K}_s$ values have been listed in table 2.1 and range between 0.996-2.17, which explains why the growth at constant volume lasts a few minutes for a relative change in radius is about 50%.

2.4.2 Thickness measurements

To further characterize the three propagation regimes, we measure the fracture aperture with the dye absorption method and plot the profiles of the fractures in figure 2.5. During the injection, both the radius and aperture of the fracture increase. Upon rescaling, the data collapse on a self-similar fracture profile, after an initial transient regime, as shown in figure 2.5(b). After the injection, the radius of the fracture increases as the aperture decreases. The rate of propagation is slower than it was during the injection. Upon rescaling, all data collapse on a second self-similar profile which corresponds to the viscous propagation of a fracture of constant volume (see figure 2.5(c)).

2.5 Conclusion

As a pressurized fluid is injected in an elastic brittle material, a penny-shaped fracture forms and propagates. The complex fracture dynamics depend on the matrix and fluid properties and the injection parameters. During the fluid injection, modeling and experimental studies have demonstrated two asymptotic regimes. The fracture expansion is either controlled by the viscous dissipation in the fluid, in the viscous-dominated regime

or the toughness of the material, in the toughness-dominated regime. Upon shut-in, the continued propagation of the fracture at constant volume has been observed in porous materials and predicted for impermeable matrices. In this study, we experimentally study the propagation regimes of a viscous-dominated fracture in a hydrogel matrix. We demonstrate the existence of three propagation regimes: injection growth, post shut-in propagation, and saturation. For each regime, we show a good agreement with the scaling laws derived for the growth of fractures in the viscous-dominated regime during injection at a constant flow rate and post shut-in. The saturation values of the fracture radius and aperture are reached when the stress intensity factor at the tip of the fracture becomes lower than the material's toughness. The experimental results and corresponding model allow for predicting the relative growth of the fracture after the injection stops, i.e., the final size of the fracture and how long it takes for the fracture to reach this equilibrium geometry once the injection stops.

Data availability statement

The datasets supporting this article have been uploaded as part of the supplementary material [60].

Author contributions

S.S.T.: conceptualization, data curation, formal analysis, investigation, visualization, writing—original draft and writing—review and editing; M.S.: investigation, visualization, and writing—review and editing; E.D.: conceptualization, formal analysis, funding acquisition, methodology, investigation, visualization, writing—original draft and writing—review and editing, project administration, resources, software, supervision.

Acknowledgements

We thank Z. Zheng for helpful discussions. This research was supported in part by the ACS PRF (grant no. 60464-ND9).

Appendix 2.1: Effect of box dimensions

All experiments are conducted in a 12.5 cm × 12.5 cm × 12.5 cm block of gelatin set in an acrylic box of the same dimensions. To test the influence of the box size or edge effects on the fracture dynamics and the saturation radius, we performed experiment 3 (see table 2.1 for experimental parameters in a larger volume of gelatin of dimensions 15 cm × 15 cm × 15 cm. The radius of the fracture is recorded over time and plotted in fig.2.6, for the two block sizes. The results demonstrate that the evolution of the radius does not depend on the size of the block of gelatin. The saturation radius is not set by edge effects.

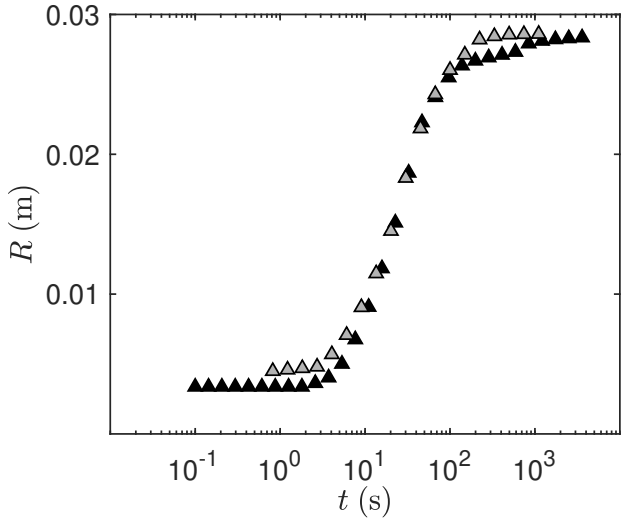

Figure 2.6: Influence of matrix dimensions on fracture propagation. Radius vs time for experiment 3 (see table 2.1 for experimental parameters) conducted in a box of size 12.5 cm × 12.5 cm × 12.5 cm (▲△) and a box of size 15 cm × 15 cm × 15 cm (▲△).

Appendix 2.2: Governing equations

We review the mathematical derivations that define the radius and aperture of penny-shaped fracture driven by a fluid [32].

The mechanical deformation in the elastic matrix associated with the fracture thickness w relates to the pressure p in the fracture and the fracture radius R through the following integral relation, initially derived by Sneddon & Lowengrub [61].

$$w(r,t) = \frac{8R}{\pi E'} \int_{r/R}^{1} \frac{\xi}{\sqrt{\xi^2 - (r/R)^2}} \int_0^1 \frac{xp(x\xi R, t)}{\sqrt{1-x^2}} \, \mathrm{d}x \, \mathrm{d}\xi. \tag{2.17}$$

To describe the fluid flow in the fracture, we use the non-linear lubrication equation called the Reynolds equations [62] which relates the aperture of the fracture to the pressure and the fracture radius.

$$\frac{\partial w(r,t)}{\partial t} = \frac{1}{12\mu} \frac{1}{r} \frac{\partial}{\partial r} \left(r w^3(r,t) \frac{\partial p}{\partial r} \right) \tag{2.18}$$

The stress intensity factor K_I defines the stress concentration at the tip of the fracture. The fracture propagates if the stress intensity factor K_I is equal to K_{IC}, i.e., the material toughness. For a penny-shaped fracture, the stress intensity is equal to [63]:

$$K_I = \frac{2}{\sqrt{\pi R}} \int_0^{R(t)} \frac{p(r,t)}{\sqrt{R^2 - r^2}} r \, \mathrm{d}r. \tag{2.19}$$

where r is the radial distance from the center of the fracture (refer to figure 2.1) .

The boundary conditions are set by the fracture geometry. The integral representation of the fluid mass conservation in the fracture is in equation (2.20). The fracture thickness at the tip is 0, equation (2.21). There is no flow through the tip of the fracture in the

elastic medium, equation (2.22).

$$Qt = 2\pi \int_0^{R(t)} rw(r,t)\mathrm{d}r \tag{2.20}$$

$$w = 0, \quad r = R(t) \tag{2.21}$$

$$w^3(r,t)\frac{\partial p(r,t)}{\partial r} = 0, \quad r = R(t) \tag{2.22}$$

In this study, this set of coupled equations and boundary conditions are used to derive scaling laws for the fracture radius and aperture.

Chapter 3

Axisymmetric displacement flows in fluid-driven fractures

3.1 Introduction

Fluid-driven or hydraulic fracturing results from the injection of a pressurized fluid in low permeability solid media. The formation and propagation of the fluid-filled tensile fracture is commonly observed in engineering and natural geophysical processes. For example, the formation of magma-driven dykes is due to density differences that generate pressure large enough to propagate a vertical fracture in the surrounding rock [55, 64]. The most common industrial application of hydraulic fracturing is well stimulation to facilitate the extraction of oil and gas from shale formations [65]. A fluid is injected at high pressure to expand fractures initiated with small-scale explosions in unconventional reservoirs. The fractures constitute new flow pathways, facilitating fluid transport and storage in low permeability and low porosity rock formations. Other applications leverage the enhanced transport. For example, fractures connecting wells can be used to extract geothermal energy as the fluid pumped through the fracture heats up as it

travels underground [66, 46, 67]. Fractures are also used for storage, including carbon sequestration [45, 68] and disposal of liquid waste [69, 70].

The complex mechanics of fluid-driven fractures are controlled by the deforming boundary, fluid flow and stress singularity at the tip of the tensile fracture [14]. Field testing, laboratory-scale experiments, and predictive modelling evidence that the fracture propagation is characterized by multiple length and time scales. When a Newtonian fluid is injected from a point source, in an infinite, homogeneous, and impermeable medium, a single fracture propagates radially. The elastic stress in the medium leads to the growth of a penny-shaped fluid-filled fracture in the direction of minimum confining stress. The propagation of such fractures has been studied extensively as it is essential to the modelling of more complex geological situations, including those involving a finite medium [25], complex fluids [71, 72, 34], and interacting fractures [33]. Seminal work on the stress distribution in a penny-shaped fracture [15] and the injection of viscous fluids to form fractures [16, 17] led to the development of self-similar solutions for fractures whose propagation is limited by the viscous dissipation in the fluid [18]. Further work on the vicinity of the crack front or tip region identified two asymptotic regimes for the tip geometry and fracture propagation [19, 20, 23, 22, 21]. In the viscous-dominated scaling, the viscous dissipation in the flow opposes the elastic stress of the deformable boundary to control the fracture evolution. In the toughness-dominated regime, the material toughness opposes the elasticity-driven propagation of the fracture and determines the system's behaviour. Laboratory-scale experiments commonly rely on clear brittle elastic gels to study the crack tip region and the penny-shaped fracture [37, 39, 43, 73]. Injections of water, glycerol, and oil in gelatin and polyacrylamide have validated the existence of two propagation regimes and the corresponding scaling laws [28, 29, 32]. The behaviour of the crack tip region was studied by injecting liquid between two plates of polymethylmethacrylate (PMMA) glued by an adhesive [26].

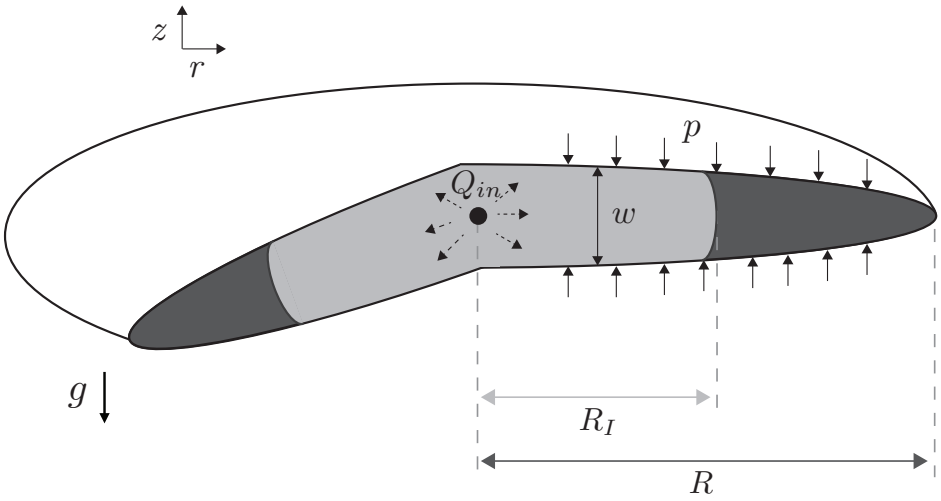

Figure 3.1: Schematic of a penny-shaped fracture formed by successively injecting two liquids, first the outer fluid (dark gray) and then the inner fluid (light gray). The fracture is axisymmetric.

Most hydraulic fracturing processes involve multiphase flows and in particular, displacement flows [72, 52, 34, 74, 75]. During hydraulic fracturing operations several fluids are injected ranging from low-viscosity fluids to high-viscosity polymer solutions [76, 75] and proppant slurries [72, 74, 77]. This sequence of injections aims at increasing the surface area of the fracture and at keeping the fracture open during the hydrocarbon extraction. For example, carbon dioxide injection is a promising strategy to enhance oil recovery after primary production of shale oil reservoirs [45, 68]. The rapid injection of supercritical CO_2 in water-filled fractures is followed by the slower permeation of CO_2 into the rock and the migration of the oil into the fracture. This strategy increases the amount of oil recovered while storing carbon in the rock. Finally enhanced geothermal systems rely on fractures in hot rocks to connect the injection and extraction wells [66, 46, 78]. Fracturing fluids are injected first, and then the working fluid, commonly water or CO_2 is pumped into the fracture to extract heat.

Displacement flows in porous media can give rise to complex out-of-equilibrium flow patterns when the invading fluid has a lower viscosity than the fluid which occupies the

porous medium, and is referred to as the displaced or defending fluid. Practically, the patterns generated by liquid-liquid or gas-liquid displacement flows lead to preferential flow pathways in the porous medium. Extensive work has therefore been dedicated to the formation and geometry of the patterns, ranging from experimental to numerical and theoretical [79, 80, 81, 82, 83, 84, 85, 86]. Viscous and capillary forces can contribute to fluid/fluid displacement in a porous medium. A displacement flow is characterized by two dimensionless parameters: the viscosity or mobility ratio $M = \mu_{inv}/\mu_{def}$ and the capillary number of the invading fluid $Ca = \mu_{inv}u/\gamma$ where μ_{inv} and μ_{def} are the viscosities of the invading and defending fluids, respectively, u is the characteristic velocity and γ is the surface tension of the interface between the two fluids. The influence of the two dimensionless parameters on the geometry of the invading front is summarized in Lenormand's phase diagram [84], which was recently revisited by Primkulov *et al.* (2021) [87] to include wettability. In summary, for large Ca, the viscous forces control the system dynamics and the interfacial forces are negligible. If the invading fluid is more viscous than the defending fluid ($M \geq 1$), a compact front or interface moves through the porous medium. If the invading fluid is less viscous than the defending one ($M << 1$), the Saffman-Taylor instability leads to an unstable front with the formation of a viscous fingering pattern, observed in porous media of different complexity, from Hele shaw cells [79, 88] to intricate networks of pores and throats [89, 90]. For low Ca, the interfacial forces contribute to the system dynamics and result in more complex patterns at the interface between the two fluids, depending on the local pore geometry and wettability [91, 92]. The rich dynamics of displacement flows is reported in various model porous media, including networks of microchannels and rough fractures [93, 94, 95]. Yet, the system geometry can delay the onset of viscous fingers and even suppress the Saffman-Taylor instability. In a converging Hele-Shaw cell, the stability of the interface depends on the mobility ratio, but also the characteristic velocity, the gradient of cell depth,

and the contact angle at the interface [96, 97, 98]. Below a critical capillary number, a compact front is observed in a converging Hele-Shaw cell despite the unfavourable nature of the displacement. Similar results are reported in flexible cells, whose geometry depends on elastohydrodynamic interactions, such as displacement flows under elastic membranes [99, 100, 101, 102]. Two physical mechanisms contribute to the stabilization of the interface under an elastic membrane that deforms as fluid is injected. Firstly, the local increase in cell depth leads to a depth gradient which has been shown to delay viscous fingering for rigid converging cells. Secondly, the increase in depth reduces the characteristic velocity or capillary number corresponding to a given injection flow rate.

The purpose of the present chapter is to model axisymmetric two-phase flows in fluid-filled growing fractures. Experiments and theoretical modelling focus on immiscible two-phase flows with a mobility ratio smaller than or of order 1 and a low capillary number, ensuring the propagation of a compact front. We build on the approach of Savitski & Detournay (2002) [22] to study the coupling between the two-phase flow and the fracture growth, in the viscous and toughness regimes (§ 3.3). We derive new scalings for the radius and aperture of the fracture and the position of the interface for immiscible displacement flows in elastic, brittle, and impermeable media (§ 3.4). To test the scalings, we conduct injection experiments in gelatin, which is a common model medium (§ 3.5). During the two consecutive injections, we record the geometrical parameters of the fracture and compare their time dependence with scalings (§ 3.6). Finally, we discuss the timescales of the fracturing displacement flow (§ 3.7).

3.2 Theoretical models

In this section, we model the displacement flow that is responsible for the propagation of a crack during the successive injections of two immiscible fluids. The mathematical

models presented build on the framework originally introduced by Spence & Sharp (1985) [18] and further developed in recent studies of single fluid injection [22, 28, 32]. Past work has focused on the injection of a single incompressible fluid in an elastic brittle solid through a point source (see figure 3.1), forming a penny-shaped crack. The fracture dynamics depend on the material properties, such as the Young's modulus E, Poisson's ratio ν, and toughness K_{IC}, and the injection parameters, i.e. the constant flow rate Q and liquid viscosity μ. As the injection stops, the fracture reaches its final configuration and volume V_0.

This study addresses the injection of an immiscible liquid in a pre-formed penny-shaped crack. The fluid is injected through the same point source at the centre of the penny-shaped crack. The displaced fluid fills an outer annular region of the fracture (see figure 3.1). In what follows, we use the subscript "in" to refer to the injected liquid and "o" to the displaced fluid. The surface tension of the interface is noted γ and the contact angle with the solid θ. Over the timescale of an experiment, typically a few minutes, the solid is not porous to the liquids and the volume of the fracture is equal to the total volume of fluid injected.

We make assumptions regarding fluid flow and fracture propagation to model the system dynamics. As the injection rates are low, we assume that the fracture propagates at equilibrium and the liquid and fracture fronts coincide at all times, with no fluid lag. The fluid injection results in linear elastic deformation of the surrounding material.

To describe the crack aperture $w(r,t)$, radius $R(t)$ and pressure $p(r,t)$, as well as the position of the interface R_I, we need to solve the coupled equations that describe (a) the viscous flow of the two fluid phases in the time-dependent fracture, (b) the elastic deformation of the solid material or fracture walls, (c) the stress intensity factor at the tip of the fracture, and (d) the volume conservation. These sets of equations are coupled by the net pressure in the fracture. The fluid domain is divided into two regions. The

outer region is composed of the displaced fluid and bound by the liquid-liquid interface at $r = R_I$ and the crack tip at $r = R$. The injected fluid fills the inner region of the crack from the injection point to the fluid-fluid interface at $r = R_I$. Both regions are axisymmetric as shown in figure 3.1.

3.2.1 Fluid flow in the crack

3.2.1.1 Lubrication theory

The low Reynolds number flow in the elongated fracture allows to simplify the Navier Stokes equation and use lubrication theory. The fluid is injected in a pre-formed crack whose aspect ratio is small:

$$w << R. \tag{3.1}$$

The Reynolds number of the flow through the crack is defined for the injected fluid as

$$Re = \epsilon \frac{\rho\, U\, w}{\mu} = \frac{\rho_{in} Q_{in} w(r=0)}{2\pi \mu_{in} R^2} \leq 1, \tag{3.2}$$

where ϵ is the aspect ratio of the crack. As a result the flow of both fluids can be modeled with the lubrication theory, similarly to the single-phase flows in a penny-shaped fracture [22, 103, 104, 28, 32]. For the 2-fluid system, the lubrication equations write:

$$\frac{\partial w(r,t)}{\partial t} = \frac{1}{12\mu_{in}} \frac{1}{r} \frac{\partial}{\partial r} \left(r w^3(r,t) \frac{\partial p}{\partial r} \right) \text{ for } 0 \leq r \leq R_I \tag{3.3}$$

$$\frac{\partial w(r,t)}{\partial t} = \frac{1}{12\mu_0} \frac{1}{r} \frac{\partial}{\partial r} \left(r w^3(r,t) \frac{\partial p}{\partial r} \right) \text{ for } R_I \leq r \leq R \tag{3.4}$$

3.2.1.2 Liquid interface

The interface between the two fluids moves outward during the injection and is described by the dynamics boundary condition:

$$\boldsymbol{n}\cdot\left(-p^{-}\boldsymbol{I}+\mu_{in}\left(\nabla\,\boldsymbol{u}^{-}+(\nabla\boldsymbol{u}^{-})^{\mathrm{T}}\right)\right)\cdot\boldsymbol{n}+\gamma\kappa=\boldsymbol{n}\cdot\left(-p^{+}\boldsymbol{I}+\mu_{0}\left(\nabla\,\boldsymbol{u}^{+}+(\nabla\boldsymbol{u}^{+})^{\mathrm{T}}\right)\right)\cdot\boldsymbol{n} \quad (3.5)$$

where $\mathbf{n} = \mathbf{e_r}$ is the vector normal to the interface and κ the sum of the principal curvatures of the interface. The $+$ and $-$ exponents indicate that the value of the variable is determined at $r = R_I + \epsilon$ and $r = R_I - \epsilon$ respectively with $\epsilon << R_I$. We note $\boldsymbol{\tau} = \mu\left(\nabla\boldsymbol{u} + (\nabla\boldsymbol{u})^{\mathrm{T}}\right)$. We assume that the fluids are perfectly wetting the gel and neglect the thin film deposited by the outer fluid. The normal stress balance writes

$$\begin{aligned} p^{-} - p^{+} &= \sigma_I = \gamma\left(\frac{1}{R_I}+\frac{2}{w_I}\right) - \mathbf{n}\cdot\left(\boldsymbol{\tau}^{+}-\boldsymbol{\tau}^{-}\right)\cdot\mathbf{n} && (3.6)\\ &= \gamma\left(\frac{1}{R_I}+\frac{2}{w_I}\right) - 2\mu_0\frac{\partial u}{\partial r}|_{r=R_I^{+}} - 2\mu_{in}\frac{\partial u}{\partial r}|_{r=R_I^{-}}, && (3.7)\end{aligned}$$

where w_I is the width of the fracture at the interface. The expression can be further simplified as $R_I > w_I$ and the viscous normal stresses are negligible. Indeed the capillary number of the invading fluid is

$$Ca_{in} = \frac{\mu_{in}\,U}{\gamma} = \frac{\mu_{in}Q_{in}}{2\gamma\pi R\,w(r=0)} << 1. \quad (3.8)$$

The pressure change across the interface is:

$$p^{-} - p^{+} \approx \frac{2\gamma}{w_I}. \quad (3.9)$$

As the fluid-fluid interface moves, we can write the following kinematic condition using Reynolds equations:

$$q^- = q^+ = -\frac{w_I^3}{12\mu_{in}}\frac{\partial p}{\partial r}|_{r=R_I^-} = -\frac{w_I^3}{12\mu_0}\frac{\partial p}{\partial r}|_{r=R_I^+}. \tag{3.10}$$

3.2.1.3 Volume conservation

Finally, through volume conservation, the volume of the crack is equal to the volume injected. We note V_0 the volume of the pre-fracture which is equal to the volume of the outer fluid. The injection begins at $t = 0$:

$$V_0 + Q_{in}\, t = 2\pi \int_0^R r w(r,t) dr, \tag{3.11}$$

and

$$Q_{in}\, t = 2\pi \int_0^{R_I} r w(r,t) dr. \tag{3.12}$$

3.2.2 Fracture equations

3.2.2.1 Linear elasticity

Similarly to the single-fluid fracture [22], the linear elasticity equation writes

$$w(r,t) = \frac{8\,(1-\nu^2)\,R}{\pi E} \int_{r/R}^1 \frac{\xi}{\sqrt{\xi^2 - (r/R)^2}} \int_0^1 \frac{xp(x\xi R, t)}{\sqrt{1-x^2}}\, \mathrm{d}x\, \mathrm{d}\xi. \tag{3.13}$$

3.2.2.2 Fracture propagation

In a small region at the tip of the crack, the material undergoes plastic deformation. The tensile fracture propagates when the mode I stress intensity factor K_I reaches a critical value called the toughness of the material $K_{IC} = \sqrt{2\,E'\,\gamma_S}$, where γ_S is the

fracture surface energy of the solid material [105] and $E' = E/(1-\nu^2)$. For a penny-shaped crack, the stress intensity factor near the tip is defined as [63]:

$$K_{\mathrm{I}} = \frac{2}{\sqrt{\pi R}} \int_0^{R(t)} \frac{p(r,t)}{\sqrt{R^2 - r^2}} r \mathrm{d}r. \tag{3.14}$$

3.2.3 Boundary conditions at the fracture tip and injection point

At the tip of the crack, the width $w(R)$ goes to zero:

$$w = 0, \quad r = R(t), \tag{3.15}$$

and the flow rate also goes to zero:

$$w^3(r,t) \frac{\partial p(r,t)}{\partial r} = 0, \quad r = R(t). \tag{3.16}$$

At the point source, the local flow rate is equal to the injected flow rate

$$2\pi \lim_{r \to 0} r\, q(r,t) = Q_{in}. \tag{3.17}$$

3.3 Scaling

The equations are non-dimensionalized by identifying the characteristic scales in both phases as listed in table 3.1.

The characteristic radius and aperture of the fracture are R and W_0 respectively, with R the radius of the fracture and W_0 the maximum aperture of the fracture at $r = 0$. The position of the interface is R_I. The characteristic pressure in both the fluids is taken to

Parameter	Inner region	Outer region
Radius	$r = R_I\hat{r}$	$r = R\tilde{r}$
Width	$w = W_0\hat{w}$	$w = W_0\hat{w}$
Pressure	$p = P_0\hat{p}$	$p = P_0\hat{p}$

Table 3.1: Rescaled parameters

be P_0. We define effective material parameters μ' E', and K' as proposed by Savitski & Detournay (2002) [22]:

$$\mu'_{in} = 12\mu_{in},\ \mu'_0 = 12\mu_0,\ K' = 4\left(\frac{2}{\pi}\right)^{\frac{1}{2}} K_{IC}, \text{ and } E' = \frac{E}{1-\nu^2}. \tag{3.18}$$

To compare the viscosity of the two liquids, we introduce the parameter $M = \mu'_{in}/\mu'_0$. When the two fluids are present in the fracture, we used a weighted average to define the resulting viscosity μ_e and the corresponding effective value $\mu'_e = 12\mu_e$.

Using the characteristic parameters summarized in table 3.1 and the effective material properties, we obtain the following set of equations to describe the displacement flow and fracture propagation:

1. Lubrication theory (from equations 3.3-3.4)

$$\frac{\mu'_e\, R^2}{W_0^2\, P_0}\ \frac{\partial \hat{w}}{\partial t} = \frac{1}{\hat{r}}\ \frac{\partial}{\partial \hat{r}}\left(\hat{r}\hat{w}^3 \frac{\partial \hat{p}}{\partial \hat{r}}\right) \tag{3.19}$$

2. Linear elasticity (from equation 3.13)

$$\hat{w} = \frac{8R}{\pi E' W_0}\left[P_0 \int_0^1 \int_0^1 \frac{x\hat{p}(x\xi R, t)}{\sqrt{1-x^2}} dx d\xi\right] \tag{3.20}$$

3. Fracture propagation (from equation 3.14)

$$\frac{K'}{P_0\sqrt{R}} = \frac{2^{7/2}}{\sqrt{\pi}} \int_0^1 \frac{\tilde{p}\,\tilde{r}}{\sqrt{1-\tilde{r}^2}}\, d\tilde{r} \tag{3.21}$$

4. Global mass balance (from equations 3.11-3.12)

$$\frac{Q_{in}\, t}{2\pi\, R_I^2\, W_0} = \int_0^1 \hat{r}\hat{w}\, d\hat{r} \tag{3.22}$$

and

$$\frac{V_0}{2\pi\, R^2\, W_0} = \int_0^1 \tilde{r}\hat{w}\, d\tilde{r} - \left(\frac{R_I}{R}\right)^2 \int_0^1 \hat{r}\hat{w}\, d\hat{r}. \tag{3.23}$$

As the fluid is injected, the elastic pressure drives the propagation of the crack, which is resisted by the viscous dissipation associated with the motion of the injected and displaced fluids and the fracture toughness. We first assume that the interfacial pressure is negligible compared to the viscous and toughness-related stresses. We then assume that one of the resisting stresses controls the propagation and balances the elastic stress. Studies on single fluid injection have validated this approach, with experimental evidence of the two asymptotic regimes. If the viscous stresses in the fluids are larger than the fracture-opening stress, the fracture propagation is said to be in the viscous regime. Alternatively, the propagation is in the toughness regime. For both regimes, we can derive scaling arguments from the dimensionless groups in equations 3.19-3.23.

3.3.1 Toughness regime

For the toughness scaling, we set the non-dimensional groups in equations 3.20-3.23 equal to one. Indeed the viscous stresses are negligible and the crack opening is limited

by the toughness of the material. The scaling relations are:

$$\frac{W_0 E'}{P_0 R} = 1 \tag{3.24}$$

$$\frac{K'}{P_0\sqrt{R}} = 1 \tag{3.25}$$

$$\frac{Q_{in} t}{R_I^2 W_0} = 1 \tag{3.26}$$

$$\frac{V_0}{W_0} = R^2 - R_I^2. \tag{3.27}$$

We define the characteristic time scale $T = V_0/Q_{in}$ and the corresponding dimensionless time $\tilde{t} = t/T$. By combining those groups, we obtain the toughness-dominated scaling of the fracture properties:

$$W_0 = \left(\frac{K'}{E'}\right)^{4/5} V_0^{1/5} \left(1+\tilde{t}\right)^{1/5}, \tag{3.28}$$

$$R = \left(\frac{E' V_0}{K'}\right)^{2/5} \left(1+\tilde{t}\right)^{2/5}, \tag{3.29}$$

$$R_I = \left(\frac{E' V_0}{K'}\right)^{2/5} \tilde{t}^{1/2} \left(1+\tilde{t}\right)^{-1/10}, \tag{3.30}$$

and

$$P_0 = K' \left(\frac{K'}{E' V_0}\right)^{1/5} \left(1+\tilde{t}\right)^{-1/5}. \tag{3.31}$$

3.3.2 Viscous regime

For the viscous scaling, we set the non-dimensional groups in equations 3.2-3.3 and 3.22-3.23 equal to one. Here the propagation of the fluids follows the lubrication equation

Fracture	Viscous regime	Toughness regime
Radius	$R \approx \left(\frac{E'}{\mu'_e Q_{in}}\right)^{1/9}$	$R \approx \left(\frac{E' V_0}{K'}\right)^{2/5} \left(1+\tilde{t}\right)^{2/5}$
	$V_0^{4/9} \left(1+\tilde{t}\right)^{1/3} \left(\alpha+\tilde{t}\right)^{1/9}$	
Interface	$R_I \approx \left(\frac{E'}{\mu'_e Q_{in}}\right)^{1/9}$	$R_I \approx \left(\frac{E' V_0}{K'}\right)^{2/5} \tilde{t}^{1/2} \left(1+\tilde{t}\right)^{-1/10}$
	$V_0^{4/9} \sqrt{\tilde{t}} \left(1+\tilde{t}\right)^{-1/6} \left(\alpha+\tilde{t}\right)^{1/9}$	
Aperture	$W_0 \approx \left(\frac{\mu'_e Q_{in}}{E'}\right)^{2/9}$	$W_0 \approx \left(\frac{K'}{E'}\right)^{4/5} V_0^{1/5} \left(1+\tilde{t}\right)^{1/5}$
	$V_0^{1/9} \left(1+\tilde{t}\right)^{1/3} \left(\alpha+\tilde{t}\right)^{-2/9}$	

Table 3.2: Scaling relations for a penny-shaped fracture driven by a displacement flow. The time evolution of the geometrical properties of the fracture depends on the dominant resisting stress, which can be viscous or toughness-related.

and the viscous dissipation limits the propagation of the fracture:

$$\frac{W_0 E'}{P_0 R} = 1 \tag{3.32}$$

$$\frac{\mu'_e R^2}{W_0^2 P_0 \left(t + V_0/Q_0\right)} = 1 \tag{3.33}$$

$$\frac{Q_{in} t}{R_I^2 W_0} = 1 \tag{3.34}$$

$$\frac{V_0}{W_0} = R^2 - R_I^2 \tag{3.35}$$

We define the effective viscosity of the volume of fluid in the fracture as a weighted average. The effective viscosity depends on the viscosities of the two fluids in the fracture and their relative volumes at time $\tilde{t}$:

$$\mu'_e = \frac{\mu'_0 + \mu'_{in} \tilde{t}}{1+\tilde{t}} \tag{3.36}$$

We obtain the viscous-dominated scaling of the variables:

$$W_0 = \left(\frac{\mu'_e Q_{in}}{E'}\right)^{2/9} V_0^{1/9} \left(1+\tilde{t}\right)^{1/3} \left(\alpha+\tilde{t}\right)^{-2/9}, \tag{3.37}$$

$$R = \left(\frac{E'}{\mu'_e Q_{in}}\right)^{1/9} V_0^{4/9} \left(1+\tilde{t}\right)^{1/3} \left(\alpha+\tilde{t}\right)^{1/9}, \tag{3.38}$$

$$R_I = \left(\frac{E'}{\mu'_e Q_{in}}\right)^{1/9} V_0^{4/9} \sqrt{\tilde{t}} \left(1+\tilde{t}\right)^{-1/6} \left(\alpha+\tilde{t}\right)^{1/9}, \tag{3.39}$$

$$P_0 = \left(\frac{\mu'_e Q_{in} E'^2}{V_0}\right)^{1/3} \left(\alpha+\tilde{t}\right)^{-1/3} \tag{3.40}$$

with $\alpha = Q_{in}/Q_0$. The results are summarized in table 3.2.

3.3.3 Discussion

We consider the single-fluid limit of the two asymptotic regimes. Indeed for a pre-fracture volume equal to zero, $V_0 = 0$, or for large values of the injection time $t >> 1$, the expressions derived above should be equal to those previously obtained for single fluid injection. In the toughness regime, we recover the single-fluid scaling relations [22, 29, 32]:

$$W_0 = \left(\frac{K'}{E'}\right)^{4/5} (Q_{in}\, t)^{1/5}, \tag{3.41}$$

$$R = \left(\frac{E'}{K'}\right)^{2/5} (Q_{in}\, t)^{2/5}, \tag{3.42}$$

and

$$P_0 = K' \left(\frac{K'}{E'\, Q_{in}\, t}\right)^{1/5}. \tag{3.43}$$

In the viscous regime, we also recover the scaling relations for a single fluid injection:

$$W_0 = \left(\frac{\mu'_{in}}{E'}\right)^{2/9} Q_{in}^{1/3}\, t^{1/9}, \tag{3.44}$$

$$R = \left(\frac{E'}{\mu'_{in}}\right)^{1/9} Q_{in}^{1/3}\, t^{4/9}, \tag{3.45}$$

and

$$P_0 = \left(\frac{\mu'_{in} E'^2}{t}\right)^{1/3}. \tag{3.46}$$

The fluid and matrix properties determine whether the fracture propagation is in the viscous or toughness regime. Past studies in single fluid injection have defined criteria to predict the propagation regime. The regime is defined by the largest of the two stresses that oppose the elastic stress: the toughness-related stress $\Delta P_m \approx \frac{K'}{\sqrt{R}}$ and the viscous stress $\Delta P_v = \frac{\mu' Q}{W_0^3}$. In the viscous regime, we can use the scaling relations for R and W_0 to estimate the ratio:

$$\left(\frac{\Delta P_m}{\Delta P_v}\right)_v = \left(\frac{K'^9\, t}{E'^{13/2}\, Q^{3/2}\, \mu'^{5/2}}\right)^{1/9} = \left(\frac{t}{t_{mk}}\right)^{1/9} = \kappa. \tag{3.47}$$

where

$$t_{mk} = \left(\frac{E'^{13/2}\, Q^{3/2}\, \mu'^{5/2}}{K'^9}\right) \tag{3.48}$$

is the characteristic timescale of the system and κ is the dimensionless toughness. Similarly, we can define the relative magnitude of both stresses in the toughness regime using the corresponding scaling relations:

$$\left(\frac{\Delta P_m}{\Delta P_v}\right)_m = \left(\frac{t}{t_{mk}}\right)^{2/5} = \kappa^{18/5}. \tag{3.49}$$

The viscous-dominated propagation is therefore associated with small values of κ, i.e.

κ or $t/t_{mk} \lesssim 1$ and the toughness-dominated dynamics for κ or $t/t_{mk} >> 1$.

Similarly, we can define the propagation regime of the fracture formed by a displacement flow. The toughness related stress remains $\Delta P_m \approx K'/\sqrt{R}$, while the viscous stress becomes $\Delta P_v = \mu'_e Q_{in} R^2 \left(R_I^2 W_0^3 + \alpha V_0 W_0^2\right)^{-1}$ as defined in equations 3.25 and 3.33.

In the viscous regime, we substitute R, R_I, and W_0 by the scaling relations defined in table 3:

$$\left(\frac{\Delta P_m}{\Delta P_v}\right)_v = \frac{K' V_0^{1/9} (\alpha + \tilde{t})^{5/18}}{E'^{13/18} \mu_e'^{5/18} Q_{in}^{5/18} (1+\tilde{t})^{1/6}} \tag{3.50}$$

Similarly, in the toughness regime, we estimate the ratio to be

$$\left(\frac{\Delta P_m}{\Delta P_v}\right)_m = \left(\frac{\Delta P_m}{\Delta P_v}\right)_v^{18/5} \tag{3.51}$$

The ratio of the viscous and toughness-related stresses is a function of time, that increases as $\tilde{t}^{1/9}$ for large values of $\tilde{t}$. In consequence, the propagation becomes toughness-controlled for long time or large-volume injections. This result is consistent with what is known for a single fluid injection. Contrary to the single fluid criterion however, there is no explicit solution for the threshold injection time in the case of displacement flow. We can determine the propagation regime at time $\tilde{t}$ by comparing the pressure ratio with 1.

3.4 Experiments

Laboratory-scale experiments commonly use hydrogels as rock analogues to study hydraulic fracturing in brittle elastic materials [31, 73]. In particular, gelatin is a clear gel whose elasticity can easily be tuned by varying the volume fraction of gelatin powder in water [43, 39, 28]. Because gelatin expands as it sets in the container, the material is spontaneously compressed, which furthers the analogy with soft rocks for fracture studies.

Exp.		Gel	Pre-fracture - oil-filled			Injection	
		E (kPa)	μ_0 (Pa.s)	Q_0 (ml.min^{-1})	V_0 (ml)	Fluid	μ_{in} (Pa.s)	Q_{in} (ml.min^{-1})
1	○	30	0.01	0.3	5.6	Water	0.001	0.5
2	▽	30	0.01	0.3	6.2	Water	0.001	1
3	◀	30	0.01	0.15	5.1	Water	0.001	0.15
4	△	30	0.01	0.15	6.3	Water	0.001	1
5	▶	15	0.02	0.1	7.1	Water	0.001	0.25
6	◇	30	0.01	0.3	3.9	Water	0.001	1.8
7	×	30	0.01	0.15	4	Water	0.001	1.8
8	■	30	0.01	0.5	6.2	Water	0.001	3.6
9	+	30	0.01	0.15	2.9	Water	0.001	0.54
10	△	15	0.01	0.25	6.1	Water	0.001	0.5
11	✳	88	10.26	10	10	Glycerol	1.2	10
12	□	88	10.26	10	15	Glycerol/water	0.3	10
13	●	88	10.26	10	15	Glycerol	1.2	10
14	◁	88	10.26	10	5	Glycerol	1.2	10
15	★	88	10.26	10	6.5	Syrup	8.6	10
16	▼	88	10.26	10	8	Syrup	8.6	10

Table 3.3: List of experiments: symbols and parameters.

3.4.1 Material preparation and characterisation

The properties of the gelatin and the injected fluids control the fracture dynamics and are, therefore, systematically characterized. The gelatin is prepared by heating ultra-pure water to 60°C. While stirring the heated water, we slowly add gelatin powder (Gelatin type A; Sigma-Aldrich, USA) at a mass fraction of 10 to 30 % to vary Young's modulus of the resulting gel. The gelatin then cools down to room temperature and sets over 24 hours prior to testing or fracturing. The Young's modulus of gelatin is measured with a custom-built displacement-controlled load frame. The sample is compressed by a ballscrew stage whose speed is set by a stepper motor Parker Compumotor OS22B controlled by a controller Parker Compumotor ZL6104. A load cell, Eaton 3108-10 (10 lb. capacity) measures the force generated by the compressed sample. We record force-displacement values for cylindrical samples of gelatin of diameter and height equal to 1 in and compute the stress-strain curves of the material. At small strain, all gelatin samples exhibit a linear elastic response to the compression. As listed in table 3.3, Young's modulus ranges between 15 to 116 kPa with a measurement error of ± 10 %. The fracture energy and Poisson's ratio of the gelatin are assumed constant in our experiments with $\gamma_S \approx 1$ J.m^{-2} and $\nu \approx 0.5$ [38].

To study displacement flows in fluid-filled fractures, we use immiscible Newtonian liquids. Silicone oils of different viscosity are used to form the pre-fracture. An aqueous solution composed of water, glycerol or corn syrup is then injected. The silicone oil is dispalced outward, further expanding the fracture in the gelatin. We measure the viscosity of the fluids and the surface tension at the oil/water and oil/syrup interfaces. Viscosity measurements are conducted using an MCR 92 Anton Parr rheometer with a parallel plate measuring system at 20°C. The values obtained have a measurement error of ± 1 % and are listed in table 3.3. Surface tension measurements are conducted using

the pendant drop method with an Attension Theta Flex tensiometer: the surface tension between silicone oil and water is $\gamma_{o/w} \approx 35 \pm 2$ mN.m^{-1} and between silicone oil and syrup is $\gamma_{o/s} \approx 50 \pm 2$ mN.m^{-1}. The fluid properties are selected to study the propagation of the pre-fracture and fracture in a single regime of during the experiment. For example, the values of κ at the end of the injection forming the pre-fracture, for experiments 1 through 10 varies between $35 \leq \kappa \leq 55$. Those experiments are expected to be in the toughness dominated regime. Similarly, for experiments 11 through 16, $1.7 \leq \kappa \leq 1.9$ at the end of the formation of the pre-fracture: these experiments target the viscous-dominated propagation. These values are consistent with previous work on the formation of fluid-driven fractures in a bloc of gelatin. During the formation of the fracture through the displacement flow, we estimate the pressure ratio in the viscous regime $\left(\frac{\Delta P_m}{\Delta P_v}\right)_v$ at the end of the injection. The ratio varies between 24 and 58 for experiments 1 through 10, which are therefore expected to be in the toughness regime. The ratio varies between 1.9 and 2.5 for experiments 11 through 16, which are therefore expected to be in the viscous regime.

3.4.2 Set-up

The injection experiments are conducted in a large block of gelatin to avoid boundary effects on the propagation of the fracture. The gelatin is set in a cubic clear container (15 cm $\times$ 15 cm $\times$ 15 cm) around a blunt needle as represented in figure 3.2. We use a thin needle (inner diameter, $ID = 1$ mm) for low-viscosity injections and a wide needle for high-viscosity injection ($ID = 2.15$ mm). In our system, the confining stress is minimum in the vertical direction, the fracture, therefore, propagates horizontally, in the direction that opposes the least resistance. To avoid small tilts of the fracture that would compromise the quality of the recording, a plastic washer is placed at the tip of

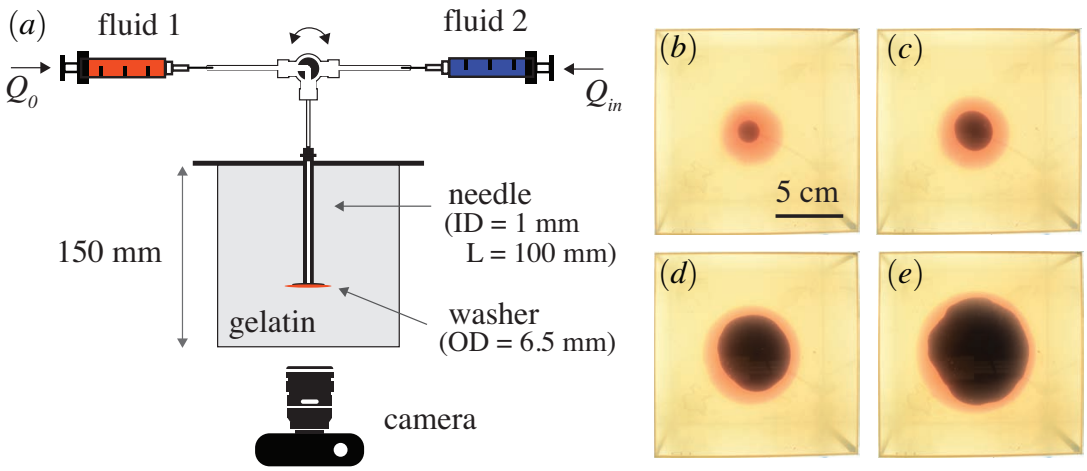

Figure 3.2: (a) Schematic of the experimental set-up. $(b-e)$ Time evolution of the fracture formed in experiment 1. The water dyed with blue food colour is injected at $Q_{in} = 0.5$ ml.min^{-1} in a pre-fracture formed with silicone oil dyed with red food colour. The recording starts when the water injection begins and the experimental images are taken at (b) $t = 50$ s, (c) $t = 300$ s, (d) $t = 1300$ s and at (e) $t = 2800$ s. The supplementary movies 1 and 2 show the complete time evolution of the pre-fracture and fracture, respectively. The movies are available at [to be added].

the needle to initiate the fracture in the horizontal plane. Two fluids are successively pumped into the gelatin. For each fluid, we use a kdScientific® Legato 200 syringe pump to set the injection flow rate at a value between 0.1 and 20 ml.min^{-1} with an accuracy of $\pm 0.35\,\%$. Both fluid-filled syringes are connected to the same injection needle using a switch valve. First, a silicone oil of viscosity μ_0 is injected at a constant volumetric flow rate Q_0 in the gelatin matrix to form the pre-fracture. The injection stops when a volume V_0 of silicone oil has been dispensed. The valve is then switched to inject the aqueous phase of viscosity μ_{in} into the pre-fracture at a flow rate of Q_{in}. The injection stops when the fracture tip is within 2 cm of the container walls to avoid confinement effects [27]. The two fluids are dyed to allow visualizing the propagation of the fracture and interface between the two liquids in the clear gelatin: we use a blue water-based food dye for the aqueous phase and a red oil-based food dye for the oil phase as shown in figure 3.2. The propagation is recorded using a Nikon D5300 camera with a Phlox® LED panel ensuring

uniform backlighting. The images are processed using a custom-made MATLAB code to determine the radius of the fracture R and the position of the interface between the two liquids R_I.

3.4.3 Measurement of the fracture width

To measure the thickness of the fracture during the propagation, we use a light absorption method [59, 26]. This method consists in selecting a soluble dye and the corresponding optical filter. The filter should transmit light to the camera at the wavelength at which the dye absorbance A is maximum A_λ. The absorbance follows Beer's law:

$$A_\lambda = -\log_{10}\left(\frac{I_\lambda}{I_{\lambda,0}}\right) = \epsilon_\lambda c\, h \tag{3.52}$$

where $I_{\lambda,0}$ is the background intensity and I_λ is the intensity when light passes through a liquid layer of thickness h, with a dye concentration c. The parameter ϵ_λ characterizes the absorbance of the dye at the selected wavelength and is obtained through calibration. To measure the thickness of both liquids in the fracture, we use two dyes, one water-soluble and one oil-soluble and record the absorbance using a single optical filter. To get accurate measurements, we select dyes with a large absorbance at the same wavelength. In all experiments, the water-soluble dye is nigrosin (Sigma-Aldrich) at 0.05 g.L^{-1}. Nigrosin is a black dye that absorbs at all wavelengths. We use different dyes depending on the viscosity of the silicone oil, because of their solubility limit. We dilute sudan red (Sigma-Aldrich) in the low-viscosity silicone oils, i.e. 10 and 20 mPa.s silicone oils, at 0.05 g.L^{-1}, and nile red (Sigma-Aldrich) in high-viscosity silicone oils, i.e. 10,300 and 30,000 mPa.s silicone oils, at 0.2 g.L^{-1}. For experiments with sudan red in the oil phase and nigrosin in the aqueous phase, we use a 520 nm optical filter. When nile red dyes the oil phase and nigrosin the aqueous phase, we use a 632 nm optical filter.

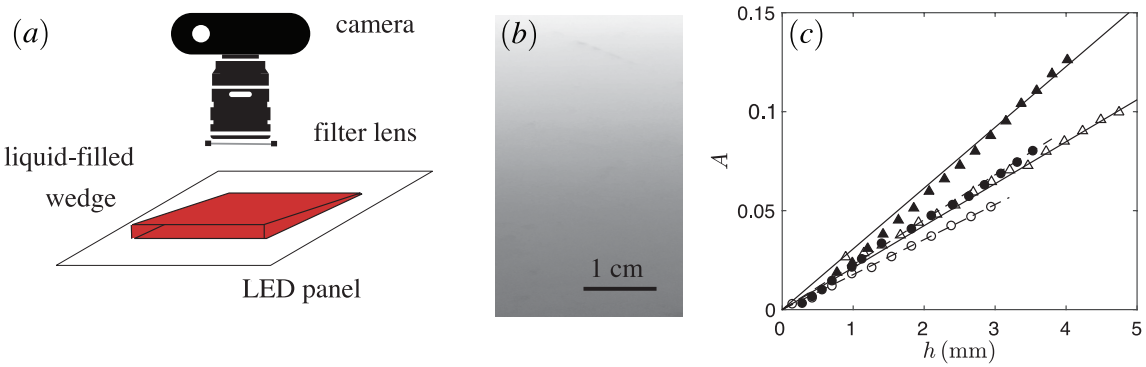

Figure 3.3: Calibration. (a) Schematic of the calibration experiment for low-viscosity fluids. (b) The intensity gradient was recorded for a wedge filled with water dyed with nigrosin at 0.05 g.L^{-1} through the 520 nm filter. (c) Absorbance measured for nigrosin-dyed water at $\lambda = 520$ nm (▲), nigrosin-dyed syrup at $\lambda = 632$ nm (●), sudan red-dyed 10 mPa.s-silicone oil at $\lambda = 520$ nm (△), and nile red-dyed 10 Pa.s-silicone oil at $\lambda = 632$ nm (○). The solid lines are the best linear fit for each calibration data set.

To measure the thickness of the fracture, we first conduct calibration experiments for each dye solution. For the low-viscosity solutions (water, 10 and 20 mPa.s silicone oils), we use a glass wedge with an aperture that increases linearly from 0 to 10 mm as shown in figure 3.3. The wedge is placed on the LED panel and the light intensity is obtained by taking a picture of the wedge with the optical filter mounted on the camera. The background intensity corresponds to an empty wedge. The light intensity of a liquid-filled wedge decreases as the thickness of the aperture increases (see figure 3.3(b)). The grey values are used to determine the absorbance as a function of the liquid thickness, as plotted in figure 3.3(c). Using a linear fit, we get $1/\epsilon_\lambda c = 47.2$ mm for sudan red in oil and $1/\epsilon_\lambda c = 32.6$ mm for nigrosin in water for $\lambda = 520$ nm. For the high-viscosity samples, we use rectangular cells that are easier to fill. The cell thickness or height ranges from 0.3 to 3 mm. For each cell, we measure the background intensity of the empty cell and the intensity of the cell filled with the viscous fluid, i.e. syrup, 10,000 mPa.s or 30,000 mPa.s silicone oil. We obtain the absorbance for a set of thickness values as shown in figure 3.3. Using a linear fit, we get $1/\epsilon_\lambda c = 56.5$ mm for nile red in oil and $1/\epsilon_\lambda c = 44$

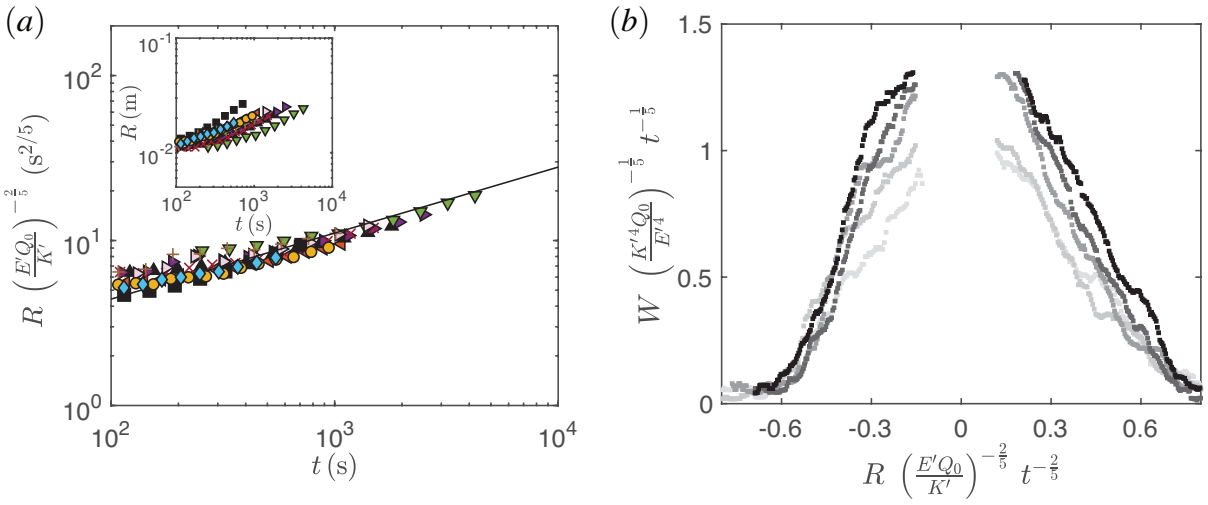

Figure 3.4: Dynamics of the pre-fracture for low-viscosity oils. (a) Dependence of rescaled fracture radius on time for experiments 1 to 10 (see table 3.3 for corresponding injection parameters). The radius is rescaled using equation 3.42 in the toughness scaling for single fluid injection. The origin for time is set when the oil enters the gelatin. The black curve represents the best linear fit with a slope of 2/5. Inset: dependence of the radius R on time t. (b) Rescaled fracture thickness profiles based on equations 3.41 and 3.42 at $t = [245, 370, 495, 620, 745]$ s with time increasing from clear to dark gray. Experimental parameters: $E = 30$ kPa, $\mu_0 = 10$ mPa.s, $Q_0 = 0.3$ ml.min^{-1}.

mm for nigrosin in water for $\lambda = 632$ nm. The fitting parameters obtained are then used to obtain the width of the fracture using Beer's law:

$$h = \frac{A_\lambda}{\epsilon_\lambda c} = \frac{-\log_{10}\left(\frac{I_\lambda}{I_{\lambda,0}}\right)}{\epsilon_\lambda c} \tag{3.53}$$

The concentrations of dyes chosen for this study, some of which are limited by solubility, are all sufficiently low for the absorbance to vary linearly with the sample thickness or fracture aperture. The accuracy of the measurements is limited by the noise due to low absorbance values.

3.5 Results

In this section, we present the results of the experiments listed in table 3.3. We measure the radius and aperture of the pre-fracture and fracture and compare the data with the scalings obtained for the viscous and toughness regimes.

The fracture propagates radially upon injection of the fluid. Viscous fingering is not observed in our experiments, as illustrated in figure 2.2(b)-(e). The viscosity ratio $M = \frac{\mu_{in}}{\mu_{out}}$ varies between 0.05 and 1, and the thickness of the crack is of the order of a few millimetres, so the characteristic wavelength of the instability is larger than the perimeter of the injected fluid region. We estimate the experimental error by conducting an error analysis based on the scaling laws and the measurement error of the various parameters: 10% for the Young's modulus E, 10% for the fracture toughness K, 0.35% for the flow rate Q, 1% for the viscosity μ and 5% for the volume V_0. In the toughness regime, the experimental error on the radius is estimated to be $\sim 10\%$. In the viscous regime, the error is $\sim 4\%$.

3.5.1 Single Fluid Injection

We prepare the pre-fracture by injecting silicone oil into the gelatin cube. After an initial pressure build-up, the oil propagates rapidly over the washer at the tip of the needle. A radial fracture then forms around the washer, propagating more slowly with the oil filling the gap between the two gelatin surfaces. The homogeneous properties of the gelatin result in axisymmetric fractures for both low and high-viscosity fluids. The radius of the fracture is measured during the injection and compared with the scaling for the toughness and viscous-dominated regimes for a single fluid (equations 3.42 and 3.45, respectively). Experiments 1-10 are in the toughness regime as low-viscosity silicone oil is injected in soft gelatin (see table 3.3). Experiments 11-16 are in the viscous regime

as high-viscosity silicone oil is injected in harder gelatin. In figure 3.4(a), we plot the results of the experiments in the toughness regime. The radius increases with time and the rescaled radius follows a $t^{2/5}$ power law which is consistent with equation 3.42. In the log-log scale, the best fit line with a slope 2/5 has a prefactor $k = 0.7$ which is in agreement with the theoretical prefactor of 0.85 derived by Savitski & Detournay (2002) [22]. These results are also consistent with previous experimental data in this regime [29, 32]. In figure 3.5(a), we report the data obtained in the viscous regime. The experimental conditions for those experiments are similar and the results demonstrate the high reproducibility of the experiments [30]. The radius increases as a power law of time. Upon rescaling the radius with the viscous scaling parameter, the data collapse on a line of slope 4/9 with a prefactor of $k = 0.36$. This result differs from the theoretical prefactor of 0.7, yet it is comparable to the values obtained in previous experimental studies in the viscous regime [28, 32]. Due to the initiation transient and finite size of the container, the power-law fits span about a decade of the log-log plots, which is common for laboratory-scale experiments.

For each regime, we measure the fracture aperture using a dye whose absorbance varies linearly with the aperture. The results presented show the evolution of the fracture cross-section over time for one experiment in the toughness regime (see figure 3.4(b)) and one in the viscous regime (see figure 3.5(b)). For both experiments, the curves show the aperture as a function of the radial position at different injection times. Because the needle disturbs the absorbance measurement near the center of the fracture, the aperture is not measured near the needle, i.e. for small values of the radius. Upon integration of the thickness curve recorded when the injection is complete, we obtain the value of $V_0 \pm 0.5$ ml. The aperture-radius curves are rescaled using the scaling for the aperture and radius. In both regimes, the curves collapse on a self-similar profile. The two data sets presented here are representative of the prefacture obtained for all the experiments

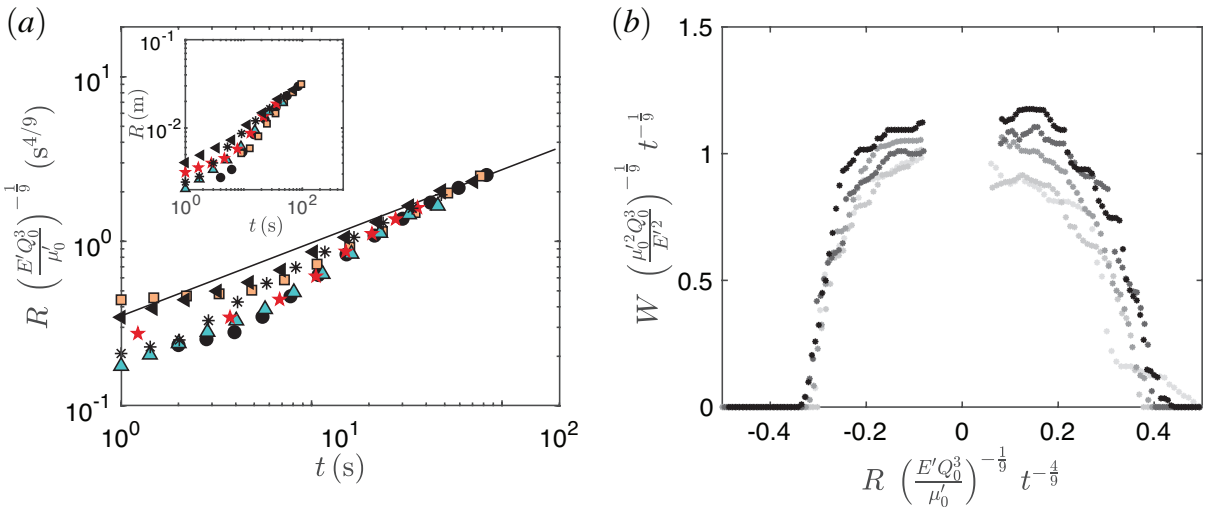

Figure 3.5: Dynamics of the pre-fracture for high-viscosity oils. (a) Dependence of rescaled fracture radius on time for experiments 11 to 16 (see table 3.3 for corresponding injection parameters). The radius is rescaled using equation 3.45 in the viscous scaling for single fluid injection. The black curve represents the best linear fit with a slope of 4/9. Inset: dependence of the radius R on time t. (b) Rescaled fracture thickness profiles based on equations 3.44 and 3.45 at $t = [9, 11.5, 14, 16.5, 19]$ s with time increasing from clear to dark gray. Experimental parameters: $E = 88$ kPa, $\mu_0 = 10$ Pa.s, $Q_0 = 10$ ml.min^{-1}.

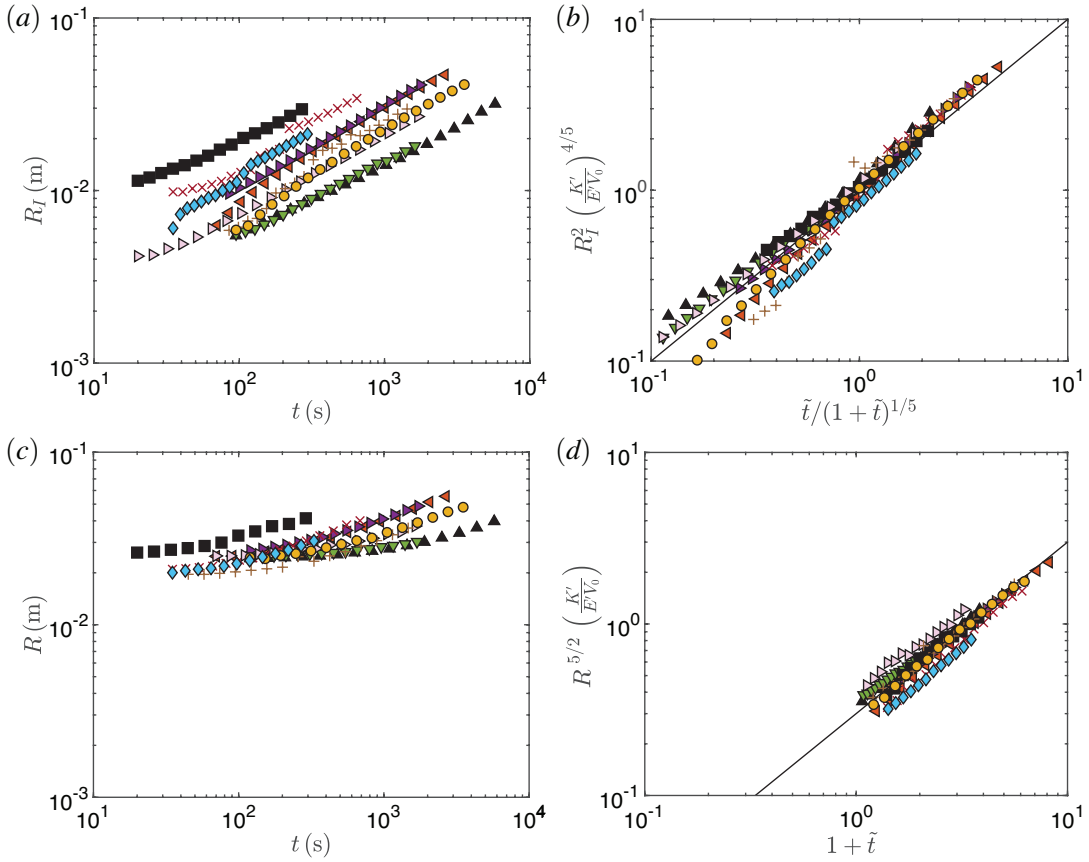

Figure 3.6: Dynamics of the fracture for low-viscosity aqueous phase. (a) Dependence of the position of the interface on time for experiments 1 to 10 (see table 3.3 for corresponding injection parameters). (b) Rescaled interface position as a function of rescaled time, based on the toughness scaling laws in table 3.2. (c) Dependence of the fracture radius on time. (d) Rescaled radius as a function of rescaled time, based on the toughness scaling laws in table 3.2. The black curves represent the best linear fit with a slope of 1.

conducted in this study and are similar to results previously reported [29, 32].

3.5.2 Displacement flow

Once the pre-fracture is formed, the valve is immediately switched to the second immiscible to avoid further propagation of the pre-fracture [24]. The material properties of the gelatin contribute to the definition of the propagation regime. Low stiffness gelatin allows the observation of the toughness regime, while the toughness regime is most

commonly reached in stiffer hydrogel. Thus, we characterize the displacement flow and fracture propagation in the toughness regime with the experimental systems 1 through 10 (see table 3.3), in which the pre-fracture is also formed in the toughness regime. The injected fluid is water. Similarly, we investigate the viscous regime in experiments 11 through 16. The displacing fluid is a syrup whose high viscosity is of the same magnitude as the silicone oil in the pre-fractures. During the displacement flow, the fracture continues its radial expansion but with a different dynamic from the one observed during the formation of the pre-fracture. To study the radial expansion of the fracture during the injection, we track the position of the interface between the two fluids R_I and the radius of the fracture R over time. In figure 3.6, we plot the results of the experiments in the toughness regime. The radial position of the interface increases with time, similarly to what was observed for a single fluid injection. The annular region of displaced fluid between R_I and R moves outward and its thickness $R - R_I$ decreases over time. Using the equations in table 2, we plot the rescaled radii with respect to the relevant dimensionless time on the log-log scale. The rescaled radial positions of the interface collapses on a line of slope 1 and prefactor 1. The rescaled radii of the fracture collapses on a line of slope 1 with a prefactor of 0.3. We note that for large values of time $\tilde{t} >> 1$, the fracture dynamics for the displacement flow is expected to become similar to the fracture dynamics for a single fluid. Indeed, if we plot the dimensionless radius as $R^{5/2}\frac{K'}{E'V_0}$, the prefactor of 0.3 for the displacement flow is comparable with the prefactor for a single fluid $0.7^{5/2} \approx 0.4$.

In figure 3.7, we plot the results of the displacement flow experiments in the viscous regime. The results can be rescaled using equations in the corresponding column of table 2. We plot the rescaled radii with respect to the relevant functions of the dimensionless time on the log-log scale. The rescaled radial positions of the interface collapse on a line of slope 1 and prefactor 0.37. The rescaled radii of the fracture collapses on a line

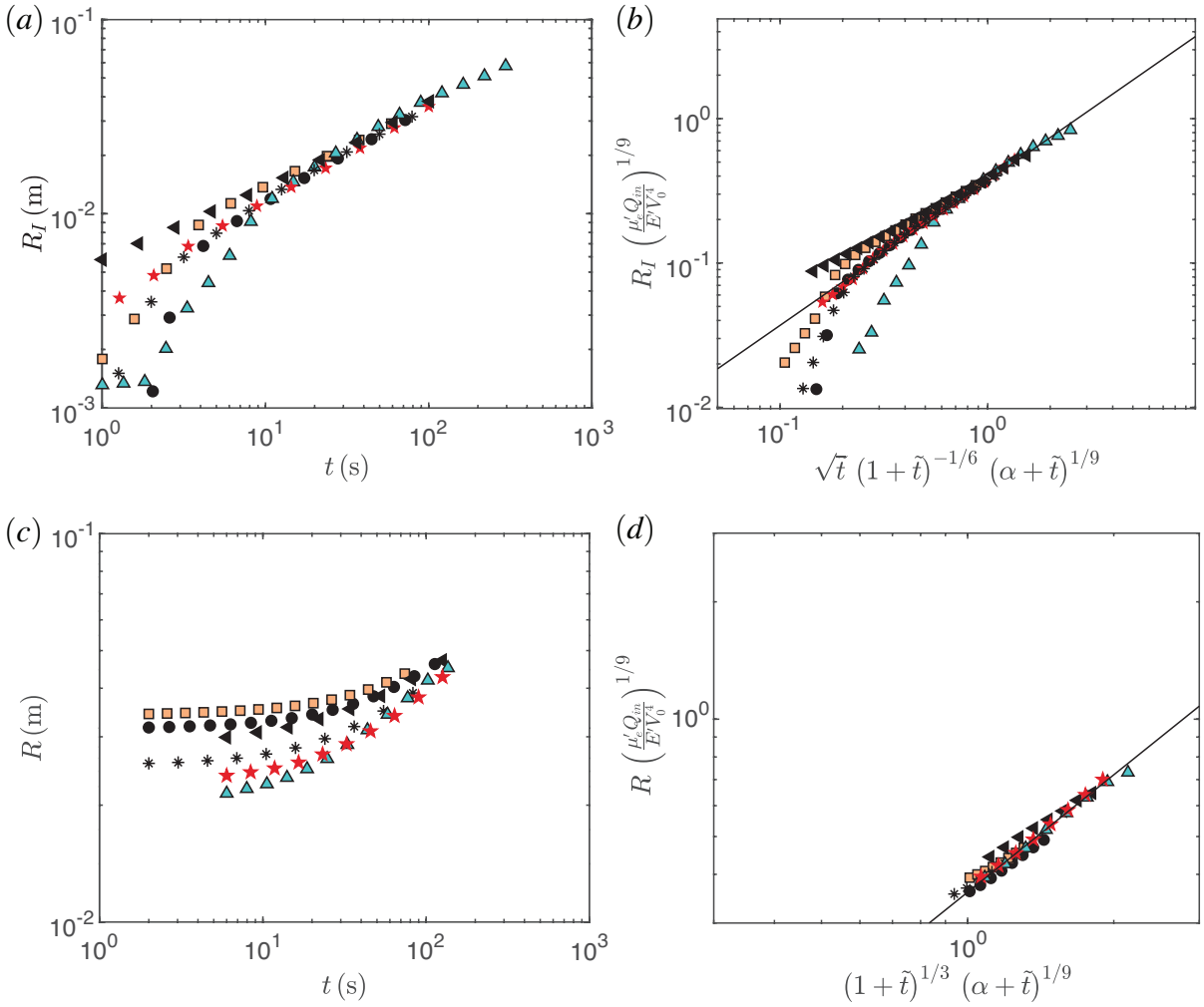

Figure 3.7: Dynamics of the fracture for high-viscosity aqueous phase. (a) Dependence of the position of the interface on time for experiments 11 to 16 (see table 3.3 for corresponding injection parameters). (b) Rescaled interface position as a function of rescaled time, based on the viscous scaling laws in table 3.2. (c) Dependence of the fracture radius on time. (d) Rescaled radius as a function of the rescaled time, based on the viscous scaling laws in table 3.2. The black curves represent the best linear fit with a slope of 1.

of slope 1 with a prefactor of 0.36. We note that for large values of time $\tilde{t} >> 1$, the fracture dynamics for the displacement flow is expected to become similar to the fracture dynamics for a single fluid. Since at large values of $\tilde{t}$, $\left(1+\tilde{t}\right)^{1/3}\left(\alpha+\tilde{t}\right)^{1/9} \approx \tilde{t}^{4/9}$, the identical prefactor for the scaling of the radius for the pre-fracture and the fracture indicates that indeed the single fluid behavior is recover for large injection times. We also note that for large values of the fracture radius, the experimental data fall below the trend line. This is due to the slow down of the growth due to the confinement of the gelatin bloc. Experimentally, this is associated with the tilting of the fracture and the formation of finger-like structures.

For the displacement flows, we measure the fracture aperture in the two fluids simultaneously, relying on two different dyes (see figures 3.8 and 3.9). Since the two dyes absorb the light differently, the absorbance profile presents a discontinuity across the interface. The absorbance values are converted to thickness measurement using Beer's law and the calibration parameters. The experimental results plotted in figures 3.8(a) and 3.9(a) show that the aperture is a continuous function of the radial position. The aperture-radius curves are rescaled using the scalings for both the aperture and radius. In the toughness regime, both the rescaled aperture and radius collapse resulting in overlapping profiles, see figure 3.8(b). In the viscous regime, the rescaled profiles collapse on a single curve, see figure 3.9(b). The two data sets presented here are representative of all the experiments. In summary, the experimental observations establish the existence of two regimes and validate the respective scaling relations.

3.6 Conclusion

In this study, we model the properties of fractures driven by displacement flows by revisiting the theoretical framework established for single fluid injections. We derive

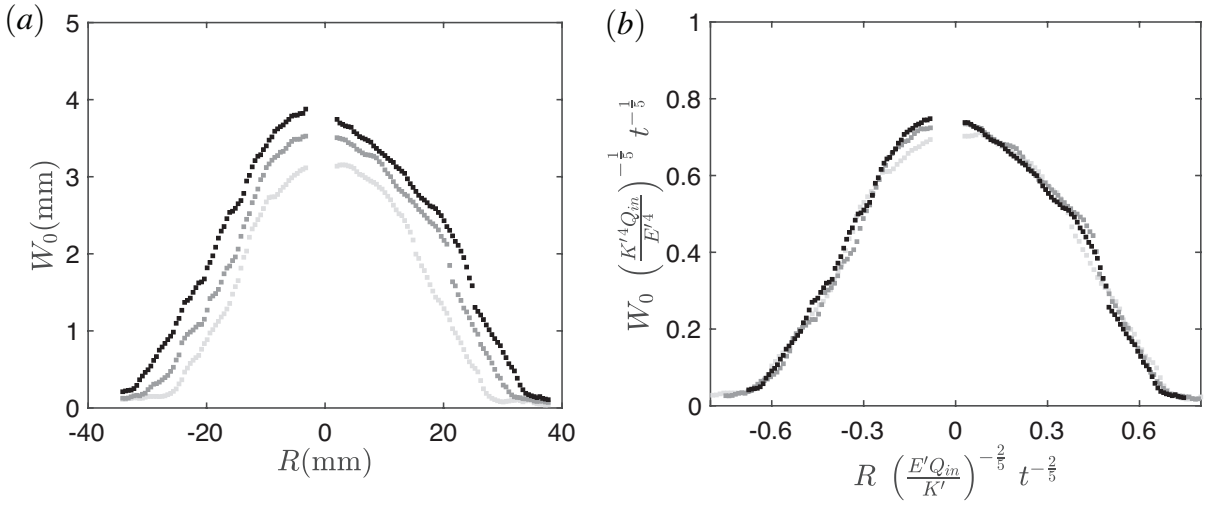

Figure 3.8: Fracture profile for low-viscosity aqueous phase. (a) Fracture profiles at $t = [150, 250, 350]$ s with time increasing from clear to dark gray. (b) Rescaled fracture profiles using the toughness scaling laws in table 3.2. Experimental parameters: $E = 30$ kPa, $\mu_0 = 10$ mPa.s, $Q_0 = 0.3$ ml.min^{-1}, $V_0 = 2.5$ ml, $\mu_{in} = 1$ mPa.s, $Q_{in} = 1.8$ ml.min^{-1}.

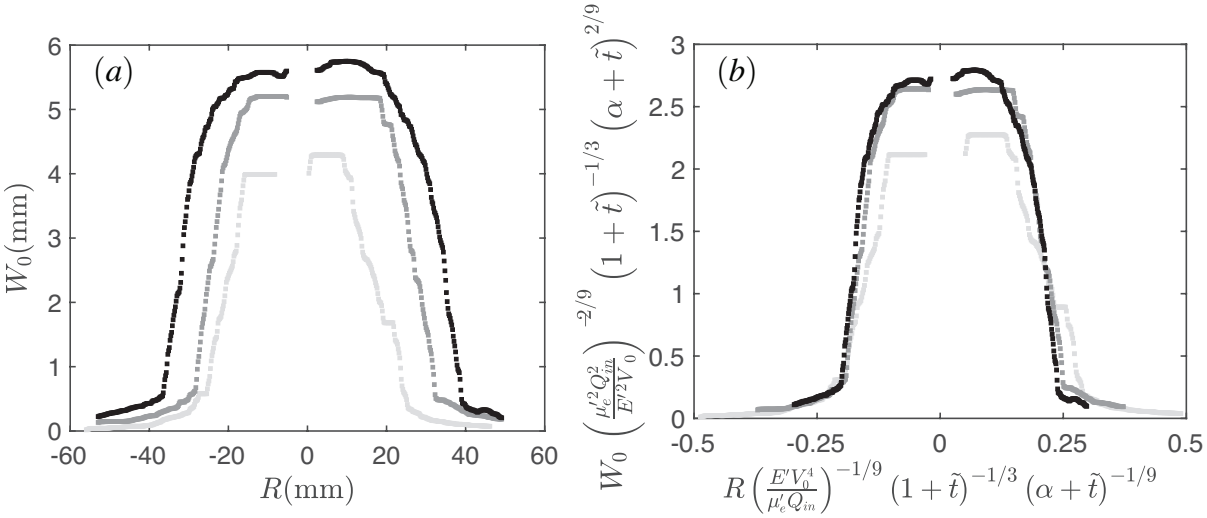

Figure 3.9: Fracture profile for high-viscosity aqueous phase. (a) Fracture profiles at $t = [5, 10, 40]$ s with time increasing from clear to dark gray. (b) Rescaled fracture profiles using the viscous scaling laws in table 3.2. Experimental parameters: $E = 88$ kPa, $\mu_0 = 10$ Pa.s, $Q_0 = 10$ ml.min^{-1}, $V_0 = 8$ ml, $\mu_{in} = 8.6$ Pa.s, $Q_{in} = 10$ ml.min^{-1}.

scaling relationships for the position of the interface between the two fluids, the radius and aperture of the fracture in a brittle elastic matrix in the viscous-dominated and toughness-dominated regimes. We define a dimensionless time, which is equal to the ratio of the volume of displacing fluid injected over the volume of the pre-fracture. In the toughness regime, the propagation dynamics is independent of the fluid properties. As a result, the fracture dynamics for the displacement flow are the same as the dynamics for a single fluid, with the addition initial finite volume V_0. In the viscous regime, however, the two fluids that fill the fracture contribute to the viscous dissipation. Over time, the relative volume of the two fluids changes. To describe the viscous dissipation in the fracture, we therefore define an average viscosity which accounts for the relative volume of displaced and displacing fluid. The scalings are compared to experimental results obtained by successively injecting an oil phase and an aqueous phase in a gelatin block. The experiments confirm the existence of two regimes of fracture propagation and are in good agreement with the derived relationships.

This study focuses on displacement flows of immiscible fluids with comparable viscosities. Other types of displacement flows are common in fracture. For example, industrial applications involve the sequential injection of miscible aqueous fluids, some of which can be complex fluids such as suspensions of particles or polymer solutions. Recent and future efforts to characterize and model multiphase flows in fractures should ultimately support efficient hydraulic fracturing operations.

Data availability statement

The data associated with this paper can be downloaded from the repository `https://doi.org/10.25349/D9W32D`.

Acknowledgements

We would like to thank Z. Zheng for helpful discussions. The work was supported in part by the ACS PRF (grant no. 60464-ND9).

Chapter 4

Dynamics of fluid-driven fractures in layered materials

4.1 Introduction

Fractures in rock formations are essential to underground energy extraction and storage [106, 107, 108, 109], carbon sequestration [110, 111, 112] and waste containment [113]. Safe operations require understanding how fluid transport and reservoir properties control fracture dynamics [14, 114]. Hydraulic fractures are driven by the injection of a pressurized fluid in a rock formation of low permeability. This industrial practice emerged in the 1940s when the first gas drilling company took up the challenge to commercially extract the oil and gas trapped in the tiny pores of shale rock [115]. Hydraulic fracturing has since become a common practice [47], with new applications including carbon sequestration [116].

Because of the considerable risks and expenses associated with CO_2 transportation, storage in a reservoir near the emission source is preferred [2, 3]. Yet, local reservoirs may not possess the most favorable characteristics for storing large fluid volumes, requiring

hydraulic fracturing to improve permeability [4].

The injection of large amounts of fluid into geological formations poses environmental and public health risks associated with water footprint, seismic activity, and leakage of the fracture content [5, 6, 7]. Carbon sequestration commonly relies on cap rocks to prevent leaks [8]. Yet injection can induce fracture propagation within the reservoir and cap rock [9, 10, 11, 12], compromising long-term storage. Leakage can also contaminate groundwater reservoirs, directly impacting local ecosystems and populations [13].

Geomechanics govern fracture propagation and transport of the injected fluid. More precisely, the composition and structure of geological formations control fracture dynamics. Rocks exhibit natural discontinuities (such as stratification), fissures, faults, and cracks. The mapping of underground mechanics and the development of predictive models that account for rock heterogeneity are essential for safe fluid injection and storage. To that end, recent experimental studies have looked at increasingly complex systems to gain better insights into the propagation dynamics of hydraulic fractures [33, 34, 35, 41, 36]. Previous work on heterogeneous media has shown that stress and/or stiffness contrast affect fracture propagation, leading to changes in propagation planes, non-axisymmetric fractures, and arrested growth [117, 118, 119, 120, 121].

This study focuses on the interaction of a penny-shaped fracture with a material discontinuity in a brittle elastic medium with no stress contrast. The fluid is injected in a hydrogel block composed of two layers that exhibit different stiffness. Since the material toughness governs the fracture propagation, the stiffness contrast determines the fate of the fracture as it reaches the interface between the two layers. We are particularly interested in the fracture dynamics when it propagates from a stiff into a soft layer exhibiting a growth spur, which, to the best of our knowledge, has never been reported.

Our experiments characterize hydraulic fractures formed with various injection parameters, fluid, and material properties. The theoretical model of the propagation dy-

namics relies on scaling arguments to reproduce experimental results and yields good agreement. While the experiments and model simplify the situations encountered during industrial processes, they provide valuable insights into the underlying physics.

4.2 Experimental methods

We conduct laboratory-scale experiments that rely on soft hydrogel to model the dynamics of hydraulic fractures propagating through stratified rocks. We prepare a hydrogel substrate with two gelatin layers of comparable height in an acrylic cube of dimensions 150 x 150 x 150 mm. The bottom layer is labeled 1, and the top layer 2. The layers have different Young's moduli noted E_1 and E_2, respectively. The fluid is injected into the bottom layer (layer 1) through a needle ($ID = 1$ mm) inserted 55 mm above the bottom of the cube as shown in figure 4.1(a). For imaging purposes, a small plastic washer is fitted onto the tip of the needle so the fracture propagates in the plane perpendicular to the needle. The thickness of the gelatin layers and needle position ensure that the fracture propagation is not affected by the finite size of the transparent cube [27].

The layers are made of gelatin, a clear gel whose Young's modulus can be tuned by varying the weight fraction of gelatin powder (Gelatin type A; Sigma-Aldrich, USA) in ultra-pure water. Gelatin has been extensively used to study hydraulic fracturing [43, 39, 28, 42]. The gelatin of the first layer is prepared by heating water to 60 °C and slowly adding the mass of gelatin powder needed to achieve the Young's modulus E_1 [41]. The mixture is poured into the cube. The gel cools down for 2 hours at room temperature. The gelatin for the second layer is prepared using a different amount of gelatin powder to obtain a Young's modulus E_2. To avoid softening the first layer and blurring the interface, the gelatin mixture for the second layer is cooled down to 40 °C

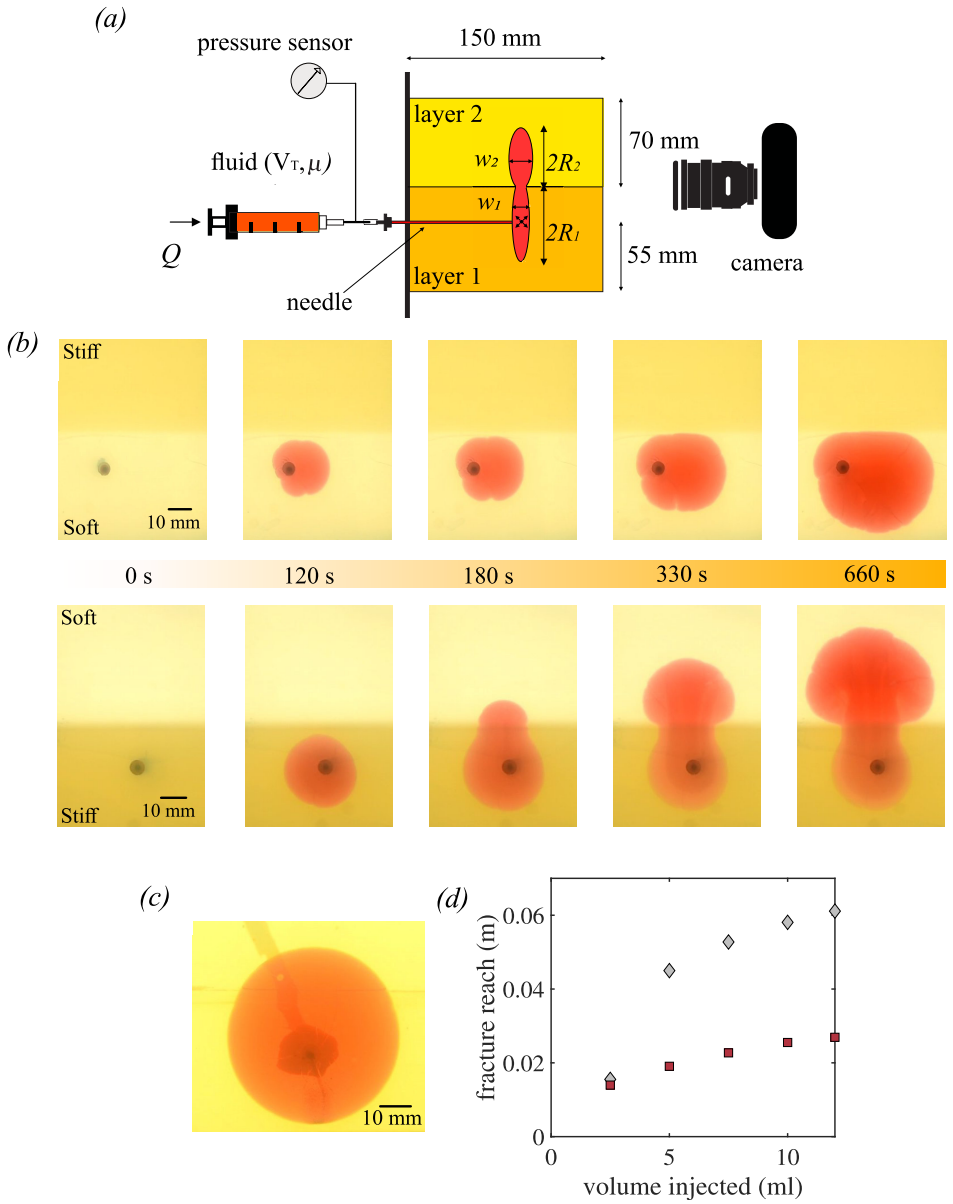

Figure 4.1: Experimental set-up and observations. (a) Schematic of the experimental set-up. (b) Times series of the fracture propagation in the fracture plane, for experiments 1 (top row) and 2 (bottom row) at times t = [0, 120, 180, 330, 660] s, with $t = 0$ the onset of the fracture in layer 1. The silicone oil ($\mu = 20$ mPa.s) is injected at $Q = 1$ ml.min^{-1}. The two layers have Young's moduli $E_{\text{soft}} = 15$ kPa and $E_{\text{stiff}} = 30$ kPa. In Exp. 1, layer 1 is softer, and in Exp. 2, layer 1 is stiffer. (c) Fracture formed upon injection of silicone oil ($\mu = 20$ mPa.s) at $Q = 1$ ml.min^{-1} for 500 s in two layers of Young's modulus $E = 30$ kPa (Experiment 3, see figure 4.6 for corresponding time series). (d) Fracture reach or maximum distance between the injection point and the fracture tip, as a function of the volume injected for Experiments 1(■) and 2(◆).

before pouring on top of the first layer. This temperature allows for good bonding of the gelatin layers. The two layers subsequently cool down to room temperature and set over 24 hours before fracturing [35].

To study the fracture propagation, we inject a volume V_T of silicone oil of viscosity μ at a constant flow rate Q with a syringe pump (kdScientific Legato 200). The oil is stained with a red dye (Sudan red) for visualization. After a volume $V_0 < V_T$ of oil is injected, the fracture reaches the interface between the two layers. The propagation is recorded using a Nikon D5300 camera with an LED panel, ensuring uniform backlighting. The images are processed using a custom-made MATLAB code to determine the contour of the fracture. A membrane pressure sensor (ATO-PRES-P350) measures the pressure of the injected fluid. We record the fracture aperture using the light attenuation method [59, 41]. The fractures propagate in the toughness-dominated regime; their growth is limited by the toughness of the material rather than the viscous dissipation in the flow [22, 28, 32].

We study the influence of material stiffness and injection parameters on fracture dynamics. The parameters are summarized in table 4.2. We explore a range of Young's modulus ratios between the two layers, from 1 to 4. Additionally, we vary the viscosity of the fluid within an order of magnitude, from 0.01 to 0.1 Pa.s. Furthermore, the volumetric flow rate spans from 0.1 to 1 ml.min^{-1}. These parameters ensure the fracture propagation occurs within the toughness-dominated regime for both layers [22, 28, 32]. A fracture growing in a single material experiences a viscous-dominated growth early on, followed by a toughness-dominated growth for times larger than a threshold or transition time. The transition time noted $t_{vt} = {\mu'}^{5/2} {E_i'}^{13/2} Q^{3/2} / {K_i'}^9$, where $i = \{1, 2\}$, spans from 6×10^{-15} to 3×10^{-9} s for our study. These values corroborate that the fracture propagation occurs in the toughness-dominated regime. The material properties are measured in the laboratory as described in [41]. The experimental error is estimated

Exp.		E_1 (kPa)	E_2 (kPa)	V_T (ml)	μ (Pa.s)	Q (ml/min)	$\boldsymbol{V_0}$ (ml)	$\boldsymbol{R_{1,f}}$ (m)
1†		15	30	12	0.02	1	-	-
2*†		30	15	12	0.02	1	2.77	0.016
3		30	30	10	0.02	1	-	-
4		15	30	10	0.01	0.5	-	-
5		15	60	10	0.02	1	-	-
6*		30	60	10	0.02	0.5	-	-
7		30	15	12	0.1	0.5	3.85	0.018
8		60	15	10	0.02	1	3.35	0.016
9		60	15	12	0.02	0.5	3.68	0.021
10*		60	30	10	0.02	0.5	4.04	0.022
11		30	15	10	0.01	0.1	7.79	0.026
12*		88	60	10	0.02	0.5	2.88	0.018
13		30	15	10	0.01	0.5	5.3	0.023
2^r		30	15	12	0.02	1	1.7	0.012

Table 4.1: List of experiments: symbols and parameters. Pressure measurements for experiments with a * and aperture measurements for experiments with a †. The values of $\mathbf{V_0}$ and $\mathbf{R_{1,f}}$ are measured. For experiments with no value listed for $\mathbf{V_0}$ and $\mathbf{R_{1,f}}$, the fracture is trapped in layer 1.

by conducting an error analysis based on the scaling laws and measurement errors for the parameters: 10% for Young's modulus E, 10% for the fracture toughness K, 0.35% for the flow rate Q and, 1% for the viscosity μ. Using these values, the experimental error for radius measurements is around 10% in the toughness regime. We measure the fracture aperture for experiments 1 and 2 using the light attenuation method [59]. Sudan red is added to the silicon oil at a concentration of 0.025 g.L^{-1}. The light absorbance at $\lambda = 520$ nm varies linearly as a function of the fracture aperture. We obtain aperture values across the fracture after calibration in a custom-made acrylic wedge [41]. We also measure the pressure for experiments 2, 6, 10, and 12.

4.3 Observations: Stiffness contrast controls growth dynamics

As oil is injected into the gelatin, a fracture forms around the needle. An axisymmetric fracture propagates over and beyond the washer, expanding radially towards the interface between layers 1 and 2, as shown in figure 4.1(b). To determine how the stiffness contrast between the two layers affects the fracture propagation, we inject oil in gelatin blocks with matching Young's moduli for the soft and stiff layer, respectively 15 and 30 kPa. For experiment 1, layer 1 is the softer layer, and the fracture growth is presented in the top row of figure 4.1(b). For experiment 2, layer 1 is the stiffer layer, and the results are in figure 4.1(b). Despite identical injection parameters ($Q = 1$ ml.min^{-1} and $\mu = 20$ mPa.s), the fractures produced exhibit different geometry and propagation dynamics once they reach the interface. In experiment 1, the fracture continues to propagate in the soft layer, adopting an elongated geometry [122]. In experiment 2, the fracture crosses over to the second and softer layer upon reaching the interface. The fracture initially adopts a half-disk shape in the soft layer. In comparison, when the two layers have the same Young's modulus, the fracture adopts a circular geometry (see figure 4.1(c)). This observation indicates that the contrast in stiffness between the layers is responsible for the modified shape and dynamics, and not the presence of an interface between two gelatin layers. To complete this comparison between the two dynamics at the interface, we consider the fracture reach in figure 4.1(d). The reach or the maximum distance between the tip of the needle and the contour of the fracture depends on the relative stiffness of the injection layer. The reach of a fracture that originates in the stiffer layer and eventually propagates in the softer layer is greater than that of a fracture that forms and remains trapped in the softer layer. These observations show that the relative stiffness of the layer in which the fracture forms compared to the adjacent layer determines if, how much, and

how fast the fracture will propagate into the adjacent layer.

To understand the response of the fracture to a stiffness contrast, we consider the ratio of the pressure required to propagate the fracture in the different layers. The ratio depends on the material stiffness and can be approximated as $P_2/P_1 \propto \sqrt{\gamma_1 G_1/\gamma_2 G_2}$, where γ is the fracture energy and G the shear modulus [123]. Since both layers are made of gelatin and have the same fracture energy $\gamma \approx 1$ J.m^{-2}, and Poisson's ratio $\nu \approx 0.5$ [38], the relation simplifies to $P_2/P_1 \propto \sqrt{E_1/E_2}$. Therefore, when the fracture reaches the interface between the two layers, it preferentially propagates in the layer with the lowest Young's modulus or lowest propagation pressure. This is consistent with the trapping of the fracture that originates in the softer layer and the mushroom-like geometry of the fracture in the softer layer 2.

We now focus on the dynamics of a fracture that grows from a stiff into a soft layer; we measure the pressure and geometrical features of the fracture for Experiment 2. In figure 4.2(a) we present side views of the growing fracture. The corresponding pressure values are plotted in figure 4.2(b). At the start of the injection (point 1), the fluid pressure increases until it reaches a critical value necessary to initiate and propagate the crack [30]. Once the fracture forms (point 2), there is a rapid pressure release, and then the propagation becomes quasi-steady. Upon further injection, the fracture reaches the interface (point 3), and the pressure drops rapidly. After this transient, the pressure evolution becomes quasi-steady again until the end of the injection (point 4). The corresponding radius measurements are presented in figure 4.2(c). The radius values are obtained from the area of the sub-fractures, allowing us to define an effective radius for non-axisymmetric fractures. The fracture grows in the stiffer layer until it reaches the interface (point 3). Then, the fracture stops expanding in layer 1, while its radius in layer 2 increases rapidly. In summary, the propagation into the softer layer arrests the radial growth of the fracture in the stiffer layer. Simultaneously, the aperture of the fracture

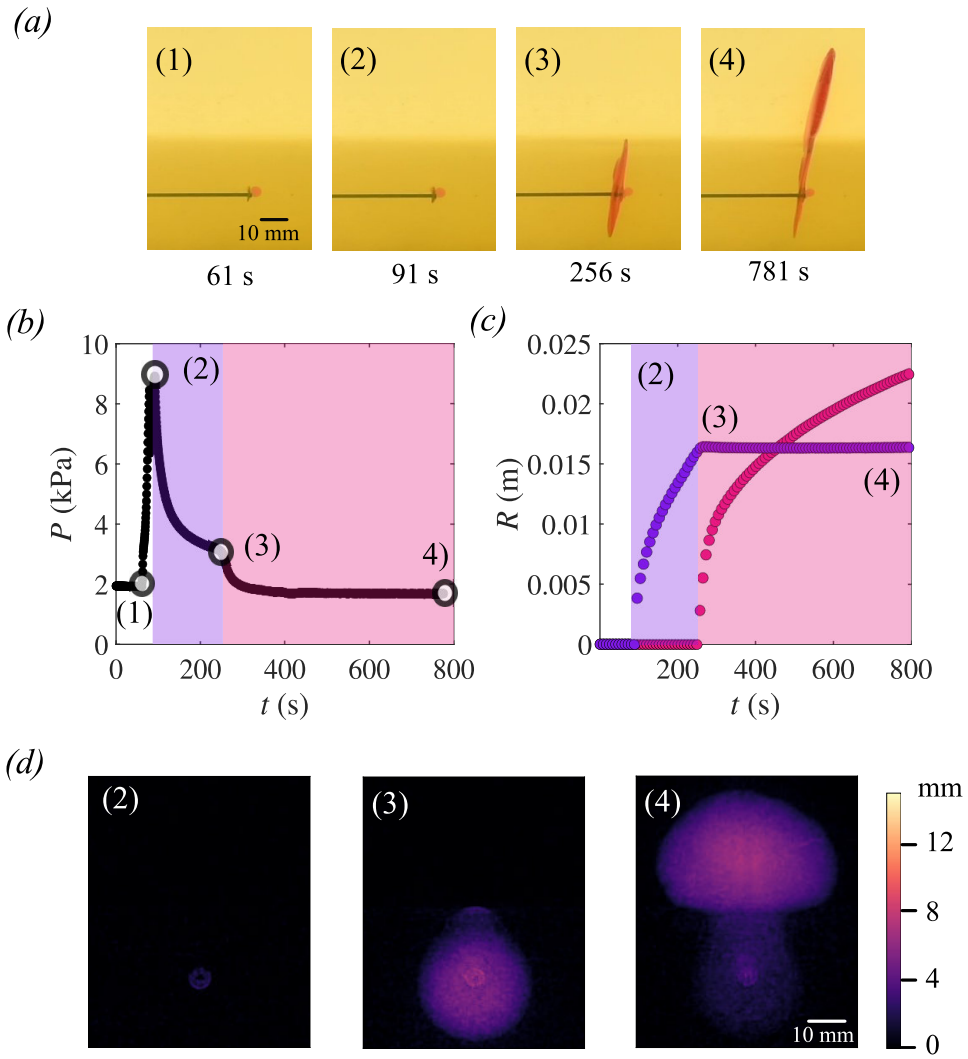

Figure 4.2: Fracture dynamics in Experiment 2: (a) Time series of side views of the fracture. (b) Fluid pressure during the injection. (c) Effective radius of the fracture in layer 1 ● and in layer 2 ●. (d) Aperture of the fracture. The heat map indicates the local aperture in layers 1 and 2. We note: 1 the onset of the injection, 2 the initiation of the fracture in the stiffer layer (layer 1), 3 the crossing of the interface toward the softer layer (layer 2), and 4 the profile at the end of the injection.

decreases in layer 1 and increases in layer 2, as shown in figure 4.2(d). These observations are reminiscent of the backflow dynamics reported by Lai et al [40]. In backflow processes, the hydraulic fracture is connected to an outlet at atmospheric pressure with tubing, which offers less resistance to the flow than the fracture propagation. The backflow is due to the fracture collapse: its aperture decreases while its radius remains constant. In our experiments, the propagation in the soft layer requires a lower pressure than the growth in the stiffer layer, driving fluid from layer 1 into layer 2.

4.4 Results and discussion

To model the dynamics of a fracture that propagates through a stiffness contrast, from a stiff to a soft layer, we start by reviewing the scaling laws that describe the fracture growth in a homogeneous material. We then model the couplings between the two "sub-fractures", as fluid flows from the sub-fracture 1 in the stiffer layer 1 into the growing sub-fracture 2 in the softer layer 2.

4.4.1 Theoretical model

When the fracture forms and grows in a homogeneous material i, the propagation dynamics are driven by the elastic deformation and limited by the fracture opening or toughness of the material. In all experiments presented here, the viscous dissipation associated with the flow in the fracture is negligible. This mode of propagation is toughness-dominated. The fluid injection starts at $t = 0$ (point 2 in figure 4.2). At time t, the volume of the fracture is equal to $V = Qt_i \approx R_i^2 w_i$, where R_i and w_i are the radius and maximum aperture of the fracture. Assuming there is no fluid lag [124], the theory of Linear Elastic Fracture Mechanics (LEFM) holds. The fracture propagates in mobile equilibrium and the pressure scales as $P_i \approx E_i' w_i / R_i$, where $E_i' = E_i/(1-\nu^2)$. The

fracture propagation criterion yields $K_i \approx P_i\sqrt{R_i} \approx 4\sqrt{2E_i'\gamma/\pi}$ with K_i stress intensity factor for a penny-shaped fracture set equal to the fracture toughness K_{IC}. Solving these three equations, we get the scaling expressions governing R_i, w_i and P_i [22, 103],

$$R_i \approx \left(\frac{E_i'}{K_i'}\right)^{2/5} V^{2/5} \tag{4.1}$$

$$w_i \approx \left(\frac{K_i'}{E_i'}\right)^{4/5} V^{1/5} \tag{4.2}$$

$$P_i \approx \left(\frac{{K_i'}^6}{{E_i'}}\right)^{1/5} V^{-1/5} \tag{4.3}$$

In the toughness-dominated regime, the propagation dynamics depends on the material properties and flow rate at which the liquid is injected Q. These scaling or power-law expressions describe the fracture growth in layer 1.

We now consider the growth dynamics of the fracture when it reaches a softer material in layer 2. The rapid growth in the soft layer is due to the material properties and is fueled by the collapse of the sub-fracture in layer 1. Based on experimental observations, we assume that the radius of the fracture in layer 1 remains constant, equal to $R_{1,f}$, and the maximum aperture $w_1(t)$ decreases over time. Since the fracture propagation in layer 1 is toughness-dominated, the material toughness sets the pressure. As the fracture crosses the interface, the pressure in the fluid is greater than necessary to propagate in layer 2. This is consistent with the initial sudden drop in pressure observed in Experiment 2, see figure 4.2(b). The pressure decreases from the value set by the toughness of layer 1 to the value set by the toughness in layer 2. After a short transient regime, the pressure is considered constant throughout the fracture, with the pressure in the two layers $P \approx P_1 \approx P_2$. We use a similar mathematical framework as for the fracture propagating in a uniform material. We derive expressions for the effective radius R_2 and maximum aperture w_2 in layer 2, maximum aperture w_1 in layer 1, and pressure

P. We note V_0 the fracture volume when it reaches the interface. After crossing the interface, the fracture volume is $V \approx V_0 + Qt_2 \approx R_{1,f}^2\, w_1 + R_2^2\, w_2$ where $t_2 = 0$ is the time at which the fracture crosses the interface (point 3 in figure 4.2). The elastic pressure scales as $P_1 \approx E_1' w_1/R_{1,f}$ and $P_2 \approx E_2' w_2/R_2$ with $P \approx P_1 \approx P_2$. Since the fracture grows in layer 2, the propagation criterion is set by the material properties of layer 2: $K_2 \approx P\sqrt{R_2} \approx 4\sqrt{2E_2'\gamma/\pi}$. We employ an iterative approach to solve this system of equations, as detailed in §4.6. This approach yields closed-form expressions that model fluid transfer from sub-fracture 1 to sub-fracture 2 while preserving the long-term toughness scaling in layer 2. In solving for the fracture parameters and pressure, we can estimate V_0', the volume of fluid transferred from sub-fracture 1 into sub-fracture 2 at time t_2:

$$V_0' \approx V_0 - \frac{R_{1,f}^3}{{E_1}'} \left(\frac{{K_2}'^6}{{E_2}'} \right)^{1/5} (V_0 + Qt_2)^{-1/5}. \tag{4.4}$$

V_0' is an increasing function of time with $V_0' \to V_0$ at large time. This result indicates that fluid drainage from sub-fracture 1 into sub-fracture 2 is a function of the stiffness of the two layers and the volume of the fracture when it reaches the interface. The fluid transfer does not depend on the fluid viscosity, which is consistent with the toughness-dominated regime studied here. Using $V_0' + Qt_2$ as the volume of sub-fracture 2, equations 4.1, 4.2, and 4.3 describe the evolution of the effective radius and maximum aperture in layer 2 and the fracture pressure, respectively. The maximum aperture of sub-fracture 1 is

$$w_1 \approx \left(\frac{{K_2}'^6}{{E_2}'} \right)^{1/5} \left(\frac{R_{1,f}}{{E_1}'} \right) ({V_0}' + Qt_2)^{-1/5} \tag{4.5}$$

The volume of fluid in sub-fracture 2 is the sum of the volume injected by the syringe pump after the fracture reaches the interface and the volume transferred from sub-fracture 1. As the volume transferred is an increasing function of time, the properties of the

fracture are not captured by power laws until $V_0' \approx V_0$. At long timescale, $V_0' \approx V_0$, those equations recover the scalings derived for the toughness-dominated propagation in layer 2 for a fracture volume equal to the total volume injected, $V \approx V_0 + Qt_2$.

4.4.2 Comparison with experimental results

Experimentally, we vary the stiffness of the two layers, the fluid viscosity, and the injection parameters (flow rate and total volume), as detailed in Table 4.2. We report the volume injected when the fracture reaches the interface between the two layers and crosses into layer 2. We measure the fracture radius in the first layer R_1, and report the data in figure 4.3(a). Upon rescaling the radius values using equation 4.1, all data sets collapse onto a single curve in figure 4.3(b). The best-fitting power law for this curve is described by $R_1 = \alpha_1 (E_1'/K_1')^{2/5} (Qt)^{2/5}$, with $\alpha_1 = 0.65$, a value which is consistent with previous studies [22, 29, 32]. Similarly, the fracture aperture and pressure scale are in agreement with equations 4.2 and 4.3 as shown in figures 4.9 and 4.10(a) and (b). We note that those measurements include experiments with a softer injection layer. These results indicate that the propagation dynamics in layer 1 are not modified by the interface (figure 4.7), even when a stiffer material across the interface confines the propagation to layer 1, resulting in an elongated fracture.

When layer 1 is stiffer than layer 2, the fracture crosses over to layer 2 when it reaches the interface. We measure the effective radius of the fracture in layer 2; the results are presented in figure 4.3(c). Initially, we observe a rapid increase in radius, characteristic of the swift transfer occurring between the two layers. Upon rescaling the data using equation 4.1 with $V = V_0' + Qt_2$, the profiles converge onto a master curve as shown in figure 4.3(c). The proposed model captures the fracture dynamics within a few seconds of the interface crossing. The best-fitting power law for this unified curve is described

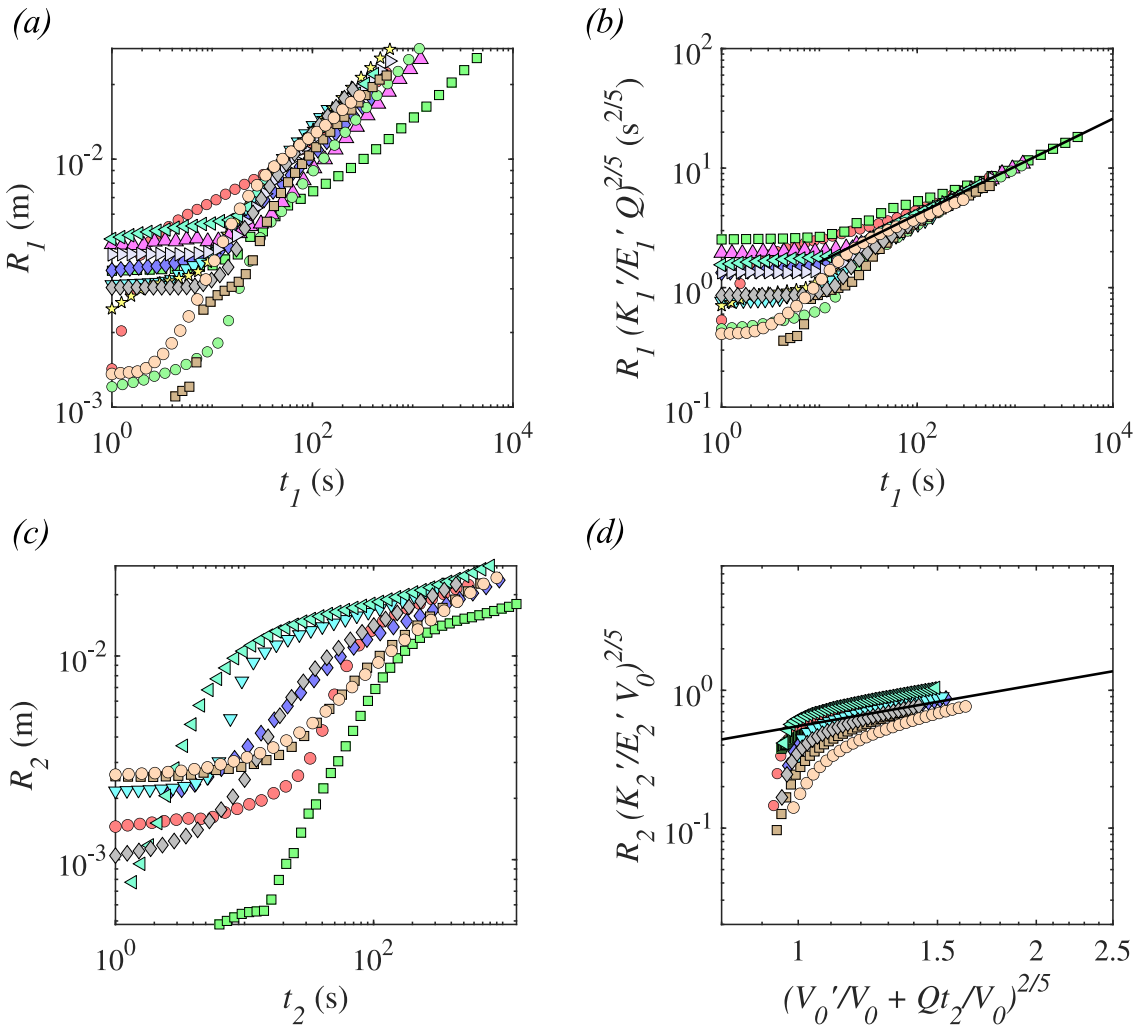

Figure 4.3: Comparison between experiments and modeling. (a) Effective fracture radius in layer 1 R_1 as a function of time for Experiments 1 to 13. $t_1 = 0$ marks the initiation of the fracture. We report values for the growth phase of the fracture, i.e., until the fracture crosses over to layer 2, when applicable. (b) Rescaled fracture radius in layer 1 for Experiments 1 to 13 using equation 4.1. (c) Effective radius in layer 2 R_2 as a function of time t_2 for Experiments 2, 7-13. $t_2 = 0$ marks the onset of the fracture propagation in layer 2. (d) Scaled radius in layer 2 for the corresponding experiments using equation 4.4.

by $R_2 = \alpha_2 (E_2'/K_2')^{2/5} (V_0' + Qt_2)^{2/5}$, with $\alpha_2 = 0.57$. This is consistent with the values obtained in the toughness regime. At later times, when the rate of drainage of sub-fracture 1 is negligible compared to the injection rate, sub-fracture 2 grows according to the power-law of time, as expected for a fracture propagating in a single material (see figure 4.11). The fracture aperture is measured along a line normal to the interface and going through the injection point, as shown in figure 4.4(a). We can, therefore, measure the aperture of both sub-fractures. The results presented in figure 4.4(b) show that the aperture of sub-fracture 1 decreases as the aperture of sub-fracture 2 increases over time. We rescale the fracture profiles using equations 4.1 and 4.2 and present the results in figure 4.4(c). We see that the fracture profiles in layer 2 collapse, whereas fracture profiles in layer 1 do not. If we rescale the fracture aperture using equation 4.5 and a fixed radius, $R_{1,f}$, the fracture profiles in layer 1 collapse onto each other, as shown in figure 4.4(d). The pressure values recorded during the fracture growth in layer 2 follow the scaling in equation 4.3 as shown in figure 4.10(c) and (d).

In summary, the radius, aperture, and pressure measurements offer conclusive evidence of the fluid transfer from layer 1 to layer 2. The growth dynamics of the fracture in layer 2 result from the combination of fluid transfer or fracture history and fluid injection at a constant flow rate.

4.5 Conclusions and Perspectives

Fluid injection and sequestration in geological formations constitute a practical approach to achieving net-zero greenhouse gas emissions. Hydraulic fractures increase the storage capacity of low-permeability reservoirs. Yet, in stratified rocks, the nonuniform material properties and stress fields can reorient the propagation plane of the fracture, resulting in complex fracture trajectories and geometry [123, 117, 119, 35]. In this paper,

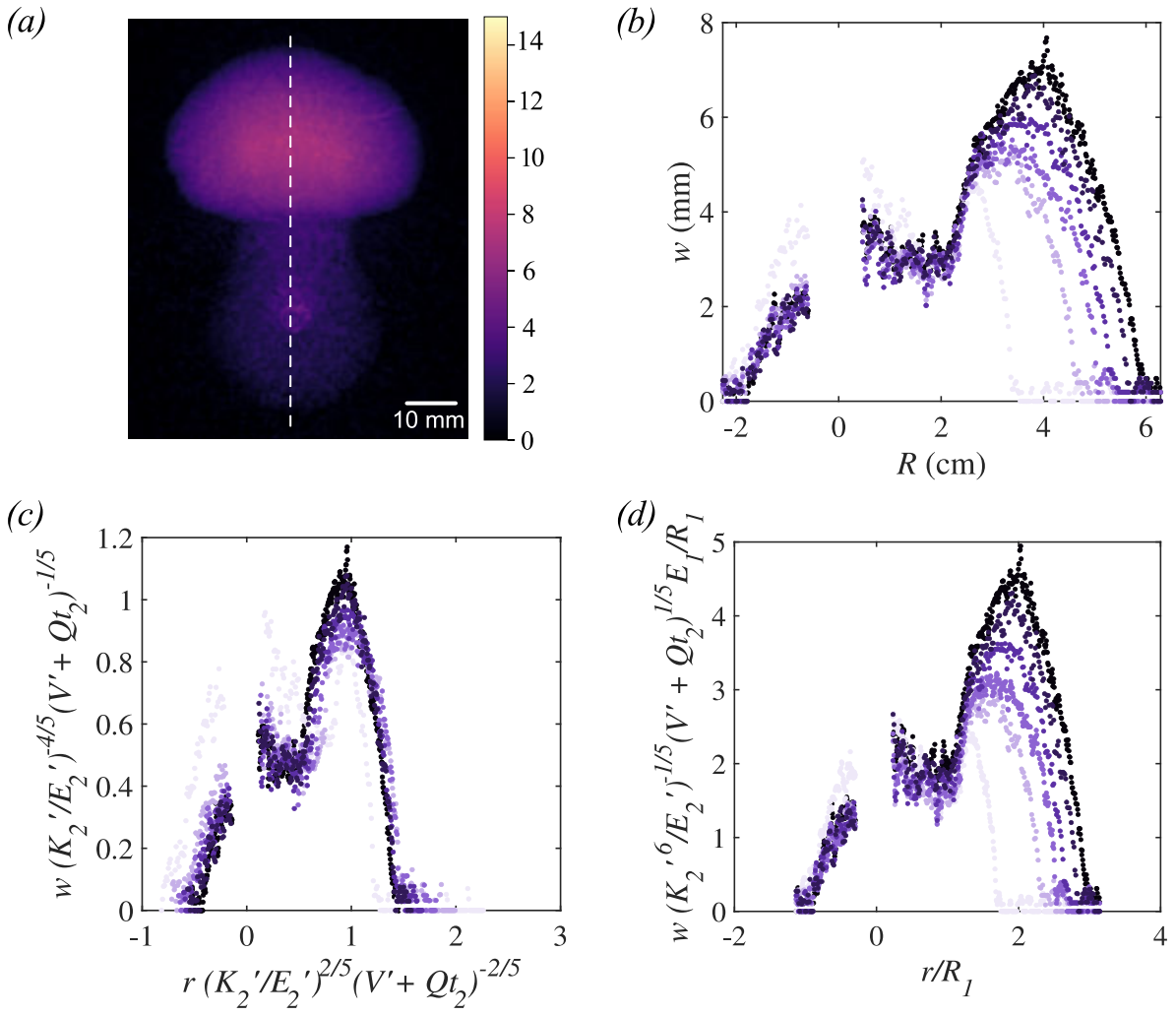

Figure 4.4: Aperture measurements. (a) Heat map of a fracture aperture from Experiment 2. The white line depicts the line along which the thickness of the fracture is measured. (b) Aperture values w or fracture profile measured during Experiment 2 at $t_2 = [21, 111, 201, 291, 381, 471]$ s, with time increasing from light to dark purple. (c) Rescaled aperture profiles using equations 4.1 and 4.2, for the propagation in layer 2. (d) Rescaled aperture profiles using $R_{1,f}$ and equation 4.5 to describe the fracture collapse in layer 1.

we have shown that the fracture can undergo enhanced or confined propagation because of differences in stiffness between two neighboring layers. Our results demonstrate that a fracture growing from a stiff into a soft layer experiences faster expansion dynamics due to the transfer of fluid from the stiff to the soft layer. Once the fluid originally in the stiff layer is drained, the fracture propagation slows down to its toughness-dominated growth rate set by the injection flow rate and the toughness of the material. A fracture formed in a stratified rock formation will behave differently due to the complexity of the rock structure and stress field, yet stiffness contrasts will still cause variations in the propagation dynamics. The fracture geometry will depend on the growth history and relative stiffness of the layers encountered. We, therefore, anticipate that our findings should have practical implications for the selection of injection sites and operation conditions, as the propagation dynamics are highly sensitive to the properties of the successive rock layers encountered.

4.6 Appendix

Mathematical model

In this section, we provide the derivation of the model that describes the fracture growth into a softer layer after reaching a stiffness contrast.

Governing equations

When the fracture propagates from layer 1 to layer 2, it exclusively grows within layer 2. The thickness of fracture w_1 in layer 1 gradually decreases over time, while the radius R_1 remains constant at $R_{1,f}$ [40].

For a penny-shaped fracture growing in a material with a Young's modulus E, the

radius R, fracture aperture w and pressure P verify [18, 22]:

$$w(r,t) = \frac{8(1-\nu^2)R}{\pi E} \int_{r/R}^{1} \frac{\xi}{\sqrt{\xi^2 - (r/R)^2}} \int_0^1 \frac{xP(x\xi R, t)}{\sqrt{1-x^2}}\, dx\, d\xi. \tag{S1}$$

In the two-layer system, we use the index $i = \{1, 2\}$ to specify the sub-fracture and layer of interest. We label the geometry of the sub-fractures (R and w), pressure P, and Young's modulus E accordingly. Using a dimensional approach and the characteristic parameters, we can approximate the fracture aperture in both layers as follows:

$$w_1 \approx \frac{P_2 R_{1,f}}{E_1'} \tag{S2}$$

$$w_2 \approx \frac{P_2 R_2}{E_2'} \tag{S3}$$

where $E_i' = E_i/(1-\nu^2)$ where ν is the Poisson's ratio.

When the fracture is propagating in layer 2, the growth is limited by the energy required to create new fracture surfaces. The fracture propagates when the mode 1 stress intensity factor (K_2) is equal to or greater than the plane strain fracture toughness (K_{IC}) of the material [105]. This can be written as

$$K_2 = K_{IC} \tag{S4}$$

After a rapid transition, experimental measurements indicate that the pressure can be considered uniform. Since the fracture is propagating in the toughness regime, the pressure in the fracture is set by the stress intensity factor at the propagating tip and can be approximated as

$$P_2 \approx P_1 \approx K_2'/\sqrt{R_2} \tag{S5}$$

where $K_2' = 4(2/\pi)^{0.5}\sqrt{2E_2'\gamma}$ and $\gamma = 1$ J/m^2 is the fracture energy for gelatin [33, 63].

If V_0 is the volume in the fracture right before the fracture penetrates into layer 2 at time $t_2 = 0$, the net volume in the fracture at t_2 is

$$V_0 + Q\,t_2 = 2\pi \int_0^{R_{1,f}} r_1 w_1(r_1, t_2) dr + 2\pi \int_0^{R_2} r_2 w_2(r_2, t_2) dr, \tag{S6}$$

Therefore,

$$V_0 + Q\,t_2 \approx R_{1,f}^2\, w_1 + R_2^2\, w_2. \tag{S7}$$

To predict the evolution of R_2, w_2, w_1, and P, we can solve equations S2, S3, S5, and S7. This coupled system of equations yields a 6th-order polynomial equation whose exact roots are not conducive to capturing the core physics of the phenomenon. Consequently, we adopt an alternative approach to derive approximate solutions.

We assume that all of the fluid in layer 1 has drained into layer 2, which is a late-time behavior. The fracture pressure P is

$$P \approx \frac{{K_2}'^{6/5}}{{E_2}'^{1/5}} (V_0 + Q t_2)^{-1/5} \tag{S8}$$

Substituting equation S8 in equation S2 and solving for w_1 we get,

$$w_1 \approx \frac{{K_2}'^{6/5}}{{E_2}'^{1/5}} (V_0 + Q t_2)^{-1/5} \frac{R_{1,f}}{{E_1}'} \tag{S9}$$

Experimental results show that the fracture grows in layer 2 while sub-fracture 1 drains. Therefore, we assume the fluid injected Qt_2 is entirely contributing to the growth of the fracture in layer 2. In addition, the fluid draining out of sub-fracture 1 goes into layer 2. Substituting equation S9 in equation S7, we derive an expression for the volume of the

fluid V_0' moving from layer 1 to layer 2 as a function of time,

$$V_0{}' \approx V_0 - \frac{{K_2{}'}^{6/5}}{{E_2{}'}^{1/5}}(V_0 + Qt_2)^{-1/5}\frac{R_{1,f}^3}{E_1'}. \tag{S10}$$

Using the above-corrected volume to account for the draining of fracture in layer 1, we get the following equations

$$P \approx \frac{{K_2{}'}^{6/5}}{{E_2{}'}^{1/5}}(V_0{}' + Qt_2)^{-1/5} \tag{S11}$$

$$w_1 \approx \frac{{K_2{}'}^{6/5}}{{E_2{}'}^{1/5}}(V_0{}' + Qt_2)^{-1/5}\frac{R_{1,f}}{E_1{}'} \tag{S12}$$

$$w_2 \approx \frac{{K_2{}'}^{4/5}}{{E_2{}'}^{4/5}}(V_0{}' + Qt_2)^{1/5} \tag{S13}$$

$$R_2 \approx \frac{{E_2{}'}^{2/5}}{{K_2{}'}^{2/5}}(V_0{}' + Qt_2)^{2/5} \tag{S14}$$

These equations have the same form as the scaling relations for the toughness regime, but here, the volume of the fracture is not a linearly increasing function of time. The power-law dependence in the toughness regime is recovered when $V_0 << Qt_2$.

Comparison between scaling and analytical roots

We assess the performance of our scaling expressions and compare them against the permissible roots of the 6th-order equation obtained from equations S2, S3, S5, and S7. For this evaluation, we focus on Experiment 2 and employ the corresponding experimental parameters to determine the roots of the polynomial equation. Upon solving, we observe that only one admissible real root exists. Subsequently, we generate a plot showcasing the actual values of various quantities and those calculated using our scaling expressions. As illustrated in figure 4.5, our scaling expressions closely approximate the actual roots

for R_1, w_2, P, and w_1.

Additional experimental results

Identical layers

In experiment 3, we conducted an injection into two layers, both constructed the same way as in our other experiments, but with an important difference: the layers had the same Young's modulus. We did this to investigate the impact of the interface we create while producing our layered gelatin material. As illustrated in figure 4.6, the fracture initiates in layer 1 and expands outward radially towards layer 2 and the interface. When it reaches the interface (indicated by the dashed black line), the fracture continues to propagate as if there were no material boundary. This continuity is also evident in the radius data presented in figure 4.7(a). When we scale the radius using the toughness-limited penny-shaped fracture scaling used for layer 1, we observe consistent scaling behavior (figure 4.7(b)).

Reproducibility

We conducted Experiments 2 and 2^r to test repeatability. Because we do not control the volume of gelatin poured precisely, we measure the volume V_0 and fracture radius $R_{1,f}$ upon crossing of the interface. We compare R_1 in figure 4.8(a) and see that after the initial variations, the fractures behave similarly. When we rescale the fracture radii in layer 1, they match, as shown in figure 4.8(b). After crossing the interface, the fracture aperture w_2 and radius R_2 depend on V_0 and $R_{1,f}$. As a result, we see differences in the early times as shown in figure 4.8(c). But as time goes on, the fractures display similar growth patterns. This supports our hypothesis that, at later times, the fracture in layer 2 behaves like a single-layer penny-shaped fracture limited by the toughness of

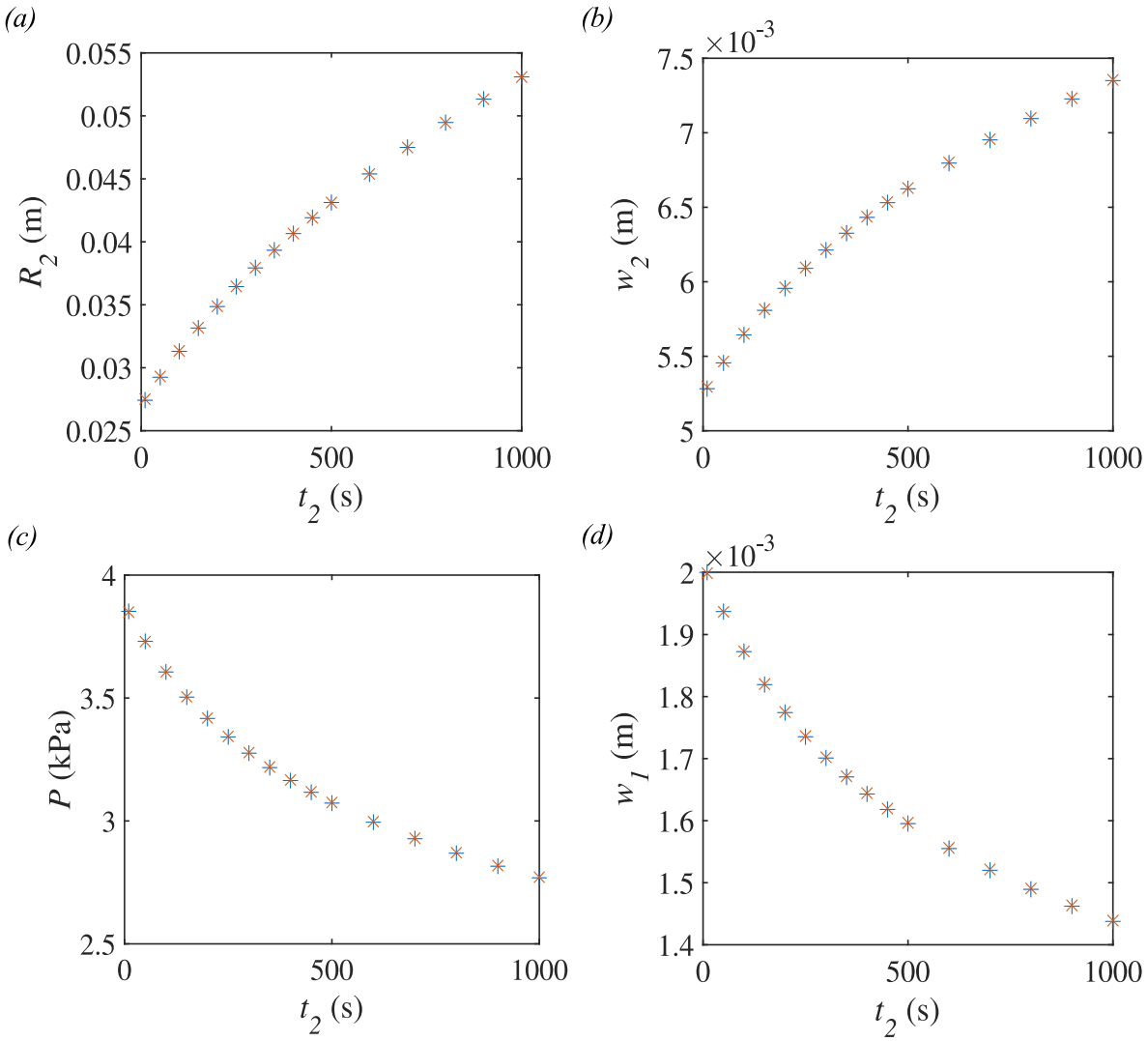

Figure 4.5: Comparison between approximate scaling solution (+) and exact solution generated using Mathematica® (x)

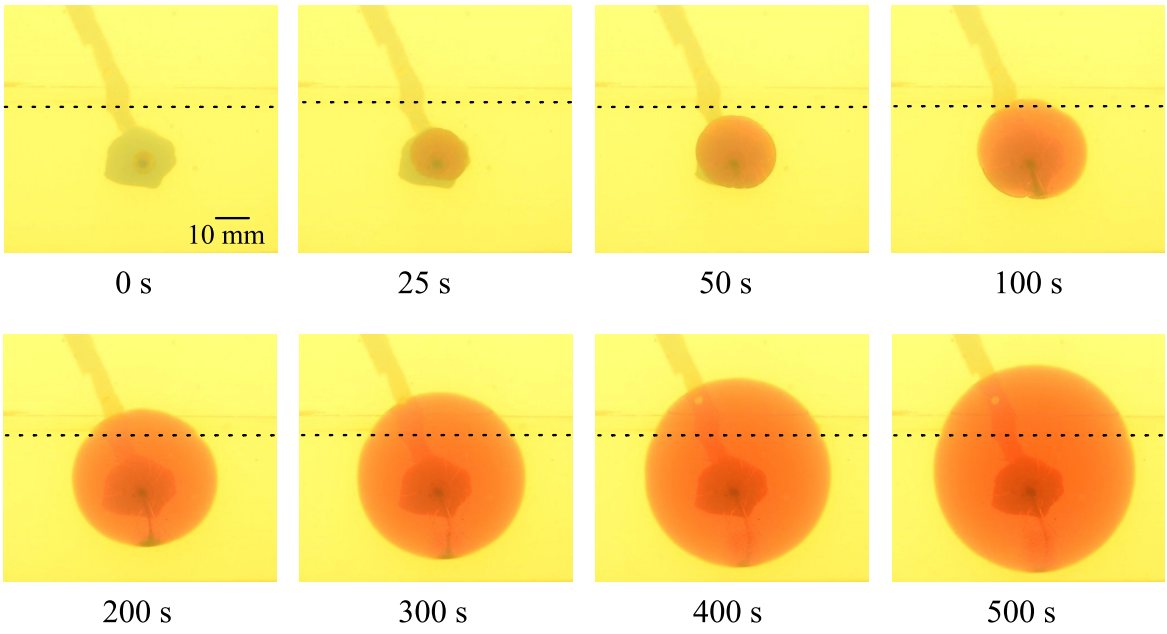

Figure 4.6: Fracture propagation when both layers have the same Young's modulus (Exp. 3). The black dotted line denotes the interface between the two layers.

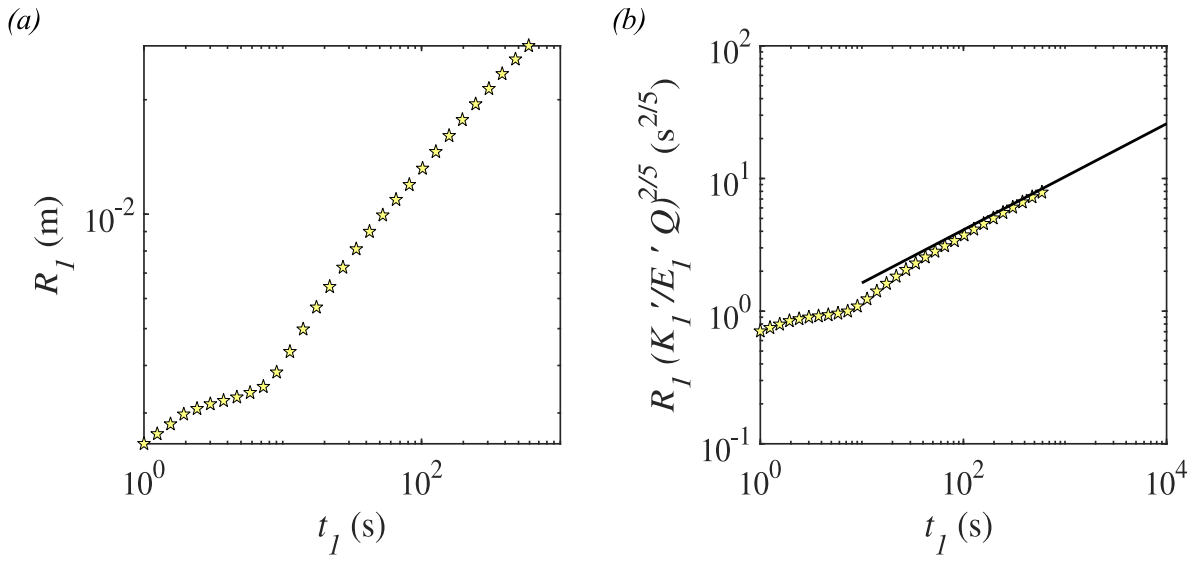

Figure 4.7: Fracture growth in two identical layers: (a) Radius of the fracture as a function of time and (b) rescaled fracture radius using the toughness scaling for a single layer. The black line represents the best-fit line for all the experiments in layer 1 and has a slope equal to 2/5.

the material. When we scale the data, we see that the fracture profiles coincide, even at early times because we take into account the differences between V_0 and $R_{1,f}$, as shown in figure 4.8(d).

Fracture aperture in layer 1

During experiment 1, we obtain the fracture profile by measuring the aperture along the diameter of the growing fracture in layer 1 at different times. We report the aperture as a function of radial position in figure 4.9(a). Upon rescaling using the toughness scaling laws [22, 29, 32], we see that the fracture profiles collapse onto each other (figure4.9(b)).

Scaling of pressure data

Using a membrane sensor, we measure the pressure in experiments 2, 6, 10, and 12. The sensor measures the pressure of the fluid in the tubing. The viscous pressure drop in the tubing and needle is two orders of magnitude lower than the toughness-dominated pressure in the fracture, assuming a fully developed pipe flow. The pressure recorded by the sensor is, therefore, primarily due to fracture propagation. In figure 4.10(a), we present the pressure values corresponding to the propagation in layer 1. When we rescale the data, we observe that the pressure data collapse on a single curve, see figure 4.10(b). The best-fitting power law is $P = \alpha_3({K_1}'^6/{E_1}')^{1/5}(Qt)^{-1/5}$, with $\alpha_3 = 0.6$. In figure 4.10(c), we report the pressure values once the fracture has advanced into layer 2. When rescaled, the pressure data converge into a horizontal line, as depicted in figure 4.10(d). The best-fit line is given by $P = \alpha_4({K_2}'^6/{E_2}')^{1/5}({V_0}' + Qt_2)^{-1/5}$, where $\alpha_4 = 0.65$.

Toughness scaling in layer 2

In figure 4.11(a), we plot the fracture radius as a function of time in layer 2 for Experiments 2 and 7 to 13. Upon using the scaling relations developed for the toughness-

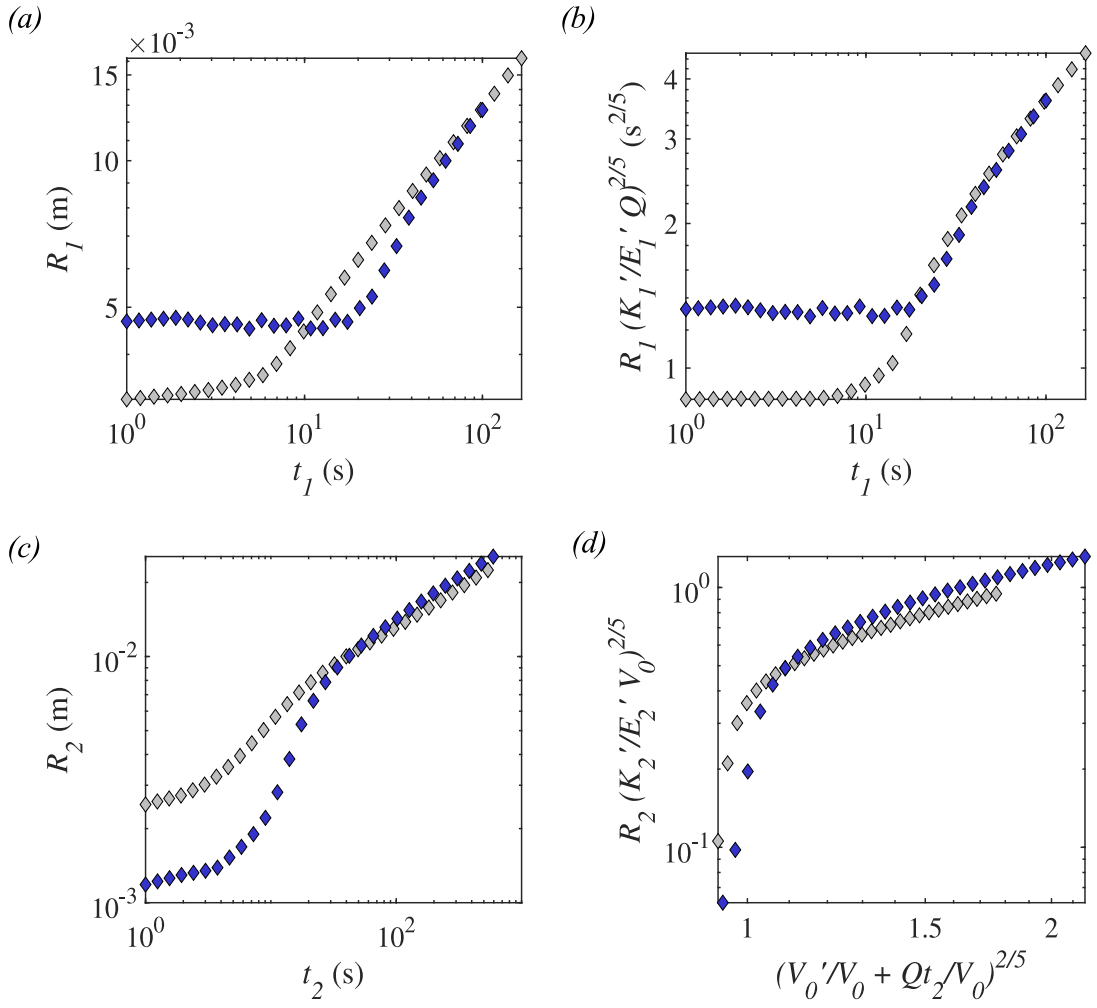

Figure 4.8: Comparison between two experiments with identical parameters (Exp. 2 and Exp 2^r): (a) time evolution of R_1 when the fracture is propagating in layer 1, (b) rescaled R_1 as a function of time using the toughness scaling (c) time evolution of the effective fracture radius R_2 in layer 2, and (d) rescaled R_2 using equations 4.1 and 4.4.

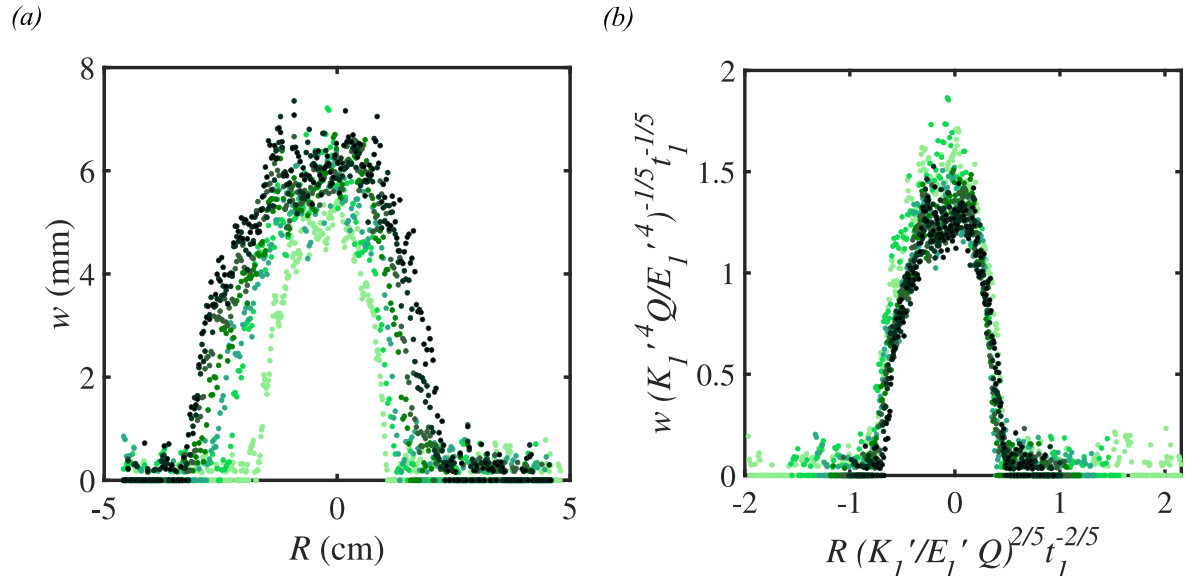

Figure 4.9: Fracture profiles in layer 1 (Exp. 1): (a) fracture aperture as a function of the radial position at $t = \{100, 200, 300, 400, 500, 600, 700\}$ s, with time increasing from light to dark green and, (b) rescaled fracture profiles using the toughness scaling.

dominated propagation, with a fracture volume equal to Qt_2, we observe that the radius values only collapse at long times, see figure 4.11(b). The best fit long-term scaling line is given by $R_2 = \alpha_5({E_2}'^{2/5}/{K_2}'^{2/5})(Qt_2)^{2/5}$ where $\alpha_5 = 0.65$.

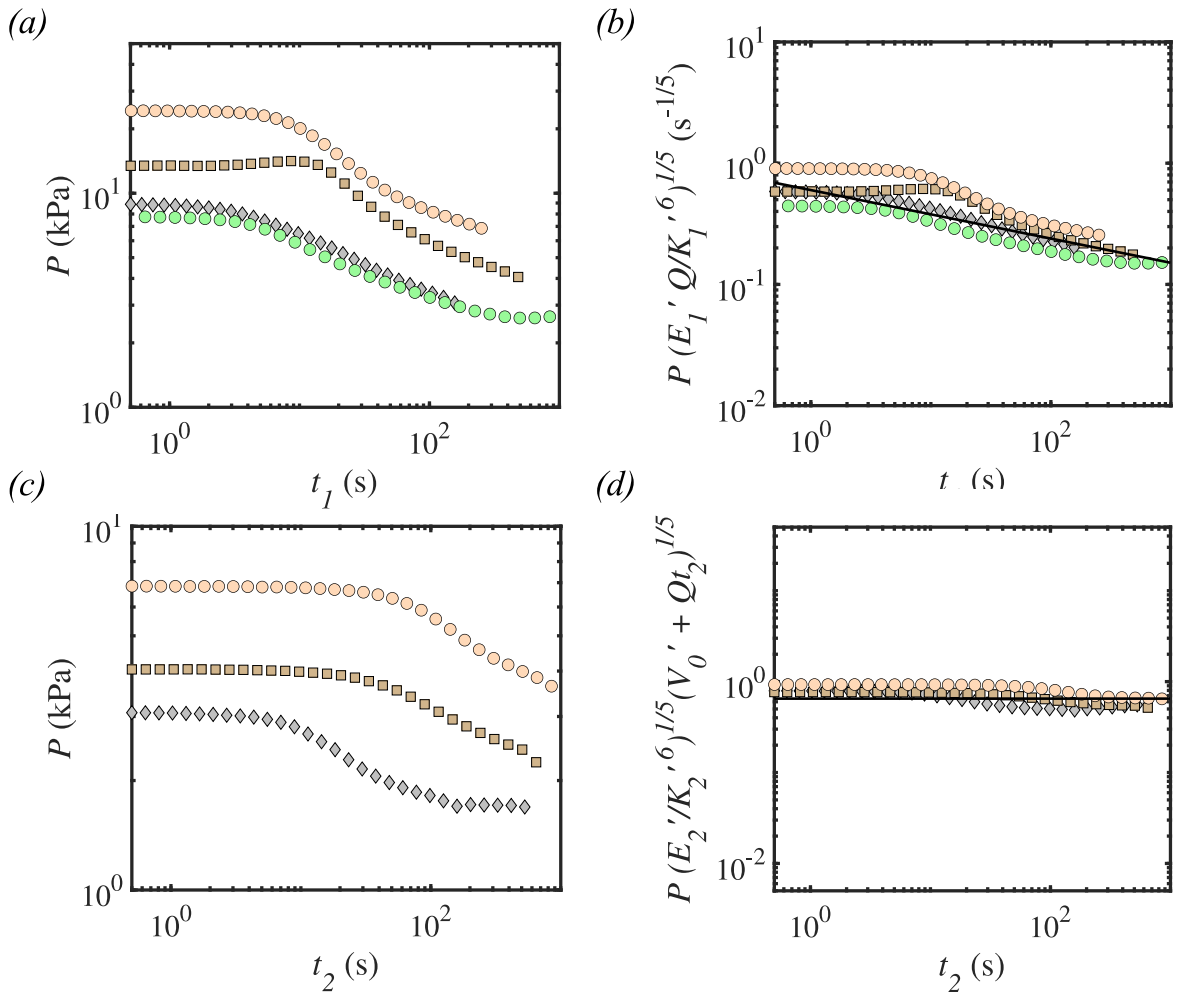

Figure 4.10: Pressure profiles: (a) pressure as a function of time when the fracture grows in layer 1 for Exp. 2, 6, 10, and 12, (b) rescaled pressure in layer 1; the black line represents the best fit with a slope of -1/5, (c) pressure as a function of time when fracture propagates in layer 2 and, (d) rescaled pressure data in layer 2 using equations 4.3 and 4.4. The black line represents the best-fit line with a slope of 1.

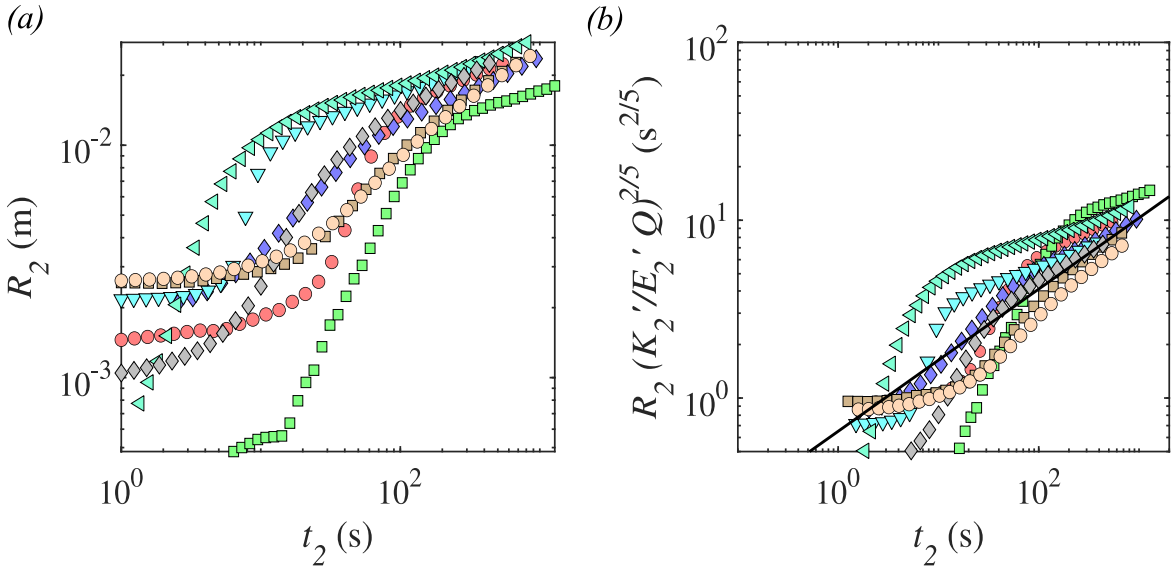

Figure 4.11: (a) Effective radius R_2 as a function of time and (b) rescaled R_2 using the single material toughness scaling with a fracture volume equal to the volume injected Q, t_2. The black line represents the best-fit line with a slope of 2/5.

Chapter 5

Conclusion and future work

In real-world scenarios where hydraulic fractures are created to enhance the permeability and porosity of rock, the fractures interact with many heterogeneous elements in the surrounding environment. These interactions encompass fluid-filled pores, material discontinuities, other cracks, fissures, etc. Understanding such a complex system is a formidable task, particularly due to the non-linear nature of fluid propagation and the singularity at the fracture tip. Therefore, laboratory scale experiments involving simple penny-shaped fractures offer a powerful tool to isolate and study the effects of various such complexities [33, 34, 40]. This thesis addresses multiple aspects of such complex hydraulic fracture propagation.

The first study presented in Chapter 2 was an experimental investigation focused on the propagation of a penny-shaped hydraulic fracture upon shut-in of injection in the viscous regime (viscous effects dominate), with no fluid leak-off to the surroundings. Depending on the injection regime, excess elastic energy may be stored in the solid medium, leading to the fracture continuing to grow even after the injection stops. We conducted a series of experiments varying the Young's modulus of the solid medium, the viscosity of the injected fluid, and the flow rate of injection.

We identified three different regimes of propagation: (i) constant flow rate, (ii) constant volume, and (iii) toughness-controlled saturation. In the fracture propagation during the constant flow rate injection, the radius of the fracture increases as $t^{4/9}$, whereas the thickness of the fracture increases as $t^{1/9}$. Once the injection stops, the fracture continues to propagate at constant volume. This implies that as the fracture radius is increasing as $t^{1/9}$, the fracture thickness has to reduce as $t^{-2/9}$ to conserve the volume in the fracture as there is no leak-off. The fracture continues to grow ever so slowly until it reaches saturation when the stress intensity factor at the tip of the fracture becomes lower than the material's toughness.

After a detailed study of a penny-shaped fracture created by a single fluid, the next study presented in Chapter 3 focused on the propagation of a "pre-filled" fracture due to the injection of an immiscible fluid. This allowed us to understand how the growth of a hydraulic fracture is modified by the successive injection of an oil phase and an aqueous phase in a gelatin block. We modeled the growth of the fracture and the interface between the two fluids by revisiting the theoretical framework established for a single fluid. Subsequently, we conducted a series of experiments in both the viscous-dominated regime and the toughness-dominated regime to experimentally validate the derived scales. We observed that in the toughness regime, the fracture dynamics for a displacement flow are the same as that of a single fluid, with the additional volume of the "pre-filled" fracture fluid. This is in stark contrast to the viscous regime, where the viscous dissipation in both the fluid phases contributes to the growth dynamics, and therefore, we use an effective viscosity that is averaged by accounting for the volume of the displaced and displacing fluid.

In Chapter 4, our focus shifted to studying the propagation dynamics when encountering distinct material layers. Our experimental findings demonstrated that when a fracture is initiated in the softer layer, it keeps propagating within that layer. Con-

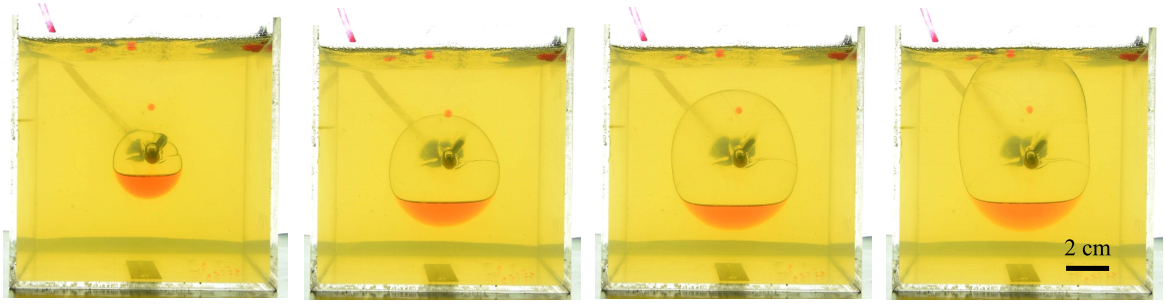

Figure 5.1: Injection in 15 KPa gelatin at 1 ml/min flow rate at times t = [12, 82, 152, 222] s. The red color is the silicone oil that was injected initially to make sure the fracture propagates in the right plane and the needle does not get clogged.

versely, if the fracture starts in the stiffer layer, it crosses the interface, experiences rapid fluid transfer into the softer layer, resumes propagation within the softer layer, while its growth is arrested within the stiffer layer. To capture these phenomena, we developed a model for fracture growth in the softer layer and collapse in the stiffer layer using an iterative approach. Our results highlight that stiffness contrast can significantly accelerate the growth of a fracture when it comes into contact with a material interface.

While the studies presented in this thesis further our understanding of hydraulic fractures in complex scenarios, there's still much to discover. Emerging technologies like carbon sequestration pose new challenges, requiring ongoing research in hydraulic fractures. Below I discuss some of the ideas that can be explored in the future.

Experimental investigation of buoyant fractures: An interesting area of research would be experimenting with a model system to create a single buoyant fracture [125]. This system presents an opportunity to study carbon sequestration in a low-permeability reservoir. A key focus could be to understand the transition of a radial hydraulic penny-shaped fracture from the toughness regime to a late-time toughness controlled buoyant fracture [126]. In an experiment conducted in the lab (see figure 5.1), we observed that the fracture starts out axisymmetric. Upon further injection of air it becomes buoyant and starts preferentially propagating upwards, finally breaking through the surface.

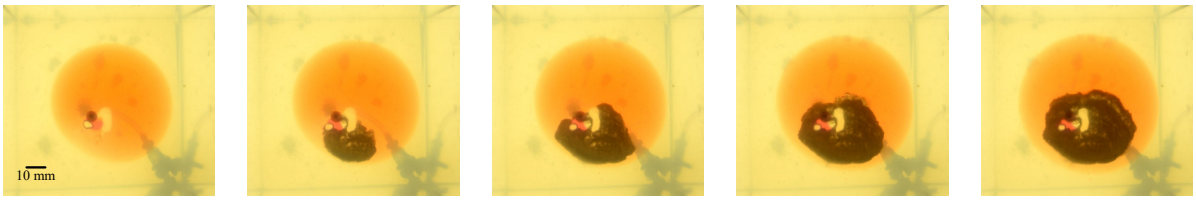

Figure 5.2: Injection of 2 M Na_2CO_3 solution at a flow rate of 1 ml/min in 30 Kpa gelatin with a "pre-fracture" of 10 ml 2 M $CaCl_2$ solution at t = [1, 75, 150, 225, 300] s. The red color is due to a water based dye added to help visualise the fracture.

Therefore, lab scale experiments would be a good approach to investigate caprock fracture due to the buoyant motion of the fracturing fluid. This study would represent a step towards understanding and eventually preventing the leakage of CO_2 back into the atmosphere, thereby contributing to the viability of geological CO_2 storage as an effective solution for climate change mitigation.

Reactive fracturing: Another interesting area of research would be to study reactive fracture fronts, where the fracturing fluid can either react with already existing fluid in the fracture, or with the surrounding solid medium. In an experiment conducted in a block of gelatin, we observed that when injecting Na_2CO_3 into a fracture already filled with $CaCl_2$, a spontaneous reaction occurs between the two fluids, creating $CaCO_3$, which is insoluble in water. As can be seen in figure 5.2, the two clear fluids react and form an opaque phase comprised of $CaCO_3$. This would be especially relevant to mineral sequestration where injected CO_2 undergoes chemical reactions that can deposit it in mineral form.

Hydraulic fracture in brittle elastic medium with rigid inclusions: A recent experimental study [36] has demonstrated that fractures generated in heterogeneous systems are rough due to the perturbation of the fracture front. This observation prompts further questions: Does the roughness affect the growth dynamics of the fracture? If so, can we utilize "effective" material parameters to accurately describe the long-term scaling

behavior? Another interesting area of research would be exploring how the interaction of fractures with rigid inclusions in striated rock formations modifies the fracture growth. This research could yield valuable insights into the complexities of fracture propagation in real-world geological settings, contributing to a more comprehensive understanding of fluid-driven fractures, their interactions with heterogeneous subsurface structures, and the development of predictive numerical models.

Appendix A

Fluid flow through hairy surfaces

In the course of my PhD I also had the opportunity to work on flow through cylindrical hair arrays. Hair-covered surfaces present in low Reynolds number (Re) flows are ubiquitous across biological systems in nature, ranging from the epithelial cilia in the human trachea to mechanosensory setae in crustaceans. These examples illustrate active cilia, which beat to drive a flow, or passive cilia, which control flow patterns in response external currents, respectively. Many filter-feeding species utilize microscopic passive hairs to filter and divert food particles to feed [127, 128, 129]. The adult barnacle *Semibalanus balanoides*, for example, controls the local flow through and around its short cirri by sweeping its long cirri at different speeds and for various durations. In engineered systems, transport through cylinders in into fluid channels has been investigated in recent years [130, 131, 132]. Bio-inspired devices utilizing hair array geometries analogous to those seen in marine crustaceans have the potential to mimic the particle capture and flow redirection properties that these biological examples exhibit. Being able to predict how the fluid behaves in the presence of these structures remains a challenge due to the nontrivial and nonlinear couplings at play.

We have published conference proceedings exploring the effect of surface coverage of hairs on filtration, presented below. Additionally, we have a manuscript in preparation where we investigate the effect of confinement on the flow through a square array of hairs in a rectangular channel. Sean Bohling, a fellow group member, has extended the study and is currently conducting additional research on flow through hair arrays in a cylindrical channel.

A.1 Effect of surface coverage on filtration performance of hair arrays: Numerical Study

A.1.1 Abstract

Biological filtration systems offer a sustainable alternative to existing engineered solutions. In this computational work, we seek to optimize the surface coverage by an array of hairs to capture particles in channels. A variety of aquatic organisms rely on arrays of hairs to interact with their fluidic environments. The hair functionality can vary from sensing to smelling, filtration to flow control depending on the species considered. Among those organisms are filter-feeders that rely on suspension-feeding, one of the most widespread feeding mechanisms and one of the oldest. Baleen whales are filter-feeders that catch their prey by using the baleen, a complex structure composed of plates and bristles in their mouth. The hairs are hollow cylindrical structures with a diameter of a few hundred micrometers that can extend over tens of centimeters. The baleen filters out the prey while letting the seawater through. The baleen is composed of flexible and elongated structures whose properties fit the feeding habits of the whale.

The porosity of the structure depends on the flow feature. Effectively, the flow can tune the filter properties, which sets biological filters apart from their engineered coun-

terpart. Previous mechanical studies have shown that an array of hairs can either act as a sieve, allowing all the fluid to flow through it, or as a rake, forcing the fluid to flow around it instead. As the speed increases, the behavior shifts from rake to sieving for a given hair spacing. From a filtration perspective, the rake regime is not favorable as particles do not enter the array. For a fixed fluid velocity, the flow transitions from rake to sieve as the spacing between the hairs in the array increases. Our recent work has also demonstrated that the confinement of the channel influences the sieve to rake transition.

The filtration mechanisms that filter-feeder organisms use to capture food particles exhibit complex fluid-structure interactions that have yet to be leveraged in engineered systems. To guide the development of hair-covered surfaces capable of trapping particles in channel flows, we investigate how different geometric factors affect the fluid transport and capture of particles by the array. In previous work, a small number of hairs, typically 25, were considered. Here, we vary the array geometry, the Reynolds number of the flow, and the surface coverage to study the transport through this confined porous structure. We compare arrays based on their optimal efficiency and the (sub-optimal) operating conditions which make the filter versatile.

A.1.2 Introduction

Particle filtration involves the separation of particles from the fluid flow, often using porous media. Fibrous filters commonly filter solid particles from aerosols and suspensions [133]. However, fibrous filters are also ubiquitous in Nature, where they exhibit improved performances. For example, biological filters provide a reliable source of food over the lifetime of the organism. Filter-feeding fish, including goldfish, suspension-feeder crabs, baleen whales, and sharks, manage to filter small prey from vast volumes of water without clogging their oral filters [134, 135]. Biologists have long assumed that filter-

feeding fish sieve particles of interest, effectively selecting particles that are too big to enter the fibrous structure [136]. But such biological filters also remove particles much smaller than the mesh size indicating a more complex filtration process. Rubenstein and Koehl [136] considered the biological trapping of particles through the mechanisms known to capture particles in industrial aerosol filters. They enumerated different mechanisms responsible for particle capture by filter feeders: direct interception, inertial impaction, gravitational deposition, and motile particle deposition. In direct interception, the particles follow the streamlines and are captured if the center of mass of the particles comes close enough to the fiber surface. The capture distance depends on the surface properties of both the particles and the fiber. In inertial impaction, the particles stop following the streamlines and adhere to the fiber surface if they come within the capture distance, at low enough speed that they do not bounce off. The gravitational interception occurs when the particle settles in the fluid and comes within the capture distance of the fiber. Finally, motile particles can migrate close enough to the fiber to get trapped. Direct interception is the most common capture mechanism for micrometer-scale non-motile particles in low-velocity flows.

Our study, therefore, focuses on the filtration of particles by a direct interception in a bio-inspired filter. For the sake of simplicity, the filter is a square array of long hair-like structures, similar to those that decorate the feeding appendages of crustaceans. The fluid carries density-matched particles along the streamlines and into the patch of hair-like obstacles. It is possible to model the system as two-dimensional, because of the aspect ratio of the hairs. Previous work has shown that the flow through a patch of hairs or filter structure exhibits different regimes under laminar conditions [137, 128, 132]. The flow regime transitions from rake to deflection and eventually sieve as the spacing between the hairs or flowrate increases. For small spacing and low flow rates, the array acts as a rake that deflects the flow. This regime corresponds to very little flow through

the fibrous structure. As the spacing and the flow rate increase, the streamlines start entering the array. In this intermediate regime, the streamlines bend, and the flow exits the array laterally. Finally, at large spacing and a large flowrate, the array acts as a sieve. Most streamlines travel from the upstream to the downstream faces of the array. In this study, we are interested in determining the influence of the flow regimes on the filtration performance of the array.

To study the filtration efficiency of different arrays of cylindrical hairs, we rely on finite element-based simulations. In the second and third sections, we describe the numerical methods and show that we recover the three flow regimes previously reported in the literature. In the fourth section, we define the filtration efficiency and compare the performance of different arrays under varying flow conditions. We conclude by discussing strategies to improve the efficiency of bio-inspired filters.

A.1.3 Numerical simulations

A.1.3.1 Governing equations

The two-dimensional model filter consists of circular fibers in a rectangular channel, as presented in fig. A.1. The fibers have a diameter d, and a center-to-center spacing noted δ. The axis of the fibers is perpendicular to the direction of the flow. The channel has a width W and a length L. The origin is set at the center of the channel. The density of the Newtonian fluid is ρ and the viscosity μ. We assume that the flow at the inlet is a fully developed Poiseuille flow for a rectangular channel whose velocity field is given by $\tilde{\mathbf{u}}(y)$. The average velocity of the flow is equal to

$$U_O = \frac{1}{W} \int \tilde{\boldsymbol{u}}(y) \, \mathrm{d}y \tag{A.1}$$

In the channel, the steady Navier-Stokes' and continuity equations govern the velocity

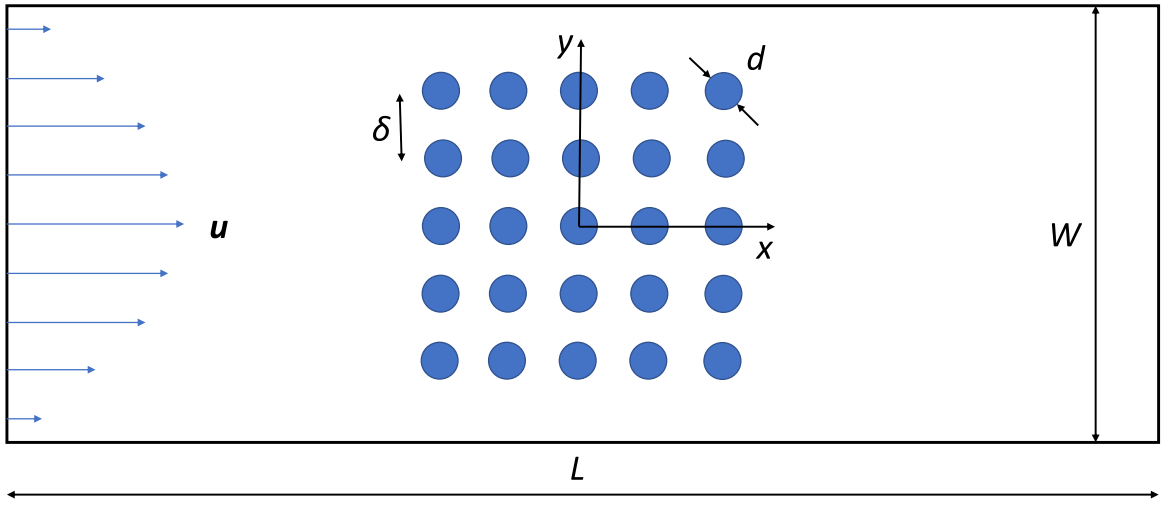

Figure A.1: Schematic of the channel.

field $\boldsymbol{u}$ and the pressure p of the flow

$$\mu\nabla^2\boldsymbol{u} - \nabla p = \rho\boldsymbol{u}\cdot\boldsymbol{\nabla}\boldsymbol{u} \tag{A.2}$$

$$\nabla.\boldsymbol{u} = 0 \tag{A.3}$$

Subject to the boundary conditions:

$$\boldsymbol{u} = 0, \text{ on the cylinder surfaces} \tag{A.4}$$

$$\boldsymbol{u}(y = \pm W/2) = 0, \text{ on the channel walls} \tag{A.5}$$

$$\boldsymbol{u}(x = -L/2) = \tilde{\boldsymbol{u}}, \text{ at the inlet.} \tag{A.6}$$

A.1.3.2 Simulations

We solve the system of equations described above by applying a finite element method using COMSOL Multiphysics. We model the flow in two dimensions. For all the simulations, $W = 60$ mm, $d = 1$mm, $L = 400$ mm, and δ varies from 2 to 10 mm. The flow is fully developed at the inlet $X = -L/2$. We define the Reynolds number Re of the flow with the average undisturbed velocity in the channel and the diameter of the cylinders:

$$Re = \frac{\rho\, d\, U_0}{\mu} \tag{A.7}$$

We explore a range of Re from 10e-03 to 40 for $\rho = 1000$ kg.m^{-3} and $\mu = 10$e-03 Pa.s. At the outlet, we set the pressure to the atmospheric pressure. The fluid flow along the channel walls and the surface of the cylinders are assumed to satisfy the no-slip condition. We use COMSOL Multiphysics' built-in meshing function to mesh the geometry at fine setting. The mesh around the cylindrical surfaces is automatically set to extra fine to account for the boundary layer surrounding them. We use free triangular elements and execute steady simulations as time-dependent or inertial effects are negligible in the system.

To study the performance of the hair array as a filter, we consider the direct interception mechanism. We assume that the particles to be filtered have a smaller diameter than the fiber:= $d/20$. A particle is intercepted if it travels on a streamline that comes close enough to the surface of a cylinder [138]. The progressive deposition of particles can modify the flow field [139] and even clog some of the narrowest regions of the array [138, 140, 141, 142]. Here we assume that only the particles whose surface comes in contact with a cylinder get trapped irreversibly. We can express this condition mathematically: if the distance between the center of mass of the particle and the surface of the cylindrical fiber is less than one particle radius, then the particle sticks irreversibly.

An annular region with an inner diameter d and outer diameter $d + (d/20)$ gives this sticking/capture region around each cylindrical surface. Therefore, we define the probability of capturing a particle as the flux of fluid into the capture regions divided by the total flow through the channel. Before studying the filtration process, we determine the flow field through the array and around each cylinder for different array sizes and array arrangements to compare their filtering efficiency.

A.1.4 The three flow regimes

Previous work by Hood et al. 2019 [132] has shown the existence of three flow regimes when fluid flows through an array of cylindrical hairs. Our simulations, presented in fig.A.2, evidence the same three flow regimes. We conduct a series of simulations with increasing Reynolds numbers from 10^{-3} to 40 as we keep the spacing between the hairs constant equal to $\delta = 4$ mm. At a low flow rate, the array acts as a sieve, and most of the fluid flows around fig.A.2(a). On the contrary, when the flow rates are high and the spacing between the hairs is larger, the fluid flows through the array, which behaves like a sieve fig.A.2(c). The transition regime between the rake and sieve is called the deflection flow regime fig.A.2(b): the fluid enters the array and exits the array laterally through the sides.

This phenomenon can be understood by looking at the change in boundary layer thickness around a single hair as the flow rate in the channel increases (see fig.A.3). When the flow rates are high, the boundary layer of a hair is thin. The width of the boundary layer is smaller than the spacing between two hairs. The boundary layers of two neighboring hairs do not overlap, and fluid can flow through the arrays. When the flow rate is low, the boundary layer thickness exceeds half the spacing between two neighboring hairs. The overlapping boundary layers dramatically reduce the fluid flow

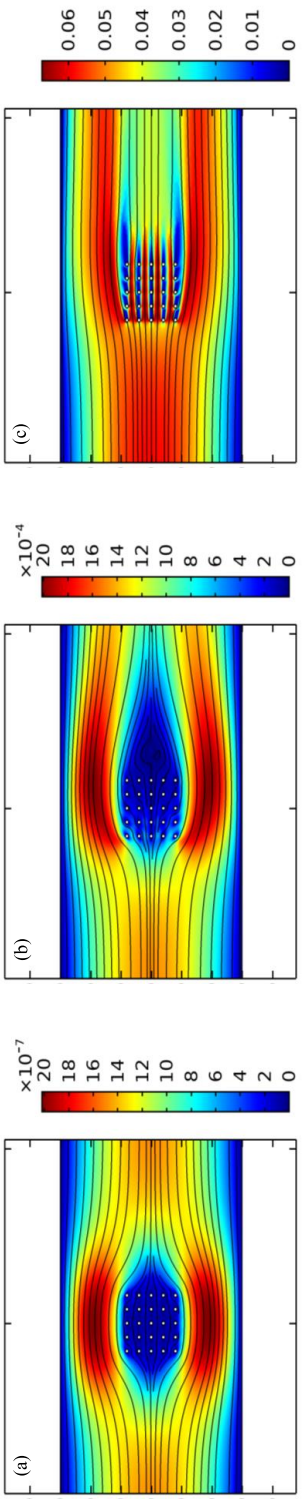

Figure A.2: Different flow regimes for $\delta = 4mm$ (a) $Re = 10^{-3}$, rake (b) $Re = 1$ deflection (c) $Re = 40$, sieve.

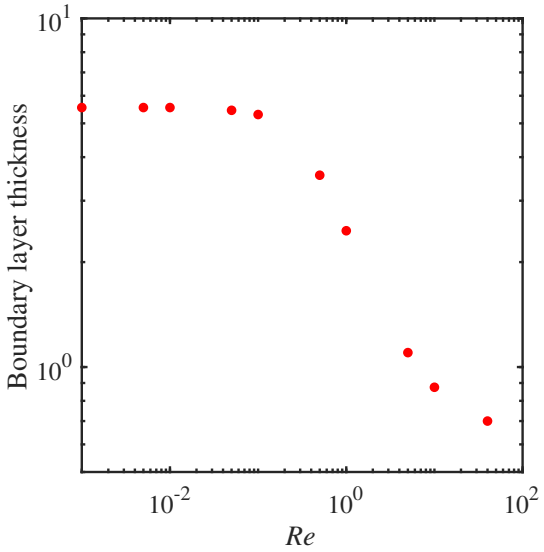

Figure A.3: Boundary layer thickness around a single cylindrical fibre.

through the array. As we assume the transport of particles along streamlines, we expect those flow regimes to influence the probability of particle capture.

A.1.5 Filtration

A.1.5.1 Efficiency definition

The first step in understanding filtration by an array of cylinders is to study the particle capture by a single cylindrical fiber. We will then compare the performance of the arrays with the performance of a single fiber, which is the unit structure of the system. We consider a single fiber located at the center of the channel. The cylinder disturbs the velocity profile in the channel. Because of the no-slip condition on the surface of the cylinder, we see a steep velocity gradient region in the boundary layer (see fig.A.3). The thickness of the boundary layer influences the filtration efficiency. To compare the performance of different filters, we use the capture efficiency, a parameter commonly used to describe engineered filters. For a cylindrical fiber, we define the filtration efficiency as

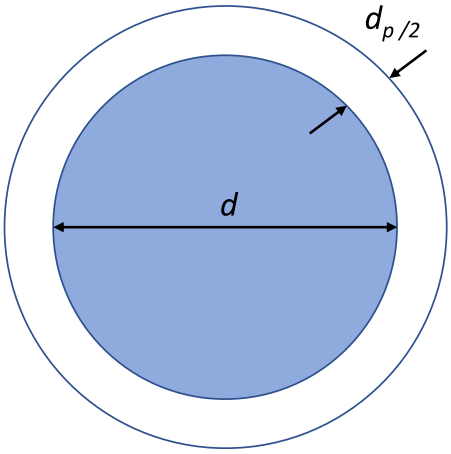

Figure A.4: Schematic of the capture region.

$$e = \frac{Q_{capture}}{U_c\, d} \tag{A.8}$$

where $Q_{capture}$ is the 2D fluid influx through the sticking/capture region around the cylinder, as shown in fig.A.4, and U_c is the average velocity through the cylinder in the undisturbed flow.

It is important to note that measuring the probability of capture leads to similar results. However the probability of capture cannot exceed 1, while the capture efficiency coefficient can, for example when the capture region is wide. We estimate the flow rate through the capture region and the undisturbed flow velocity using Comsol Multiphysics simulations and compute the filtration efficiency of a single hair. Figure A.5 presents the efficiency of a single hair as a function of the Re number of the flow. The efficiency is an increasing function of the Re. Since the boundary layer is thicker at lower Re numbers, there is not much flow influx through the capture region. As the Re number increases, the percentage of flow influx through the capture region increases. This also

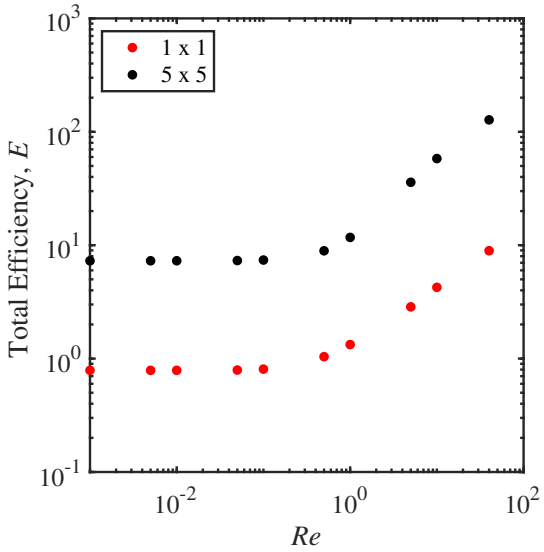

Figure A.5: Single hair Vs array: Comparision of total efficiency.

explains the different behavior observed at lower and higher Re. At low Re, the filtration efficiency is almost constant and independent of the Re. There is a strong dependence of the boundary layer thickness and efficiency on the Re out of the Stokes regime. In consequence, larger velocities are desirable to improve filtration efficiency.

A.1.5.2 Filtration by a 5×5 array

To define the efficiency of an array, we consider both the total efficiency of the array and the average efficiency of a single hair. For an array, we sum the filtration efficiency over every cylinder for the total efficiency E. To obtain the average efficiency, we divide the total efficiency by the number of cylinders in the array,

$$E = \sum_{i=1}^{N} \frac{Q_c apture}{U_{c,i} d} \tag{A.9}$$

where N is the number of cylindrical fibers in the array.

We first consider a square 5×5 array with an inter-fiber spacing of 4 mm. We compare

the total filtration efficiency of a single cylindrical fiber and the array. As we can see in fig.A.5, the total filtration efficiency of the array is higher than the single hair because the array has more cylinders that can capture more particles. The dependence of the filtration efficiency on the Re is the same for both systems, consistent with our analysis based on the boundary layer thickness. It is interesting to note that although the total filtration efficiency of the array is higher than the efficiency of the single hair, the ratio of the total efficiencies is smaller than 25, which is the number of hairs in the array. In average, a hair in the array is less efficient at capturing particles than a single hair. This means that, on average, the single fiber is much more efficient at filtering than a 5×5 array with a spacing of inter-fiber spacing of 4 mm. To understand the cause of this loss in filtration efficiency and minimize it, we look at different array structure.

A.1.5.3 Effect of varying the array dimensions

We systematically vary the array dimensions in both the x and y directions, i.e., we change the number of columns and rows of hairs. We consider different arrays of the form $i \times j$ where i is the number of rows and j is the number of columns. The inter-fiber spacing δ is kept constant equal to 4 mm. All the arrays are centered at the origin of the channel.

We first vary the number of rows while keeping the number of columns constant at 5. In figure A.6(a), we observe that all the arrays show the same qualitative behavior over the range of Re considered. The average filtration efficiency e is independent of the Re at lower values. At higher Re, the efficiency becomes an increasing function of the Re. If we now compare the average efficiency of a hair in the different arrays, we note that the efficiency is an increasing function of the number of rows for all Re. Interestingly, for an array with ten rows and five columns of hairs, the average efficiency is comparable to the efficiency of a single hair. We note that the average efficiency of the array even

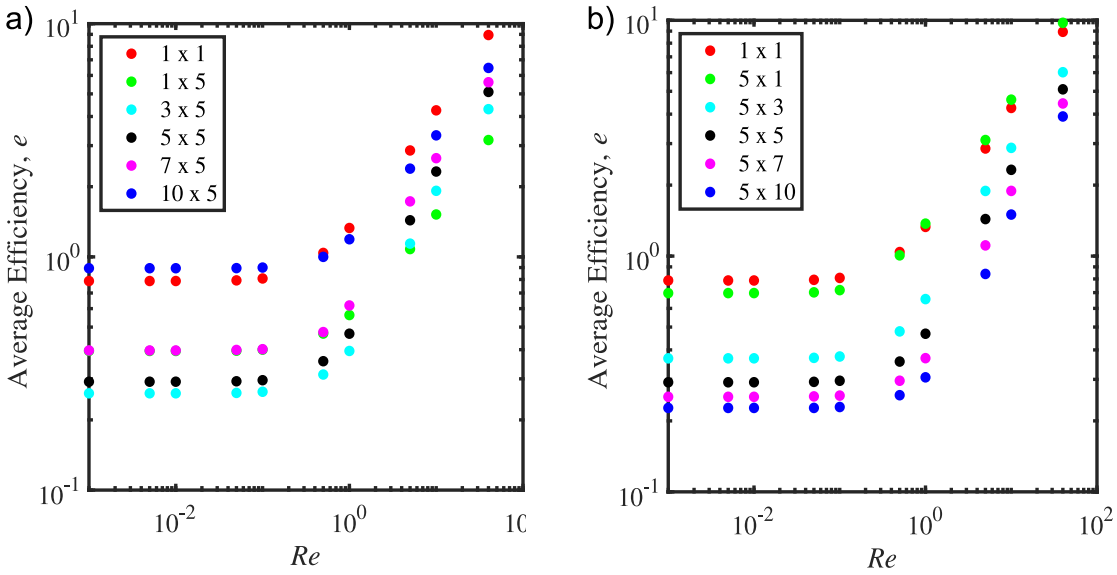

Figure A.6: Average efficiency as a function of Re, for different arrays. We vary the number of rows and columns in the array: (a) number of rows goes 1 to 10, for 5 columns and (b) number of rows is 5, while the number of columns goes from 1 to 10.

exceeds the efficiency of the single hair a low Re numbers. Still, it remains an order of magnitude below the efficiency of the large Re. We consider the flow through the system to rationalize the capture efficiency. As the number of rows increases, the open channels on either side of the array are progressively more restricted [143]. At low Re, this does not significantly modify the flow properties in the array but increases the average velocity in the side channel, which means that the cylinder lining the array will see its efficiency improve. Overall this improvement results in a modest increase in the efficiency with the number of rows at low Re. At large Re numbers, the restriction of the flow in the side channel increases the flow rate through the array, which further reduces the size of the boundary layer and significantly increases the average efficiency of the array. These results indicate that the confinement of the array is beneficial to the filtration process both at low and high Re.

Next, we vary the number of columns while keeping the number of rows constant and

equal to five. The average efficiency is a decreasing function of the number of columns, for all values of the Re considered. This is consistent with the decrease in speed of the flow as the number of rows increases. The efficiency loss as a function of the number of columns is greater for the first few columns, indicating that additional columns eventually add a slight but constant increase in total efficiency.

It is interesting to note that the efficiency for the 5×1 array is more than that for the single cylinder at higher Re. The confinement effect described above is responsible for increasing average efficiency for the column of hairs over a single hair. In conclusion, the average filtration efficiency depends on the aspect ratio of the array and its confinement. We can conclude that a wide array with fewer rows will lead to the most efficient filtration.

A.1.5.4 5×5 array with different spacing

Based on the previous result, we now compare the performance of square arrays. We vary the spacing between the cylinders for a symmetric 5×5 array to understand the effect of δ on the filtration efficiency. Figure A.7 reports the efficiency of different arrays as a function of the Re. At all values of Re, the performance of arrays with large spacing exceeds the performance of arrays with small spacing. For example, at lower Re, the efficiency of the $\delta = 12$ mm, $\delta = 10$ mm, and $\delta = 8$ mm is much higher than that of a single fiber. At higher Re, the single fiber crosses these two, and the efficiency for the single fiber is the highest at high Re. At high Re, we notice that after a point, increasing the spacing between the elements does not improve the efficiency.

To understand those results, we need to account for two effects. First, we know that confinement improves filtration efficiency. Increasing the spacing between posts reduces the space available for the flow around the array. As a result, more fluid flows through an array with larger spacing than through an array with smaller spacing. In addition, we should compare the spacing between posts with the size of the boundary

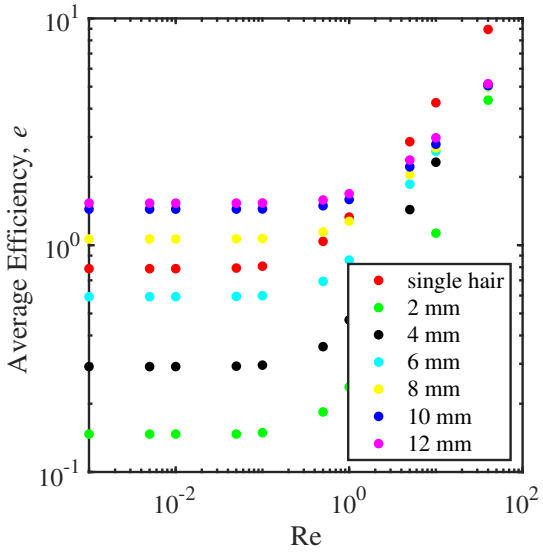

Figure A.7: Influence of spacing on the efficiency of a square array (5 x 5).

layer of the cylinders. As the spacing increases, the overlap between the boundary layers of two neighboring posts is reduced, which increases the filtration efficiency. Note that the overlap of the boundary layers determines the efficiency at low Re. Therefore, the improvement in filtration efficiency due to spacing increases is much more significant at low Re than the confinement effect alone. In conclusion, the increase in efficiency due to spacing between neighboring cylinders is valuable at all Re number. Compare to the confinement strategy through the addition of rows; the spacing approach yields greater results at low Re. The design of a filter with comparable performances at low and high Re will most benefit from increases in the cylinder spacing. In summary, the results of the numerical simulations indicate that, over the range of intermediate Re considered here, the efficiency increases with the width of the array and the spacing between the rows and columns.

A.1.6 Conclusion

This numerical study considers the efficiency of arrays of cylindrical fibers to filter buoyant particles that travel along the streamlines of a liquid flowing through a rectangular channel. We consider laminar flows and assume direct interception of the advected particles, as these conditions are prevalent in biological filters, like those of filter-feeders. Relying on two-dimensional simulations using Comsol Multiphysics, we compare the filter efficiency of different array geometries to improve the efficiency of square arrays of fibers. We find that the efficiency of all arrays increases with Re. The efficiency of an array is greater than the efficiency of a single hair. However, in most cases, the interactions between hairs reduce the individual efficiency of each hair, called the average efficiency. Comparing arrays of different aspect ratios, we show that the lateral confinement of the arrays improves efficiency. However, an increase in the number of columns decreases the average efficiency of the array. Similarly, we show that increasing the spacing between the cylinders improves the efficiency of capture. A filter needs to operate at higher Re (in the sieve regime), and the flow needs to be confined to improve the efficiency of the filter. Still, the rows and columns need to be placed as far from each other as possible, so the fluid influx through the capture region is higher. In the future, experimental work should test those findings and determine the upper bound of Re that maximizes the capture efficiency in the direct interception regime while minimizing inertial effects. In conclusion, this study identifies inter-cylinder spacing and lateral confinement as important design parameters to optimize filtration for the geometry described.

Bibliography

[1] FracFocus, "What is fracturing fluid made of?." Accessed: Nov 10, 2023.

[2] V. Onyebuchi, A. Kolios, D. Hanak, C. Biliyok, and V. Manovic, *A systematic review of key challenges of CO_2 transport via pipelines*, *Renew. Sustain. Energy Rev.* **81** (2018) 2563–2583.

[3] X. Yu, C. O. Catanescu, R. E. Bird, S. Satagopan, Z. J. Baum, L. M. L. Diaz, and Q. A. Zhou, *Trends in Research and Development for CO_2 Capture and Sequestration*, *ACS Omega* **8** (2023), no. 13 11643–11664.

[4] N. J. Huerta, K. J. Cantrell, S. K. White, and C. F. Brown, *Hydraulic fracturing to enhance injectivity and storage capacity of CO_2 storage reservoirs: Benefits and risks*, *Int. J. Greenh. Gas Control* **100** (2020) 103105.

[5] W. L. Ellsworth, *Injection-induced earthquakes*, *Science* **341** (2013) 1225942.

[6] L. J. Pyrak-Nolte and D. D. Nolte, *Approaching a universal scaling relationship between fracture stiffness and fluid flow*, *Nat. Commun.* **7** (2016), no. 1 10663.

[7] A. J. Kondash, N. E. Lauer, and A. Vengosh, *The intensification of the water footprint of hydraulic fracturing*, *Sci. Adv.* **4** (2018), no. 8 eaar5982.

[8] I. R. Kivi, R. Y. Makhnenko, C. M. Oldenburg, J. Rutqvist, and V. Vilarrasa, *Multi-Layered Systems for Permanent Geologic Storage of CO_2 at the Gigatonne Scale*, *Geophys. Res. Lett.* **49** (2022), no. 24 49.

[9] M. D. Zoback and S. M. Gorelick, *Earthquake triggering and large-scale geologic storage of carbon dioxide*, *Proc. Natl. Acad. Sci.* **109** (2012), no. 26 10164–10168.

[10] G. Wen and S. M. Benson, *CO_2 plume migration and dissolution in layered reservoirs*, *Int. J. Greenh. Gas Control* **87** (2019) 66–79.

[11] P. Fu, X. Ju, J. Huang, R. R. Settgast, F. Liu, and J. P. Morris, *CO_2 injection with fracturing in geomechanically protected caprock: Task 6 of LLNL's Research Activities to Support DOE's Carbon Storage Program (FWP-FEW0191)*, .

[12] P. Fu, X. Ju, J. Huang, R. R. Settgast, F. Liu, and J. P. Morris, *Thermo-poroelastic responses of a pressure-driven fracture in a carbon storage reservoir and the implications for injectivity and caprock integrity*, *Int. J. Numer. Anal. Methods Geomech.* **45** (2021), no. 6 719–737.

[13] J. A. Dammel, J. M. Bielicki, M. F. Pollak, and E. J. Wilson, *A Tale of Two Technologies: Hydraulic Fracturing and Geologic Carbon Sequestration*, *Environ. Sci. Technol.* **45** (2011), no. 12 5075–5076.

[14] E. Detournay, *Mechanics of hydraulic fractures*, *Annu. Rev. Fluid Mech.* **48** (2016) 311–339.

[15] I. N. Sneddon and N. F. Mott, *The distribution of stress in the neighbourhood of a crack in an elastic solid*, *Proc. R. Soc. Lond. A* **187** (1946) 229–260.

[16] S. Khristianovic and Y. Zheltov, *Formation of Vertical Fractures by Means of Highly Viscous Liquid*, *4th World Petrol. Congr. Proc.* **2** (1955) 576–586.

[17] G. Barenblatt, *On the formation of horizontal cracks in hydraulic fracture of an oil-bearing stratum*, *Prikl. Mat. Mech.* **20** (1956) 475–486.

[18] D. A. Spence and P. Sharp, *Self-similar solutions for elastohydrodynamic cavity flow*, *Proc. R. Soc. Lond. A* **400** (1985) 289–313.

[19] J. Desroches, E. Detournay, B. Lenoach, P. Papanastasiou, J. Pearson, M. Thiercelin, and A. Cheng, *The crack tip region in hydraulic fracturing*, *Proc. R. Soc. Lond. A* **447** (1994), no. 1929 39–48.

[20] D. I. Garagash and E. Detournay, *The tip region of a fluid-driven fracture in an elastic medium*, *J. Appl. Mech.* **67** (2000) 183–192.

[21] D. I. Garagash and E. Detournay, *Plane-strain propagation of a fluid-driven fracture: Small toughness solution*, *J. Appl. Mech.* **72** (2005) 916–928.

[22] A. A. Savitski and E. Detournay, *Propagation of a penny-shaped fluid-driven fracture in an impermeable rock: asymptotic solutions*, *Int. J. Solids Struct.* **39** (2002) 6311–6337.

[23] E. Detournay and D. Garagash, *The near-tip region of a fluid-driven fracture propagating in a permeable elastic solid*, *J. Fluid Mech.* **494** (2003) 1–32.

[24] A. Möri and L. Brice, *Arrest of a radial hydraulic fracture upon shut-in of the injection*, *Int. J. of Solids Struct.* **219-220** (2021) 151–165.

[25] A. Bunger and E. Detournay, *Asymptotic solution for a penny-shaped near-surface hydraulic fracture*, *Eng. Fract. Mech.* **72** (2005), no. 16 2468–2486.

[26] A. P. Bunger and E. Detournay, *Experimental validation of the tip asymptotics for a fluid-driven crack*, *J. Mech. Phys. Solids* **56** (2008) 3101–3115.

[27] A. Bunger, E. Gordeliy, and E. Detournay, *Comparison between laboratory experiments and coupled simulations of saucer-shaped hydraulic fractures in homogeneous brittle-elastic solids*, *J. Mech. Phys. Solids* **61** (2013), no. 7 1636–1654.

[28] C. Y. Lai, Z. Zheng, E. Dressaire, J. S. Wexler, and H. A. Stone, *Experimental study on penny-shaped fluid-driven cracks in an elastic matrix*, *Proc. R. Soc. Lond. A* **471** (2015) 20150255.

[29] C. Y. Lai, Z. Zheng, E. Dressaire, and H. A. Stone, *Fluid-driven cracks in an elastic matrix in the toughness-dominated limit*, *Phil. Trans. R. Soc. Lond. A* **374** (2016) 20150425.

[30] B. Lecampion, J. Desroches, R. Jeffrey, and A. Bunger, *Experiments versus theory for the initiation and propagation of radial hydraulic.pdf*, *J. Geophys. Res. Solid* **122** (2017), no. 2 1239–1263.

[31] N. O'Keeffe and P. Linden, *Hydrogel as a Medium for Fluid-Driven Fracture Study*, *Exp. Mech.* **57** (10, 2017) 1 – 11.

[32] N. J. O'Keeffe, H. E. Huppert, and P. F. Linden, *Experimental exploration of fluid-driven cracks in brittle hydrogels*, *J. Fluid Mech.* **844** (2018) 435–458.

[33] N. O'Keeffe, Z. Zheng, H. Huppert, and P. Linden, *Symmetric coalescence of two hydraulic fractures*, *Proc. National Acad. Sci. USA* **115** (2018), no. 41 10228 – 10232.

[34] C.-Y. Lai, B. Rallabandi, A. Perazzo, Z. Zheng, S. Smiddy, and H. Stone, *Foam-driven fracture*, *Proc. National Acad. Sci. USA* **115** (2018), no. 32 8082 – 8086.

[35] S.-M. Ham and T.-H. Kwon, *Photoelastic observation of toughness-dominant hydraulic fracture propagation across an orthogonal discontinuity in soft, viscoelastic layered formations*, *Int. J. Rock Mech. Min.* **134** (2020) 104438.

[36] W. Steinhardt and S. M. Rubinstein, *How material heterogeneity creates rough fractures*, *Phys. Rev. Lett.* **129** (Sep, 2022) 128001.

[37] A. Takada, *Experimental study on propagation of liquid-filled crack in gelatin: Shape and velocity in hydrostatic stress condition*, *J. Geophys. Res.* **95** (1990), no. B6 8471–8481.

[38] T. Menand and S. R. Tait, *The propagation of a buoyant liquid-filled fissure from a source under constant pressure: An experimental approach*, *J. Geophys. Res.* **107** (2002) ECV 16–1–ECV 16–14.

[39] J. Kavanagh, T. Menand, and K. Daniels, *Gelatine as a crustal analogue: Determining elastic properties for modelling magmatic intrusions*, *Tectonophysics* **582** (2013) 101–111.

[40] C.-Y. Lai, Z. Zheng, E. Dressaire, G. Z. Ramon, H. E. Huppert, and H. A. Stone, *Elastic Relaxation of Fluid-Driven Cracks and the Resulting Backflow*, *Phys. Rev. Lett.* (2016).

[41] S. S. Tanikella and E. Dressaire, *Axisymmetric displacement flows in fluid-driven fractures*, *J. Fluid Mech.* **953** (2022) A36.

[42] S. S. Tanikella, M. C. Sigallon, and E. Dressaire, *Dynamics of fluid-driven fractures in the viscous-dominated regime*, *Proc. R. Soc. A* **479** (2023) 20220460.

[43] D. E. Giuseppe, F. Funiciello, F. Corbi, G. Ranalli, and G. Mojoli, *Gelatins as rock analogs: A systematic study of their rheological and physical properties*, *Tectonophysics* **473** (2009) 391–403.

[44] U.S. Environmental Protection Agency, *Hydraulic fracturing for oil and gas: Impacts from the hydraulic fracturing water cycle on drinking water resources in the united states*, tech. rep., Office of Research and Development, Washington, DC, 2016.

[45] H. E. Huppert and J. A. Neufeld, *The fluid mechanics of carbon dioxide sequestration*, *Annu. Rev. Fluid Mech.* **46** (2013), no. 1 255–272.

[46] R. A. Caulk, E. Ghazanfari, and J. N. Perdrial, *Experimental investigation of fracture aperture and permeability change within enhanced geothermal systems*, *Geothermics* **62** (2016) 12–21.

[47] S. Jasechko and D. Perrone, *Hydraulic fracturing near domestic groundwater wells*, *Proc. Natl. Acad. Sci.* **114** (2017) 13138–13143.

[48] H. Yu, R. M. Harrington, H. Kao, Y. Liu, and B. Wang, *Fluid-injection-induced earthquakes characterized by hybrid-frequency waveforms manifest the transition from aseismic to seismic slip*, *Nat. Commun.* **12** (2021) 6862.

[49] P. Folger and M. Tienmann, *Human-induced earthquakes from deep-well injection: A brief overview*, *Congr. es. Serv.* **42** (2016).

[50] R. Schultz, G. Atkinson, D. W. Eaton, Y. J. Gu, and H. Kao, *Hydraulic fracturing volume is associated with induced earthquake productivity in the duvernay play*, *Science* **359** (2018) 304–308.

[51] U.S. Environmental Protection Agency, *Minimizing and managing potential impacts of injection-induced seismicity from class ii disposal wells: Practical approaches*, tech. rep., Underground Injection Control National Technical Workgroup, Washington, DC, 2016.

[52] A. A. Osiptsov, *Fluid mechanics of hydraulic fracturing: a review*, *J. Petrol. Sci. Eng.* **156** (2017) 513–535.

[53] A. A. Savitski and E. Detournay, *Similarity solution of a penny-shaped fluid-driven fracture in a zero-toughness linear elastic solid*, *C. R. Mec.* **329** (2001) 255–262.

[54] D. I. Garagash, E. Detournay, and J. I. Adachi, *Multiscale tip asymptotics in hydraulic fracture with leak-off*, *J. Fluid Mech.* **669** (2011) 260–297.

[55] J. R. Lister and R. C. Kerr, *Fluid-mechanical models of crack propagation and their application to magma transport in dykes*, *J. Geophys. Res.* **96** (1991) 10049–10077.

[56] D. P. Van Dam, de P., and R. Romijn, *Analysis of hydraulic fracture closure in laboratory experiments*, *SPE Production Facilities* **15** (2000), no. 03 151–158.

[57] D. I. Garagash, *Plane-strain propagation of a fluid-driven fracture during injection and shut-in: Asymptotics of large toughness*, *Eng. Fract. Mech.* **73-4** (2006) 456–481.

[58] A. Lakirouhani, E. Detournay, and A. P. Bunger, *A reassessment of in situ stress determination by hydraulic fracturing*, *Geophysical Journal International* **205-3** (2016) 1859–1873.

[59] A. P. Bunger, *A photometry method for measuring the opening of fluid-filled fractures*, *Meas. Sci. Technol.* **17** (2006) 3237.

[60] S. Tanikella, M. Sigallon, and E. Dressaire, *Data from: Dynamics of fluid-driven fractures in the viscous-dominated regime*, 2022.

[61] I. N. Sneddon and M. Lowengrub, *Crack Problems in the Classical Theory of Elasticity*. Wiley, 1969.

[62] G. K. Batchelor, *An introduction to fluid dynamics*. Cambridge University Press, 1967.

[63] J. R. Rice, *Mathematical analysis in the mechanics of fracture*. Academic Press, N. Y., 1968.

[64] A. Rubin, *Propagation of Magma-Filled Cracks*, *Annu. Rev. Earth Planet. Sci.* **23** (1995), no. 1 287 – 336.

[65] L. Cueto-Felgueroso and R. Juanes, *Forecasting long-term gas production from shale*, *Proc. National Acad. Sci. USA* **110** (2013), no. 49 19660–19661.

[66] H. Murphy, J. Tester, C. Grigsby, and R. Potter, *Energy extraction from fractured geothermal reservoirs in low-permeability crystalline rock*, *J. Geophys. Res.* **86** (1981), no. B8 7145–7158.

[67] J. Luo, Y. Zhu, Q. Guo, L. Tan, Y. Zhuang, M. Liu, C. Zhang, W. Xiang, and J. Rohn, *Experimental investigation of the hydraulic and heat-transfer properties of artificially fractured granite*, *Sci. Rep.* **7** (2017), no. 1 39882.

[68] B. Jia, J.-S. Tsau, and R. Barati, *A review of the current progress of CO2 injection EOR and carbon storage in shale oil reservoirs*, *Fuel* **236** (2019) 404–427.

[69] X. Bao and D. Eaton, *Fault activation by hydraulic fracturing in western Canada*, *Science* **354** (2016), no. 6318 1406–1409.

[70] D. Alessi, A. Zolfaghari, S. Kletke, J. Gehman, D. Allen, and G. Goss, *Comparative analysis of hydraulic fracturing wastewater practices in unconventional shale development: Water sourcing, treatment and disposal practices*, *Can. Water Resour. J.* **42** (2017), no. 2 1–17.

[71] A. Barbati, J. Desroches, A. Robisson, and G. McKinley, *Complex Fluids and Hydraulic Fracturing*, *Annu. Rev. Chem. Biomol. Eng.* **7** (2016) 415–453.

[72] S. Hormozi and I. Frigaard, *Dispersion of solids in fracturing flows of yield stress fluids*, *J. Fluid Mech.* **830** (2017) 93–137.

[73] T. Baumberger and O. Ronsin, *Environmental control of crack propagation in polymer hydrogels*, *Mech. Soft Mater.* **2** (2020), no. 1 14.

[74] J. Wang, D. Elsworth, and M. Denison, *Propagation, proppant transport and the evolution of transport properties of hydraulic fractures*, *J. Fluid Mech.* **855** (2018) 503–534.

[75] A. Bessmertnykh, E. Dontsov, and R. Ballarini, *Semi-Infinite Hydraulic Fracture Driven by a Sequence of Power-Law Fluids*, *J. Eng. Mech.* **147** (2021), no. 10 04021064.

[76] F.-E. Moukhtari and B. Lecampion, *A semi-infinite hydraulic fracture driven by a shear-thinning fluid*, *J. Fluid Mech.* **838** (2018) 573–605.

[77] B. Barboza, B. Chen, and C. Li, *A Review on Proppant Transport Modelling*, *J. Petrol. Sci. Eng.* **204** (2021) 108753.

[78] F. Parisio and K. Yoshioka, *Modeling Fluid Reinjection Into an Enhanced Geothermal System*, *Geophys. Res. Lett.* **47** (2020), no. 19.

[79] P. Saffman and G. Taylor, *The penetration of a fluid into a porous medium or Hele-Shaw cell containing a more viscous liquid*, *Proc. R. Soc. Lond. A* **245** (1958), no. 1242 312–329.

[80] L. Paterson, *Radial fingering in a Hele Shaw cell*, *J. Fluid Mech.* **113** (1981), no. -1 513–529.

[81] C.-W. Park and G. Homsy, *Two-phase displacement in Hele Shaw cells: theory*, *J. Fluid Mech.* **139** (1984) 291–308.

[82] J.-D. Chen, *Growth of radial viscous fingers in a Hele-Shaw cell*, *J. Fluid Mech.* **201** (1989) 223–242.

[83] G. Homsy, *Viscous Fingering in Porous Media*, *Annu. Rev. Fluid Mech.* **19** (1987), no. 1 271–311.

[84] R. Lenormand, E. Touboul, and C. Zarcone, *Numerical models and experiments on immiscible displacements in porous media*, *J. Fluid Mech.* **189** (1988) 165–187.

[85] S. Tanveer, *Evolution of Hele-Shaw interface for small surface tension*, *J. Geophys. Res.* **343** (1993), no. 1668 155–204.

[86] B. Primkulov, A. Pahlavan, X. Fu, B. Zhao, C. MacMinn, and R. Juanes, *Signatures of fluid–fluid displacement in porous media: wettability, patterns and pressures*, *J. Fluid Mech.* **875** (2019) 133 – 13.

[87] B. Primkulov, A. Pahlavan, X. Fu, B. Zhao, C. MacMinn, and R. Juanes, *Wettability and Lenormand's diagram*, *J. Fluid Mech.* **923** (2021) A34.

[88] P. Tabeling, G. Zocchi, and A. Libchaber, *An experimental study of the Saffman-Taylor instability*, *J. Fluid Mech.* **177** (1987) 67–82.

[89] R. Lenormand, C. Zarcone, and A. Sarr, *Mechanisms of the displacement of one fluid by another in a network of capillary ducts*, *J. Fluid Mech.* **135** (1983) 337–353.

[90] B. Zhao, C. MacMinn, and R. Juanes, *Wettability control on multiphase flow in patterned microfluidics*, *Proc. National Acad. Sci. USA* **113** (2016), no. 37 10251–10256.

[91] J. Stokes, D. Weitz, J. Gollub, A. Dougherty, M. Robbins, P. Chaikin, and H. Lindsay, *Interfacial Stability of Immiscible Displacement in a Porous Medium*, *Phys. Rev. Lett.* **57** (1986), no. 14 1718–1721.

[92] C. Cottin, H. Bodiguel, and A. Colin, *Drainage in two-dimensional porous media: From capillary fingering to viscous flow*, *Phys. Rev. E* **82** (2010), no. 4 046315.

[93] R. Glass, H. Rajaram, and R. Detwiler, *Immiscible displacements in rough-walled fractures: Competition between roughening by random aperture variations and smoothing by in-plane curvature*, *Phys. Rev. E* **68** (2003), no. 6 061110.

[94] Y. Chen, S. Fang, D. Wu, and R. Hu, *Visualizing and quantifying the crossover from capillary fingering to viscous fingering in a rough fracture*, *Water Resour. Res.* **53** (2017), no. 9 7756–7772.

[95] Z. Yang, Y. Méheust, I. Neuweiler, R. Hu, A. Niemi, and Y. Chen, *Modeling Immiscible Two-Phase Flow in Rough Fractures From Capillary to Viscous Fingering*, *Water Resour. Res.* **55** (2019), no. 3 2033–2056.

[96] T. Al-Housseiny, P. Tsai, and H. Stone, *Control of interfacial instabilities using flow geometry*, *Nat. Phys.* **8** (2012), no. 10 747–750.

[97] T. Al-Housseiny and H. Stone, *Controlling viscous fingering in tapered Hele-Shaw cells*, *Phys. Fluids* **25** (2013), no. 9 092102 – 12.

[98] N. Lu, C. Browne, D. Amchin, J. Nunes, and S. Datta, *Controlling capillary fingering using pore size gradients in disordered media*, *Phys. Rev. Fluids* **4** (2019), no. 8 084303.

[99] D. Pihler-Puzović, P. Illien, M. Heil, and A. Juel, *Suppression of Complex Fingerlike Patterns at the Interface between Air and a Viscous Fluid by Elastic Membranes*, *Phys. Rev. Lett.* **108** (2012), no. 7 074502.

[100] D. Pihler-Puzović, R. Périllat, M. Russell, A. Juel, and M. Heil, *Modelling the suppression of viscous fingering in elastic-walled Hele-Shaw cells*, *J. Fluid Mech.* **731** (2013) 162–183.

[101] D. Pihler-Puzovic, A. Juel, G. Peng, J. Lister, and M. Heil, *Displacement flows under elastic membranes. Part 1. Experiments and direct numerical simulations*, *J. Fluid Mech.* **784** (11, 2015) 487 – 511.

[102] G. Peng, D. Pihler-Puzovic, A. Juel, M. Heil, and J. Lister, *Displacement flows under elastic membranes. Part 2. Analysis of interfacial effects*, *J. Fluid Mech.* **784** (11, 2015) 512 – 547.

[103] E. Detournay, *Propagation regimes of fluid-driven fractures in impermeable rocks*, *Int. J. Geomech.* **4** (2004), no. 1 35–45.

[104] E. Detournay and A. Peirce, *On the moving boundary conditions for a hydraulic fracture*, *Int. J. Eng. Sci.* **84** (2014) 147–155.

[105] M. Kanninen and C. Popelar, *Advanced Fracture Mechanics*. No. 15 in Oxford Engineering Science Series. Oxford University Press, 1985.

[106] *Hydraulic Fracturing for Oil and Gas: Impacts from the Hydraulic Fracturing Water Cycle on Drinking Water Resources in the United States (Final Report)*, Technical Report EPA/600/R-16/236F, U.S. Environmental Protection Agency, Washington, DC, 2016.

[107] S. Pandey, A. Chaudhuri, and S. Kelkar, *A coupled thermo-hydro-mechanical modeling of fracture aperture alteration and reservoir deformation during heat extraction from a geothermal reservoir*, *Geothermics* **65** (2017) 17–31.

[108] F. Parisio, V. Vilarrasa, W. Wang, O. Kolditz, and T. Nagel, *The risks of long-term re-injection in supercritical geothermal systems*, *Nature Communications* **10** (2019), no. 1 4391.

[109] D. L. Young, H. Johnston, and C. Augustine, *Electrical energy storage using compressed gas in depleted hydraulically fractured wells*, *iScience* **24** (2021), no. 12 103459.

[110] Z. Tao and A. Clarens, *Estimating the Carbon Sequestration Capacity of Shale Formations Using Methane Production Rates*, *Environmental Science & Technology* **47** (2013), no. 19 11318–11325.

[111] S. Sharma, V. Agrawal, S. McGrath, J. A. Hakala, C. Lopano, and A. Goodman, *Geochemical controls on CO_2 interactions with deep subsurface shales: implications for geologic carbon sequestration*, *Environ. Sci.: Processes Impacts* **23** (2021), no. 9 1278–1300.

[112] N. Gupta and A. Verma, *Supercritical Carbon Dioxide Utilization for Hydraulic Fracturing of Shale Reservoir, and Geo-Storage: A Review*, *Energy & Fuels* **37** (2023), no. 19 14604–14621.

[113] National Academies of Sciences, Engineering, and Medicine, *Characterization, Modeling, Monitoring, and Remediation of Fractured Rock*. The National Academies Press, Washington, DC, 2020.

[114] H. S. Viswanathan, J. Ajo-Franklin, J. T. Birkholzer, J. W. Carey, Y. Guglielmi, J. D. Hyman, S. Karra, L. J. Pyrak-Nolte, H. Rajaram, G. Srinivasan, and D. M. Tartakovsky, *From Fluid Flow to Coupled Processes in Fractured Rock: Recent Advances and New Frontiers*, *Rev. Geophys.* **60** (2022), no. 1.

[115] C. T. Montgomery and M. B. Smith, *Hydraulic Fracturing: History of an Enduring Technology*, *J. Pet. Technol.* **12** (2010), no. 62 26–40.

[116] M. Zoback and D. Smit, *Meeting the challenges of large-scale carbon storage and hydrogen production*, *Proceedings of the National Academy of Sciences* **120** (2023), no. 11 e2202397120.

[117] L. Teufel and J. Clark, *Hydraulic fracture propagation in layered rock: Experimental studies of fracture containment*, *SPE Journal* **24** (1984) 19–32.

[118] M. B. Smith, A. B. Bale, L. K. Britt, H. H. Klein, E. Siebrits, and X. Dang, *Layered modulus effects on fracture propagation, proppant placement, and fracture modeling*, *Proc. - SPE Annu. Tech. Conf. Exhib.* **SPE 71654** (2001) 1–14.

[119] J. Huang, P. Fu, R. R. Settgast, J. P. Morris, and F. J. Ryerson, *Evaluating a simple fracturing criterion for a hydraulic fracture crossing stress and stiffness contrasts*, *Rock Mech. Rock Eng.* **52** (2019), no. 6 1657–1670.

[120] N. R. Warpinski, J. A. Clark, R. A. Schmidt, and C. W. Huddle, *Laboratory investigation on the effect of in-situ stresses on hydraulic fracture containment*, *SPE J.* **22** (1982), no. 03 333–340.

[121] D. Liu, B. Lecampion, and D. I. Garagash, *Propagation of a fluid-driven fracture with fracture length dependent apparent toughness*, *Eng. Fract. Mech.* **220** (2019) 106616.

[122] H. Zia, B. Lecampion, and W. Zhang, *Impact of the anisotropy of fracture toughness on the propagation of planar 3d hydraulic fracture*, *Int. J. Fracture* **211** (2018) 103–123.

[123] M. A. Biot, W. L. Medlin, and L. Massé, *Fracture Penetration Through an Interface*, *SPE J.* (1983).

[124] D. Garagash and E. Detournay, *The tip region of a fluid-driven fracture in an elastic medium*, *J. Appl. Mech.* **67** (06, 1999) 183–192.

[125] M. Heimpel and P. Olson, *Chapter 10 buoyancy-driven fracture and magma transport through the lithosphere: Models and experiments*, in *Magmatic Systems* (M. P. Ryan, ed.), vol. 57 of *International Geophysics*, pp. 223–240. Academic Press, 1994.

[126] A. Möri and B. Lecampion, *Three-dimensional buoyant hydraulic fractures: Constant release from a point source*, *J. Fluid Mech.* **950** (2022) A12.

[127] H. U. Riisgård and P. S. Larsen, *Particle capture mechanisms in suspension-feeding invertebrates*, *Mar. Ecol. Prog. Ser.* **418** (2010) 255–293.

[128] M. Koehl, J. Koseff, J. Crimaldi, M. McCay, T. Cooper, M. Wiley, and P. Moore, *Lobster Sniffing: Antennule Design and Hydrodynamic Filtering of Information in an Odor Plume*, *Science* **294** (2001), no. 5548 1948–1951.

[129] L. Watling and M. Thiel, *Functional Morphology and Diversity*. Oxford University Press, 2013.

[130] C.-Y. Chen, L.-Y. Cheng, C.-C. Hsu, and K. Mani, *Microscale flow propulsion through bioinspired and magnetically actuated artificial cilia*, *Biomicrofluidics* **9** (2015), no. 3 034105.

[131] A. C. Balazs, A. Bhattacharya, A. Tripathi, and H. Shum, *Designing bioinspired artificial cilia to regulate particle–surface interactions*, *J. Phys. Chem. Lett.* **5** (2014), no. 10 1691–1700.

[132] M. Hood, K. andJammalamadaka and A. Hosoi, *Marine Crustaceans with Hairy Appendages: Role of Hydrodynamic Boundary Layers in Sensing and Feeding*, *Phys. Rev. Fluids* **4** (2019), no. 11 114102.

[133] V. Rastegar, G. Ahmadi, and S. Babu, *Effect of Flow Velocity on Fiber Efficiency and Particle Residence Time during Filtration of Aqueous Dispersions—An Experimental and Simulation Study*, *Particul. Sci. Technol.* **37** (2017), no. 2 161–170.

[134] S. Conova, *Role of Particle Wettability in Capture by a Suspension-Feeding Crab (Emerita Talpoida)*, *Mar. Biol.* **133** (1999), no. 3 419–428.

[135] S. Sanderson, E. Roberts, J. Lineburg, and H. Brooks, *Fish Mouths as Engineering Structures for Vortical Cross-Step Filtration*, *Nat. Comm.* **7** (2016), no. 1 11092.

[136] D. Rubenstein and M. Koehl, *The Mechanisms of Filter Feeding: Some Theoretical Considerations*, *Am. Nat.* **111** (1977), no. 981 981–994.

[137] A. Cheer and M. Koehl, *Paddles and Rakes: Fluid Flow through Bristled Appendages of Small Organisms*, *J. Theor. Biol.* **129** (1987), no. 1 17–39.

[138] H. Wyss, D. Blair, J. Morris, H. Stone, and D. Weitz, *Mechanism for Clogging of Microchannels*, *Phys. Rev. E.* **74** (2006), no. 6 061402.

[139] F. Gregori, J. Kapran, and E. Dressaire, *Filtration of Floating Particles by Collectors: Influence of the System Geometry on the Efficiency*, *Fluids. Eng.* **7** (2017) V007T09A049–V007T09A049.

[140] V. Ramachandran and H. Fogler, *Plugging by Hydrodynamic Bridging during Flow of Stable Colloidal Particles within Cylindrical Pores*, *J. Fluid. Mech.* **385** (1999) 129–156.

[141] E. Dressaire and A. Sauret, *Clogging of Microfluidic Systems*, *Soft Matter* **13** (2016) 37–48.

[142] C. Cejas, F. Monti, M. Truchet, J. Burnouf, and P. Tabeling, *Particle Deposition Kinetics of Colloidal Suspensions in Microchannels at High Ionic Strength*, *Langmuir* **33** (2017) 6471–6480.

[143] E. Strong, M. Pezzulla, F. Gallaire, P. Reis, and L. Siconolfi, *Hydrodynamic Loading of Perforated Disks in Creeping Flows*, *Phys. Rev. Fluids* **4** (2019) 084101.